TECHNISCHE UNIVERSITÄT MÜNCHEN

Fakultät für Maschinenwesen

Lehrstuhl für Nukleartechnik

Investigation of very high burnup UO_2 fuels in Light Water Reactors

Fabiola Cappia

Vollständiger Abdruck der von der promotionsführenden Einrichtung Fakultät für Maschinenwesen der Technischen Universität München zur Erlangung des akademischen Grades eines

Doktor-Ingenieurs (Dr.-Ing.)

genehmigten Dissertation.

Vorsitzender: Prof. Dr.-Ing. Klaus Drechsler

Prüfender der Dissertation:

1. Prof. Rafael Macián-Juan, Ph.D.
2. Prof. Lelio Luzzi, Ph.D. (Politecnico di Milano, Italien)

Die Dissertation wurde am 13.01.2017 bei der Technischen Universität München eingereicht und durch die Fakultät für Maschinenwesen am 27.03.2017 angenommen.

E se avessi il dono della profezia
e conoscessi tutti i misteri e tutta la scienza,
e possedessi la pienezza della fede
così da trasportare le montagne,
ma non avessi l'amore,
non sarei nulla

I Corinzi 1 13:2

A mamma e nonna,
muse di amore incondizionato

A papá,
per avermi reso forte

The most beautiful experience we can have is the mysterious.
It is the fundamental emotion that stands
at the cradle of true art and true science.

A. Einstein

Contents

List of Figures

List of Tables

Abstract

Historically, the average discharge burnup of Light Water Reactor (LWR) fuel has increased almost continuously. On one side, increase in the average discharge burnup is attractive because it contributes to decrease part of the fuel cycle costs. On the other side, it raises the practical problem of predicting the performance, longevity and properties of reactor fuel elements upon accumulation of irradiation damage and fission products both during in-reactor operation and after discharge. Performance of the fuel and structural components of the core is one of the critical areas on which the economic viability and public acceptance of nuclear energy production hinges.

Along the pellet radius, the fuel matrix is subjected to extremely heterogeneous alteration and damage, as a result of temperature and burnup gradients. In particular, in the peripheral region of LWR UO_2 fuel pellets, when the local burnup exceeds 50-70 GWd/tHM, a microstructural transformation starts to take place, as a consequence of enhanced accumulation of radiation damage, fission products and limited thermal recovery. The newly formed structure is commonly named High Burnup Structure (HBS). The HBS is characterised by three main features: (a) formation of submicrometric grains from the original grains, (b) depletion of fission gas from the fuel matrix, (c) steep increase in the porosity, which retains most of the gas depleted from the fuel matrix.

The last two aspects rose significant attention because of the important impact of the fission gas behaviour on integral fuel performance. The porosity increase controls the gas-driven swelling, worsening the cladding loading once the fuel-cladding gap is closed. Another concern is that the large retention of fission gas within the HBS could lead to significant release at high burnups through the degradation of thermal conductivity or contribute to fuel pulverisation during accidental conditions.

Need of more experimental investigations about the fuel mechanical properties and their relationship with the local microstructure at high burnup has been recognised, being one of the factors influencing Pellet-Cladding Mechanical Interaction (PCMI). The knowledge of the fuel mechanical properties has also fundamental importance to assess the mechanical integrity of the spent fuel during the back end of the fuel cycle.

In this context, the scope of this work was twofold. The first task was the experimental study of the fuel microhardness and Young's modulus in high burnup UO_2 fuels and their relationship with the local porosity, which has a major impact on their variation. Moreover, assessment of the accumulation of the decay damage during storage and its influence on the fuel microhardness has been carried out, in the framework of safety studies on the back end of the fuel cycle at high burnup. The second task consisted in the

evaluation of the porosity and pore size distribution evolution in high burnup fuel, with particular focus on the HBS porosity.

The experimental relationship between the high burnup fuel Young's modulus and local porosity obtained through combination of acoustic microscopy and microindentation measurements has been compared to the material property correlations commonly used in fuel performance codes, which are based on data from characterization of unirradiated UO_2. The investigation has revealed that the relationship is similar for non-irradiated and irradiated material, but in the latter case an additional factor that takes into account the Young's modulus decrease due to burnup accumulation has to be included in the correlation to match the experimental values.

First analysis of the fuel microhardness as a function of the accumulated decay damage has shown that fuel microhardness does not significantly increase when the dose due to the additional decay damage accumulated during storage reaches $\approx$0.1 dpa, in agreement with what observed in unirradiated ^{238}Pu-doped UO_2. However, further investigation is needed to determine the kinetics of hardening and to confirm if the observed behaviour holds in other cases, e.g., at lower and at higher accumulated dpa.

Concerning the second part of the research, a new methodology, based on the adaptive kernel estimator, has been introduced for the experimental determination of the three-dimensional pore size distribution and pore density in the fuel, in order to introduce a best-practice approach in this type of experimental analyses. The method has been applied not only to the pellet rim, where the HBS is present, but also to the so called "dark zone" and other pellet radial positions characterised by high fission gas bubble density, whose porosity is generally not specifically quantified. The study revealed that pore density and pore sizes comparable to what found in the HBS are present. Analysis of the fuel microstructure showed systematic presence of round subgrains around the pores and on free surfaces, suggesting that a restructuring process might be in fieri also at intermediate radial positions, albeit at a lower extent compared to the pellet periphery.

In the pellet rim, the analysis of the pore density and mean pore size as a function of the local burnup has shown that upon reaching $\approx$100 GWd/tHM pore coarsening is evident. A first attempt to explain such behaviour based on the hypothesis that the drop of pore density is due to coalescence of growing pores is given. The model was based on the work by White for the fundamental mechanism, but with a modification that took into account the experimental observations in this work. White modelled the pore system according to a system of fully overlapping disks. Measurements of the autocorrelation function of the pore phase performed through image analysis showed a behaviour more similar to a system of hard spheres. Therefore, the coarsening mechanism was modified, taking into account the nearest-neighbour statistics for hard spheres. This model was coupled with another existing model that describes the xenon depletion and pore growth in the HBS and compared to the experimental data. The modification introduced in the coarsening mechanism improved the agreement with the trend of the experimental data, providing a first insight on the main underlying physical phenomena likely to be responsible for bubble swelling in the HBS.

Zusammenfassung

Historisch gesehen, hat sich die durchschnittliche Abbrand von Leichtwasserreaktoren (LWR) Brennstoffen ständig erhöht. Auf der einen Seite, Erhöhung des durchschnittlichen Abbrands ist attraktiv, weil es einen Teil der Kernbrennstoffkreislauf zu senken beiträgt. Auf der anderen Seite stellt sich die praktische Probleme der Performance, Langlebigkeit und Eigenschaften der Brennstoffelementen bei Ansammlung von Spaltschäden und Spaltprodukte während der Betriebszeit und nach der Entlassung von Reaktor vorherzusagen. Performance der Brennstoff und Strukturkomponenten des Kerns ist einer der kritischen Bereiche, auf denen die Wirtschaftlichkeit und die öffentliche Akzeptanz der Kernenergieproduktion abhängt.

Entlang der Radius wird die Brennstoffmatrix zu extrem heterogenen Veränderung und Beschädigung ausgesetzt, infolge Steigungen der Temperatur und des Abbrands. Insbesondere im Randbereich von LWR UO_2 Brennstoff-Pellets, wenn die lokale Abbrand 50-70 GWd/tHM überschreitet, vollzieht sich eine Gefügeumwandlung, als Folge der verstärkten Anhäufung von Strahlenschäden, Spaltprodukte und begrenzten thermischen Verwertung. Die neu gebildete Struktur wird allgemein Hoch Abbrand Struktur (HBS) benannt. Die HBS durch drei Hauptmerkmale gekennzeichnet ist: (a) Bildung von submikrometrischen Körner von den ursprünglichen Körner, (b) Abreicherung von Spaltgas aus dem Brennstoffmatrix, (c) steilen Anstieg der Porosität, die das meiste Spaltgas aus die Kraftstoffmatrix aufgebrauchte behält.

Die letzten beiden Aspekte stieg große Aufmerksamkeit wegen der erheblichen Folgen der Spaltgasverhalten auf integralen Brennstoffleistung. Die Porosität Erhöhung steuert die gasbetriebenen Schwellung und verschlechtert die Belastung der Verkleidung, sobald die Lücke geschlossen ist. Eine weitere Sorge ist, dass die große Retention von Spaltgas in der HBS zu signifikantem Maße zur Freisetzung durch die Verschlechterung der Wärmeleitfähigkeit bei hohen Abbrand führen könnte oder dazu beitragen, Pulverisierung des Brennstoffs bei zufälligen Bedingungen.

Notwendigkeit von mehr experimentelle Untersuchungen über mechanischen Eigenschaften der Brennstoffe und ihre Beziehung mit der lokalen Mikrostruktur bei hohem Abbrand wurde auch anerkannt, da sie einer der Faktoren sind, die Pellet-Verschalungen mechanische Wechselwirkung beeinflussen. Die Kenntnis der mechanischen Eigenschaften des Brennstoffs hat auch grundlegende Bedeutung der mechanischen Integrität des Brennstoffs während das hintere Ende an dem Kraftstoffkreislauf zu beurteilen.

In diesem Zusammenhang ist der Anwendungsbereich dieser Arbeit zweifach. Die erste Aufgabe war die experimentelle Untersuchung des Brennstoffmikrohärte und Elastiz-

itätsmodul UO_2 Brennstoffe hohen Abbrands und deren Beziehung zur lokalen Porosität, die den größten Einfluss auf ihre Variation hat. Außerdem Beurteilung der Akkumulation des Zerfalls Beschädigung während der Lagerung und ihren Einfluss auf die Kraftstoffmikrohärte wurde im Rahmen der Sicherheitsstudien am hinteren Ende des Brennstoffkreislaufs bei hohem Abbrand durchgeführt. Die zweite Aufgabe bestand in der Bewertung der Porosität und Porengrößenverteilung Entwicklung in Brennstoffen hohen Abbrands, mit besonderem Schwerpunkt auf der HBS Porosität.

Die experimentelle Beziehung zwischen dem Brennstoffs hohen Abbrands Elastizitätsmodul und lokale Porosität, die durch Kombination von akustischen Mikroskopie und Mikroindentation Messungen erhalten wurde, wurde mit die Werte des Elastizitätsmoduls, die auf nicht-bestrahlten UO_2 Daten basieren, häufig benutzt in Computerprogrammen zur Berechnung der Brennstoffleistungsfähigkeit verglichen. Die Untersuchung hat ergeben, dass die Beziehung für die nicht bestrahlte und bestrahlte Material ähnlich ist, aber in dem letzteren Fall ist ein zusätzlicher Faktor, der den Elastizitätsmodul Abnahme infolge Abbrand Akkumulations berücksichtigt hat, in der Korrelation einbezogen werden, um die experimentellen Daten zu reproduzieren.

Erste Analyse des Brennstoffs Mikrohärte als Funktion des Zerfalls Schaden angesammelt hat, dass die Kraftstoff-Mikrohärte entspricht nicht signifikant erhöhen, wenn die Dosis auf Grund der zusätzlichen Verfall Schäden während der Lagerung angesammelt $\approx$0.1 dpa erreicht, in übereinstimmung mit dem, was auf den ^{238}Pu-dotierten Proben beobachtet wurde. Allerdings sind weitere Untersuchungen nötig, um die Kinetik der Härtung zu bestimmen und um zu bestätigen, ob das beobachtete Verhalten in anderen Fällen und bei höheren kumulierten dpa gilt.

In Bezug auf den zweiten Teil der Forschung, eine neue Methodik, auf dem adaptiven Kernel-Schätzer basiert, wurde für die experimentelle Bestimmung der dreidimensionalen Porengrößenverteilung und Porendichte im Kraftstoff eingeführt, um eine Best-Practice-Ansatz in dieser Art von experimentellen Untersuchungen einzuführen. Das Verfahren wurde in der Pellet Felge nicht nur angewendet, wo die HBS vorhanden ist, sondern auch in der sogenannten "dunklen Zone" und andere Pellet radialen Positionen durch hohe Spaltgasblasendichte charakterisiert, dessen Porosität im allgemeinen nicht spezifisch quantifiziert ist. Die Studie ergab, dass Porendichte und Porengrößen vergleichbar zu denen, die in der HBS gefunden wurden, sind. Die Analyse der Brennstoffmikrostruktur zeigte systematische Präsenz von rund Subkörnern um die Poren und auf freien Flächen, was darauf hindeutet, dass ein Umstrukturierungsprozess in fieri sein könnte auch bei mittleren radialen Positionen, wenn auch in einem geringeren Ausmaß im Vergleich zu dem Pellet Peripherie.

In der Pellet Felge, bedeuten die Analyse der Porendichte und Porengröße als eine Funktion des lokalen Abbrands, dass Poren Vergröberung bei Erreichen $\approx$100 GWd /tHM offensichtlich ist. Ein erster Versuch, ein solches Verhalten auf der Hypothese basiert, zu erklären, dass der Tropfen der Porendichte zur Koaleszenz der wachsenden Poren zurückzuführen ist gegeben.

Das Modell wurde für den grundlegenden Mechanismus auf die Arbeit von White basiert, jedoch mit einer Modifikation, die die experimentellen Beobachtungen in dieser

Arbeit berücksichtigt hat. White modelliert das Porensystem gemäß einem System von vollständig überlappenden Platten. Messungen der Autokorrelationsfunktion der Porenphase durch Bildanalyse durchgeführt, zeigten ein Verhalten ähnlicher ein System von harten Kugeln. Daher wurde der Vergröberung Mechanismus geändert, unter Berücksichtigung der nächsten Nachbarn Statistiken für harte Kugeln. Dieses Modell wurde mit einem anderen vorhandenen Modell gekoppelt, die die Xenonverarmungs und Porenwachstum in der HBS und im Vergleich zu den experimentellen Daten beschrieben. Die änderung in der Vergröberung Mechanismus eingeführt verbessert die Vereinbarung mit dem Trend der experimentellen Daten, einen ersten Einblick über die wichtigsten zugrunde liegenden physikalischen Phänomene wahrscheinlich verantwortlich sein für Blase Schwellung in der HBS bietet.

Acronyms

DNB Departure from Nucleate Boiling

dpa displacements per atom

EBSD Electron Backscatter Diffraction

EOL End of Life

EPMA Electron Probe Microanalysis

FIB Focused Ion Beam

FIMA Fission of Initial Metallic Atoms

HBEP High Burnup Effects Program

HBRP High Burnup Rim Project

HBS High Burnup Structure

LOCA Loss of Coolant Accident

LWR Light Water Reactor

NFIR Nuclear Fuel Industry Research

PCMI Pellet-Cladding Mechanical Interaction

PIE Post Irradiation Examination

PWR Pressurised Water Reactor

RIA Reactivity Initiated Accident

SAM Scanning Acoustic Microscopy

SCV Smoothed Cross Validation

SEM Scanning Electron Microscopy

SIMFUEL Simulated Spent Fuel

SIMS Secondary Ion Mass Spectrometry

SNF Spent Nuclear Fuel

TEM Transmission Electron Microscopy

XRD X-Ray Diffraction

XRF X-Ray Fluorescence

1. Introduction

A journey of a thousand miles must begin with a single step

Lao Tsu

1.1. Background

Today, civil nuclear power supplies almost 11.5% of global electricity needs, from reactors in 31 countries. In 2015 in the European Union 27% of the electricity was produced by nuclear power. Approximately 85% of the current nuclear generated electricity comes from Light Water Reactor (LWR), i.e. reactors where water is used as moderator and coolant. The most common type of fuel used in LWRs is UO_2, and, sometimes, a mixture of UO_2 and PuO_2 (the so-called MOX fuels). The fuel is composed of cylindrical ceramic fuel pellets stacked in a fuel pin with metallic cladding, generally Zr alloys (Fig. 1.1).

The LWR reactor technologies were developed in the 1950s and improved since then. Thanks to the progressive accumulation of operational experience and to the technological progress, the average discharge burnup in LWR has historically increased steadily (Fig. 1.2) [1]. In less than thirty years, discharge burnups as high as twice the initial ones have been attained without compromising the fuel safety. The fast progress was possible due to a tight synergy between improved fuel design and deepened understanding of fuel behaviour, complemented by the availability of new materials with enhanced performance [2].

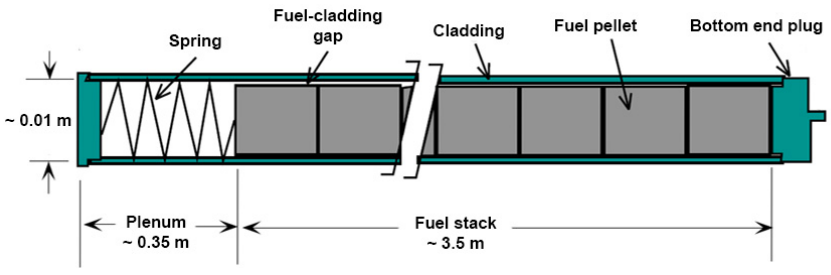

Figure 1.1.: Schematic of a LWR fuel rod.

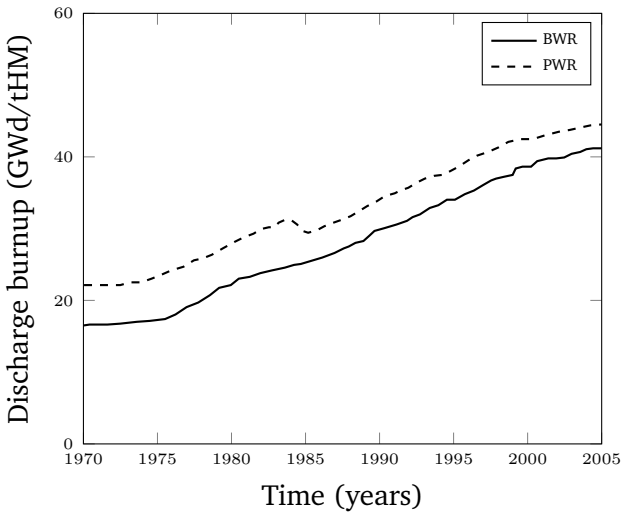

Figure 1.2.: Average discharge burnup trends in LWR [1].

One of the main driving factors for pursuing higher discharge burnups is the economic benefit for fuel cycle costs components that scale with fuel turnout, e.g., fuel fabrication costs, fresh fuel transport and processing costs [2, 3].

Secondly, higher discharge burnups imply that larger amount of power can be extracted before refueling, thus decreasing the need for fresh fuel. Practically, the ratio between the initial mass of fresh fuel loaded and the mass of spent fuel discharged scales inversely with the average discharge burnup. The reduction of volume of discharged spent fuel is an important driving force for increasing the average burnup, contributing to the sustainability of the fuel cycle. It also increases the operational flexibility, because the plant can operate longer between refueling outages [2].

Despite the benefits previously mentioned, several technological challenges arise when operating at high burnup. The increase of the average burnup impacts several aspects of the in-pile and out-of-pile fuel cycle and management. Regarding for instance the in-reactor fuel performance, operation at higher burnup would imply more severe thermo-mechanical regimes [3]. There are several life-limiting phenomena of particular concern in LWR operating at high burnup. For example, after the first cycles, while the burnup increases the pellet-cladding gap progressively closes causing mechanical contact, the so-called Pellet-Cladding Mechanical Interaction (PCMI). During PCMI the cladding stress state is reversed from a compressive state to a tensile stress state, intensified by increasing fuel swelling. This, combined with cladding embrittlement due to hydride accumulation and corrosion, could eventually lead to premature cladding failures [3]. The accelerated growth of fission gas release to the rod plenum systematically observed beyond 45-50 GWd/tHM [4, 5] is another critical issue, because the increased internal pressure contributes to the cladding stress state.

On a microscopic scale, energy production in nuclear fuels proceeds via slowing down of high energy fission products [6]. The two heavy ions, which have mass numbers

between 65-160 and energies in the range 70 MeV to 100 MeV, are the main source of radiation damage in the fuel matrix during in-reactor operation [7, 8]. The kinetic energy is transferred to the surrounding matrix mainly by electronic losses at the beginning and then progressively via nuclear collisions once the energy is decreasing (Table 1.1) [7, 9]. Other minor sources of radiation damage in the fuel in-pile[1] are high-energy electrons formed during β-decays, which can produce displacements by direct energy transfer or by ionization and excitation along their path, or the pair α-particle and recoil atom produced during α-decays [9].
Irradiation will form Frenkel pair defects (i.e. interstitials and vacancies) in the lattice whose concentration largely exceeds the equilibrium thermodynamic concentration. For instance, during each fission event, approximately 100000 defects are created [10] (see Table 1.1), most of which instantaneously recombine. Only ≈5000 U-defects survive the displacement cascade of the fission spike [10, 11]. Point defects surviving recombination can cluster together and evolve in extended defects such as dislocation and/or dislocation loops (for interstitials) or voids (for vacancies), introducing lattice distortions and structure modifications. The extent of damage accumulation depends on a complex balance between defects' creation and annealing, depending largely upon the local temperature and the local fission density. In addition to the formation of defects, one has to consider that each fission event brings a simultaneous change in chemistry by producing new elements, including volatile elements such as Br, I, Kr, Xe, Cs etc. [6], which can stabilize other formed defects, resulting in complex microstructural evolution. Variations of material microstructure following radiation damage and fission products accumulation influence fuel macroscopic properties such as thermal conductivity, diffusion, density etc., with important technological consequences on fuel performance and reliability [12]. The formation of the so-called High Burnup Structure (HBS) (see Section 1.2) is certainly one of the most spectacular and intriguing microstructural modifications affecting the high burnup fuel due to radiation damage effects. Having important influences on thermal, mechanical, and fission gas release behaviour under both normal and transient conditions, the study of the HBS has been a major research topic in the last decades [2, 4, 13–18].

Concerning the back-end of the fuel cycle, if on one hand higher average discharge burnup is beneficial in terms of reduction of the waste volume per unit energy produced, on the other hand it requires additional confirmations that fuel elements with high burnup can be stored and handled safely [19, 20]. The decay heat output increases roughly linearly with burnup, requiring longer residence time in spent fuel pool before moving to other long-term storage facilities being possible. Longer residence time in the pools might limit pool capacity, unless properly planned and managed [1]. In addition, the burnup dependence of the spent fuel isotopic inventory is a very important parameter that affects the back-end of the fuel cycle. In particular, the amount of α-emitters, main responsible of the long-term microstructural damage the fuel is hampered with, is a strong function of burnup. Each α-decay produces about 1400-1700 displacements, mostly due to the

[1] Concerning neutrons, the minimum neutron energy necessary to cause displacement is $E_n^{min} \sim$100 eV [9]. In thermal reactors like the LWRs most of the neutrons are thermalized (i.e., with energy $E <$ 1eV), therefore do not produce direct displacement.

Table 1.1.: Properties of different damage sources in ceramic nuclear fuels [8]

	Energy (keV)	Range (μm)	ν^a	N^b
LFP^c	95000	∼9	0.03/0.97	∼40000
HFP^c	67000	∼7	0.06/0.94	∼60000
α-particle	∼5000	∼12	0.01/0.99	∼200
Recoil atom of α-decay	95	∼0.025	0.90/0.10	∼1500

[a] Fraction of energy lost by elastic (nuclear)/inelastic (electronic) collisions
[b] Total number of defects produced, both anion and cation defects.
[c] LFP stands for light fission product; HFP stands for heavy fission product.

heavy recoil atom which forms a dense collision cascade [6]. The number of pair defect produced per α-decay event is a few order of magnitude smaller than the corresponding value occurring during fission events (see Table 1.1), but the spontaneous recombination during the cascade is negligible [8] and the timescales during which the phenomenon takes place are much longer than in-pile irradiation periods, spanning over thousands of years and more in the case of spent fuel disposal in a geological repository. The implications for the SNF safety are further discussed in Section 1.3.

1.2. The High Burnup Structure

The neutron capture cross section spectrum of the isotope ^{238}U shows a series of resonances at epithermal energies [21]. During irradiation, such captures convert ^{238}U into the isotope ^{239}U, which then decays into fissile ^{239}Pu after two subsequent β-emissions. In a cylindrical LWR fuel pellet, the maximum ^{239}Pu conversion takes place at the outermost part of the pellet (often called "rim" region), due to the configuration of the energy spectrum of the neutrons entering the fuel pins. The conversion efficiency decreases almost exponentially towards the pellet radius interior due to the epithermal neutron depletion caused by the neutron capture events [22, 23]. Therefore, the rim experiences higher fission density due to enhanced Pu concentration. This leads to a local burnup increase as high as twice or three times the pellet average burnup. The rim of the pellet is relatively cold, which implies low thermal recovery of the created defects. The intensified radiation damage paired with low thermal recovery results in a dramatic fuel restructuring process, namely the formation of the rim-structure or HBS.

Variations in the microstructure were observed between the end of the 1950s and the beginning of 1960s on UO_2 samples irradiated above 10% Fission of Initial Metallic Atoms (FIMA) (i.e., ≈75 GWd/tHM) [24–26]. Three main characteristics were noticed, i.e., enhanced plasticity of the material, evident increase of porosity with higher burnup, and appearance in the X-ray diffraction patterns of non-coherently diffracting material, suggesting structure amorphisation [24]. Later on, this fuel restructuring was called "rim effect" [23] or HBS [27]. At that time the burnup limits for applications in commercial

reactors were well below the level at which the HBS significantly appears, thus the phenomenon was not studied in detail.

A few decades later, as a consequence of the general trend of increasing the average discharge burnup (cf. Fig. 1.2), extensive research and development was directed toward assuring fuel reliability while extending fuel burnup. The HBS was observed again [14, 28–30]. Within the investigations of the High Burnup Effects Program (HBEP), the HBS was appointed as a possible cause of the increase in the fission gas release observed at high burnup, though precise quantification of the gas coming from the HBS was not obtained [14]. Significant concern was expressed from industry to evaluate the effects of the rim structure on fuel performance and safety. However, a lack of thorough understanding of the phenomenon emerged [14], paving the way for further research.

To respond to these needs, several programs and experimental campaigns have been launched in order to understand HBS characteristics and formation mechanisms. Several international research centres, fuel vendors and utility representatives committed in specific R&D international projects involving fabrication and characterisation of special irradiation fuels to study the HBS in LWR fuels.

One example of such programs is the High Burnup Rim Project (HBRP), initiated in 1991 [31]. The main goals of the project included (a) the identification of the conditions (burnup and temperature thresholds) for the HBS formation, (b) the investigation of the mechanisms responsible for the HBS formation, (c) the determination of amount of gas released during post-irradiation annealing to quantify the HBS contribution to the fission gas release, and (d) the characterisation of material properties relevant for fuel safety and performance, e.g., thermal conductivity [31]. The irradiation of these experimental fuels was carried out under "quasi" iso-thermal conditions in the Halden reactor. The samples did not exhibit the steep radial burnup and irradiation temperature gradients typical of normal irradiation in a commercial reactor, thus allowing well-defined parametric studies which could complement the results obtained on commercial fuels.

Following the HBRP investigations, it was determined that the HBS is formed when the fuel reaches a local burnup between 50-75 GWd/tHM and the local temperatures do not exceed $1100 \pm 100\,^{\circ}\mathrm{C}$ (Fig. 1.3) [31–33].

Another example of international R&D collaboration studying the HBS is the Nuclear Fuel Industry Research (NFIR) program, which is currently ongoing [34]. Among the main tasks of the project is the analysis to determine further quantitative data on high burnup UO_2 properties, but also the investigations of the behaviour of such fuel during Loss of Coolant Accident (LOCA). In addition, different types of fuel, including MOX, with various microstructure and additives are considered, in order to evaluate their performance at high burnup [34].

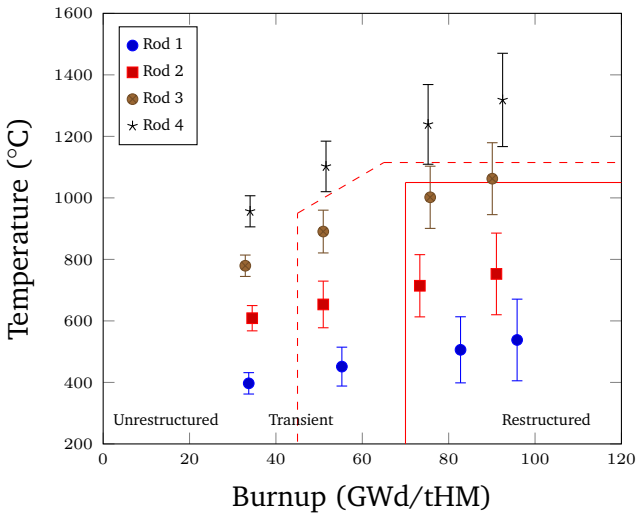

Figure 1.3.: Irradiation matrix of the HBRP project highlighting the burnup and temperature threshold for the HBS formation [17].

1.2.1. HBS characteristics

From the various observations three main features of HBS have been identified [22, 35–38]:

1. subdivision of the initial grains from typically 10 µm to 0.1–0.3 µm (Fig. 1.4) and absence of extended defects in the newly formed grains (Fig. 1.5),

2. round fission gas pores of micrometric size (Fig. 1.6),

3. Xe depletion from the matrix of newly formed small grains (Fig. 1.7).

Two types of subgrains have been reported associated with the HBS: polyedral subgrains [38] and round subgrains [39]. The first are formed in between the micrometric pores [11, 37], whereas the second are generally associated with free surfaces like the pore surfaces or the grain boundaries [37, 39], also far from the restructured areas [39]. Both high angle grain boundaries [40] and low angle grain boundaries have been observed, leaving doubts about the possible formation mechanism [32]. Some studies have concluded that neither variation in the local temperature, final burnup, nor fission rate had a significant effect on the sub-grain size distribution [33], but another study has shown a broadening in the grain size distribution, probably related to partial thermal growth active at intermediate radial positions in the fuel pellet [41].

The second macroscopic feature of the HBS is the porosity. The HBS pores are approximately spherical, surrounded by round sub-grains which give them a faceted appearance [35, 38]. The porosity evolution following formation and development of the HBS has been studied by Spino et al. [41]. The rate of porosity increase reaches ∼1% per 10

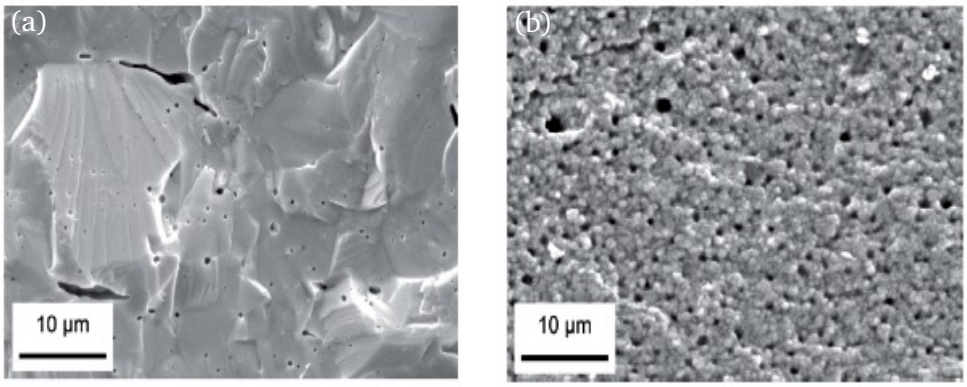

Figure 1.4.: SEM micrographs showing fresh fracture surface of (a) unirradiated UO_2 fuel, (b) UO_2 fuel with local burnup 75 GWd/tHM, highlighting the typical HBS morphology [22].

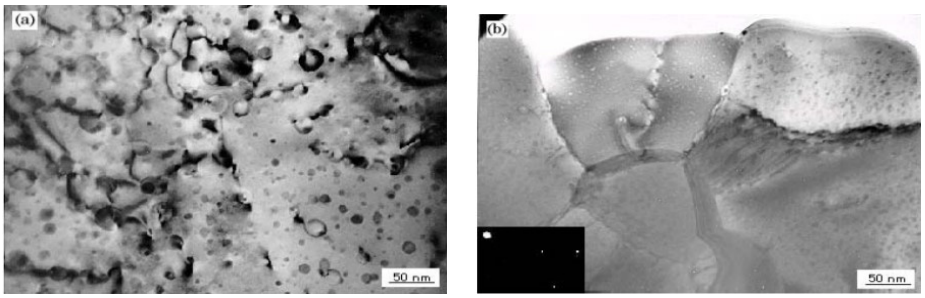

Figure 1.5.: TEM micrographs from the HBRP project [32] of (a) unrestructured fuel grain of a sample with burnup 55 GWd/tHM, (b) restructured subgrains of a sample with burnup 82 GWd/tHM. In (a) the tangled dislocations are visible. In (b) the new subgrains are free of extended defects.

GWd/tHM at the beginning of restructuring, but the porosity growth decreases to $\sim$0.6% per 10 GWd/tHM above $\approx$100 GWd/tHM [41]. The same authors noted that the rate of porosity growth approaches the fuel swelling rate in high burnup fuels, given that the depletion of xenon from the matrix is complete by $\approx$120 GWd/tHM, suggesting that at very high burnup the fuel swelling is governed only by porosity increase [42]. In the outermost periphery of fuels samples with average burnup 100 GWd/tHM, formation of remarkably extra-large pores has been observed [41, 43, 44] at local burnups corresponding to $\approx$150-300 GWd/tHM. This region has been attributed the name of "ultra-high" burnup structure [43]. The increase in the pore size corresponds to a drop in the pore density, as was observed by Spino et al. above $\approx$100 GWd/tHM [41]. Romano et al. [43] suppose that the pore growth is driven by pore pressurization and vacancy precipitation. The initial pore overpressure is varied till the experimental value of the pore radius are

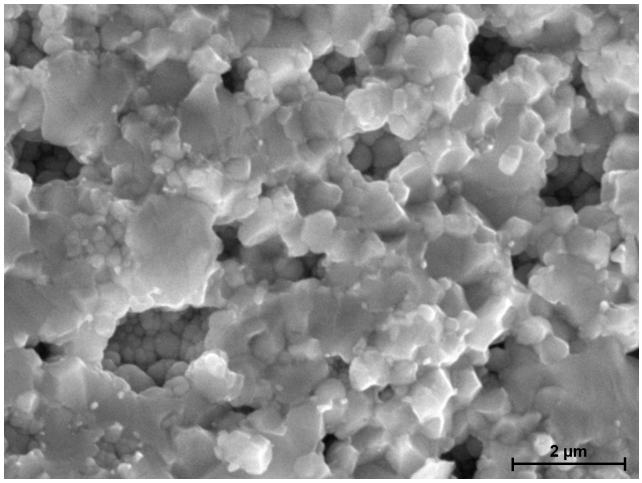

Figure 1.6.: SEM micrograph (fresh fracture) of a sample with average burnup 93 GWd/tHM. Large (micrometric) round pores are visible between the sub-grains.

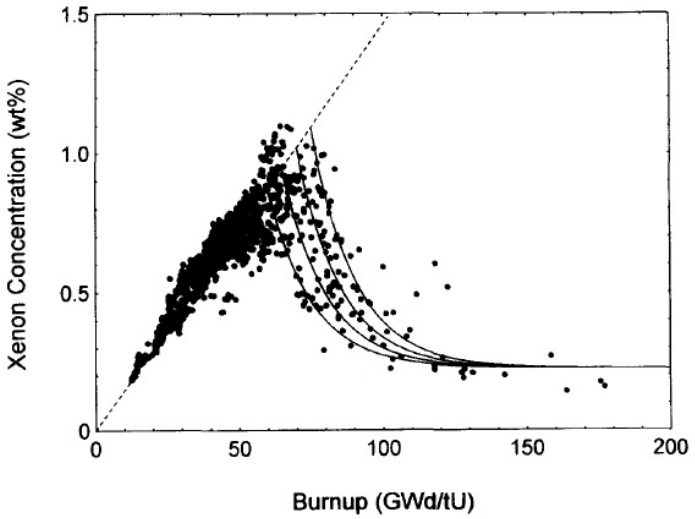

Figure 1.7.: EPMA data showing the Xe depletion from the fuel grains. Dashed line represents the calculated Xe production, solid lines represent the depletion model by Lassmann et al. [27]. Figure taken from [27].

matched. The pore density drop is a direct consequence of the pore radius increase, since the total porosity is supposed to be constant, in contrast to experimental evidence which shows that the porosity still increases at those burnups, albeit at a slower pace [41]. Other than coalescence, the pore density drop and concomitant mean pore radius increase could be due to Ostwald ripening, as proposed by Spino et al. [41]. They analysed the

kinetics of mean pore growth and pore density decrease based on the experimental data, showing a rate proportional to $t^{0.4}$ for the pore radius growth, and a rate proportional to t^{-1} for the pore density decrease, consistent with a Ostwald ripening coarsening[2] mechanism. However, the remarkable right skewness of the pore size distribution (see for example Fig. 4 in [41]) strongly contradicts the assumption that Ostwald ripening is active. Moreover, pore-contact onset was recognised (Fig. 7 in [41]), leaving doubts about the reliability of the kinetics analysis.

1.2.2. HBS formation and evolution mechanisms

The formation mechanism of the HBS is still source of different, often contrasting, interpretations. Several mechanisms have been proposed to describe the initiation of restructuring and the following development of the restructured region, as extensively reviewed in [22, 45].

Most interpretations ascribe the HBS formation either to a recrystallisation-induced transformation or to a micro-polygonisation phenomenon. Primary recrystallization is defined as the process by which the grain structure of the deformed material is transformed to a new structure, as a consequence of high stored energy of plastic deformation. New grains grow from regions present in the deformed state by the formation and migration of high angle grain boundaries, i.e., with misorientation higher than 15°–20° [46]. Polygonisation describes the rearrangements of dislocations forming low energy sub-boundaries and slightly misaligned sub-grains (misoriented by 1°–3°) [6, 47].

Based on TEM analyses, Nogita and Une proposed a model based on recrystallization-assisted Xe depletion from the fuel matrix [40, 48–50]. Tangled dislocations results from inhomogeneous defect accumulation due to radiation damage. Upon saturation, they are re-organized into grain boundaries of sub-divided grains of 20–30 nm with high angle boundaries, driven by the release of stored strain energy in the matrix. Subsequently, the newly formed nanometric grains grow sweeping out bubbles that precipitate at the new grain boundaries. Such bubbles coalesce into coarsened bubbles of micrometer-size upon fission gas accumulation.

Rest and Hofman [51, 52] explain grain subdivision through heterogeneous recrystallization. It is supposed that at the beginning of the irradiation a cellular dislocation structure is present, acting as sinks for irradiation-produced defects. As irradiation proceeds, impurities forming during fissioning diffuse heterogeneously as vacancy-impurities complexes to the interfaces where they pin the dislocation walls (called “nuclei”), reducing their mobility. Particularly efficient in reducing the wall mobility would be the overpressurized bubbles [53]. Some of the walls present no impurities and continue to undergo subgrain coalescence. The available stored energy is thus concentrated on fewer and fewer nuclei. Recrystallization is induced when the energy per nucleus is high

[2] Here and in the rest of the manuscript, I use the word coarsening as general term to indicate the process responsible for the pore/bubble merging into bigger ones. Coarsening may be driven by several different physical mechanisms, e.g., coalescence or Ostwald ripening. Please see Section 4.3 for further discussion.

enough that the creation of grain-boundary surfaces is offset by the creation of strain-free volumes, giving a net decrease in the free energy of the material.

A recrystallisation mechanism has been also proposed recently [54]. The original driving force for the grain subdivision is the accumulation of dislocation loops, which cause strain in the fuel matrix by increasing the lattice parameter. The lattice displacement will increase till a critical value is reached, above which matrix recrystallization would be favoured in order to decrease the accumulated strain energy.

Spino et al. [38] proposed grain subdivision as a possible consequence of the formation of pressurised gas bubbles via a loop-punching mechanism. However, such mechanism would be questionable when referred to the poorly deformable ceramic fuel.

Kinoshita [55] suggested that the recrystallisation could be induced by spatial instability in the concentration of diffusing defects.

Matzke et al. [23, 33, 56, 57] rejected recrystallization phenomena as explanation of grain subdivision and talks instead of micro-polygonization after accumulation of defects. The grain subdivision could be caused either by a cleavage process and microfracture probably related to the high pressure of athermally formed small fission gas bubbles [23, 56] or by re-organisation of tangled dislocations [33, 57].

A formation mechanism similar to this last one was also proposed by Sonoda et al. [32], based on the HBRP investigations, stressing possible "pinning effect" of fission product precipitates on dislocations and defect clusters which would favour grain subdivision.

Theoretical studies about nucleation, growth and accumulation of dislocation-type defects have also been performed [58–60]. In particular, in [60] dislocation dynamics is used to investigate the possible correlation between dislocations generation and HBS formation. It is found that upon reaching a critical dislocation density, polygonization starts from random fluctuations of the stress field prior to eventual recrystallization.

Recent synchrotron-based experimental X-Ray Diffraction (XRD) investigations [61] have shown that the formation of the subgrains originates from polygonisation of a parent grain. It is also supposed that the subgrain formation is linked to the relaxation of local stresses [61].

On the basis of the experimental evidences reported in [37] according to which Xe depletion preceeds grain subdivision, Baron et al. [11] proposed a four-step model for the HBS formation and evolution. First, a network of tangled dislocation is formed due to accumulation of irradiation-induced defects. Secondly, the lattice distortion induced by tangled dislocations leads to nano-scaled energy gradients, which would favour vacancies migration towards dislocations in order to relax the locally accumulated energy. These nanometric bubble can stabilize and start growing by accumulating gas and vacancies (step three). Being pressurised, the bubbles become quasi-spherical in order to maximise the volume to surface ratio. Finally, grain subdivision proceeds via polygonisation from the micrometric pores.

Despite extensive investigation, a comprehensive model predicting radiation effects on the fuel microstructure and its evolution has not been established yet. Discussion is also ongoing about the parameters affecting HBS formation and propagation, such as external hydrostatic pressure, initial fuel grain size, addition of additives (e.g. gadolinium

or chromium), the instantaneous fission density, and the local concentration of fission products [11].

In addition to the models here summarised, other models specifically developed for fuel performance codes exist. The discussion of those is postponed to Chapter 4.

1.2.3. Implications of HBS formation on fuel performance

In the assessment of the HBS impact on fuel performance, the attention focussed on three main aspects: (a) the thermal conductivity degradation and potential detrimental effects on the maximum temperature at the centre line of the fuel pellet, (b) the fission gas behaviour in the restructured regions and its release from the HBS, and (c) the mechanical interaction between fuel and metallic cladding, which is tightly bounded to the fission gas swelling and porosity increase in the HBS.

Given the importance of the thermal conductivity in determining the fuel temperature profile during irradiation, the investigations have been several (see [62] and references in it). Beneficial effects of the HBS formation on the lattice thermal conductivity have been shown, following the reduction of point defect and gas concentration inside the grains [18,63] and the precipitation of high conductive metallic phase [63]. However, the steep increase in porosity might offset the intrinsic recovery, acting as a thermal barrier, ultimately favouring fission gas release from the interior of the fuel pellet [64].

Another matter of concern is the role of HBS in fission gas release at high burnups. First investigations suggested that the enhanced fission gas release seen at high burnup was due to the HBS [14]. Instead, it is now generally accepted that most of the fission gas depleted from the grain interior (cf. Fig. 1.7) is retained in the micrometric pores, as shown by micro-coring techniques like Secondary Ion Mass Spectrometry (SIMS) [5, 65–68], X-Ray Fluorescence (XRF) [69] or three-dimensional sample reconstruction via image analysis [70] and by retained fission gas analysis, e.g., by annealing in a Knudsen cell [17, 44]. The retained fission gas contributes to the fuel swelling, increasing the loading on the cladding during PCMI [71]. On the other side, PCMI can influence the development of porosity [50].

Despite the initial concerns, various studies performed so far indicate that during normal operation, the HBS formation does not pose a safety issue [22, 72], and today's fuel normally operates at burnup levels which encompass the presence of the HBS.

The assessment of the HBS role on the high burnup fuel performance during accidental transients is much more difficult, due to the concomitant effects of other degradation mechanisms acting both on fuel and cladding at prolonged exposure to the irradiation field and high temperatures in the core (e.g., radiation damage, corrosion and hydride precipitation in the cladding).

During Reactivity Initiated Accident (RIA), high burnup fuel can fail prior to the occurrence of Departure from Nucleate Boiling (DNB) (the so-called 'hydride-assisted PCMI failure') [73]. When the PCMI load is produced primarily by solid thermal expansion of the fuel, the HBS does not have a strong impact on the reduction of the failure threshold [73].

However, at later transient stages, pore rapid pressurization can have influence on the fission gas release and cladding failure [73, 74]. Similarly, during LOCA the main concern with the formation of the HBS is related to the amount of fission gas loading given the high local inventory trapped in the micrometric pores, and the relocation or dispersal of fuel fragments [75, 76]. The intergranular gas inventory is probably one of the more relevant parameters to predict the high burnup fuel behaviour during accidental events [76, 77]. For instance, in his analysis of the CABRI-Rep and NSRR RIA test, Lemoine [74] highligthed how highly overpressurized bubbles, like the ones that are present in the HBS, can behave like hot spots, contributing to worsen the mechanical loading on the cladding and to its early failure at high burnup.
Fuel fragmentation tests simulating LOCA conditions at Studsvik have determined that the average burnup threshold for fuel fine fragmentation lies in the range 60-75 GWd/tHM [78]. This burnup level is well beyond the HBS formation threshold at the pellet rim. An immediate link between the presence of HBS and the pulverization of the fuel was established [75]. It has been shown that the HBS area are prone to fragmentation [68], but also fragments from non restructured areas have been observed [78, 79]. Several interacting and concomitant factors influence the fuel cracking and fragmentation behaviour, such as the rod internal pressure, but also the local cladding constrain plays a role [80]. The specific contribution of the HBS to fuel fragmentation remains at present unclear.

The HBS formation at the pellet periphery is thought to have beneficial effects on the PCMI, because the fuel restructuring is paired with a restoration of the lattice parameter [81] and an overall softening of the fuel, as shown by microhardness measurements [82].

1.3. Spent high burnup fuel evolution during storage

Safe, secure and sustainable management of growing inventories of radioactive waste and Spent Nuclear Fuel (SNF) has received considerable public attention and pressure, especially following the increased perceived threat of terrorism and occurrence of nuclear accidents. For instance the Fukushima Daichii accident has triggered a prompted revision of nuclear and spent fuel safety international guidance [83]. The environmental sustainability and security of nuclear waste is a key aspect to assure public acceptance of the nuclear energy as a viable and effective source of clean, carbon-free energy [84, 85].

When it is discharged from the reactor core, the spent fuel element temperature is too high to allow dry-handling or reprocessing, due to the decay power of short-lived nuclides produced during in-pile operation. As a consequence, SNF elements are kept for several years in cooling ponds till remote manipulation and transportation are possible. After the cooling in the reactor pool, the back-end of the open fuel cycle comprises three main steps [85]:

- Handling and transportation
- Storage in a temporary/interim storage facility

- Final disposal in a geological repository.

The interim storage was conceived as a temporary solution to last a few decades while awaiting for transport to reprocessing plant or to geologic repository, but extended storage of SNF is nowadays considered in several countries due to the pending issue in the licensing process of the facilities assigned to final disposal [20, 86]. International programs [19, 20, 86, 87] have been launched to evaluate fuel and materials performance under wet and dry storage and to assess the possible implications of prolonged interim storage on SNF management, including handling and transport.

The primary safety functions of the SNF rods comprise ensuring radiological confinement and structural integrity [83]. Integrity and stability of the waste forms are influenced by temperature, chemical-physical property evolution, and radioactivity level [85, 88, 89]. The α-decays dominate the long-term activity and dose of the SNF, due to the long half-life of many α-emitters [90]. Concerning the fuel, several studies have shown that radiogenic He accumulation and associated alpha-damage in the fuel matrix are responsible for most microstructural damage and alteration of the fuel pellet occurring after the end of irradiation in the reactor [91–97]. The damage associated to the α-decays of transuranic elements is particularly important for high burnup fuel, since the inventory of many transuranic α-emitters tends to increase with burnup (Fig. 1.8) [2]. Consequently, the amount of He and the corresponding α-decay per fuel gram accumulated in LWR UO_2 increase as the average burnup increases (Fig. 1.9) [93].

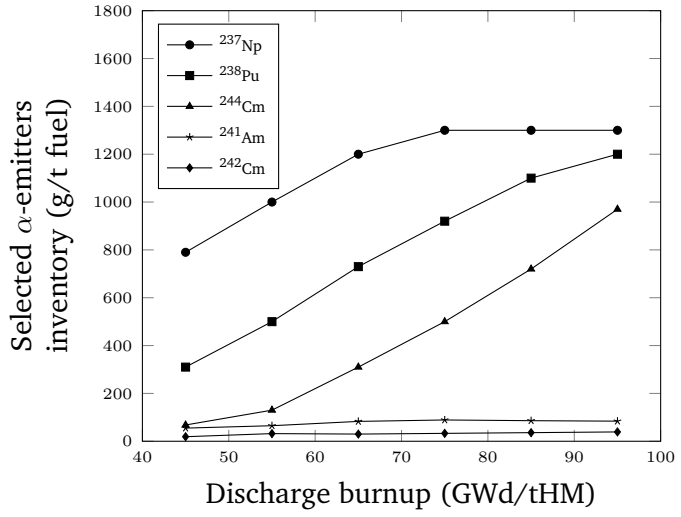

Figure 1.8.: Dependence of selected α-emitters concentrations on discharge burnup. The concentrations were calculated using KORIGEN [98] at the end of fuel life.

The ageing accumulated by spent fuel currently available for experimental studies does not cover the time scale of interest for safety assessment of extended storage (i.e., hundreds of years) and no direct measurements are available. UO_2 fuels doped with short-lived alpha emitters (e.g., $^{238}PuO_2$) can be used to simulate spent fuel during long

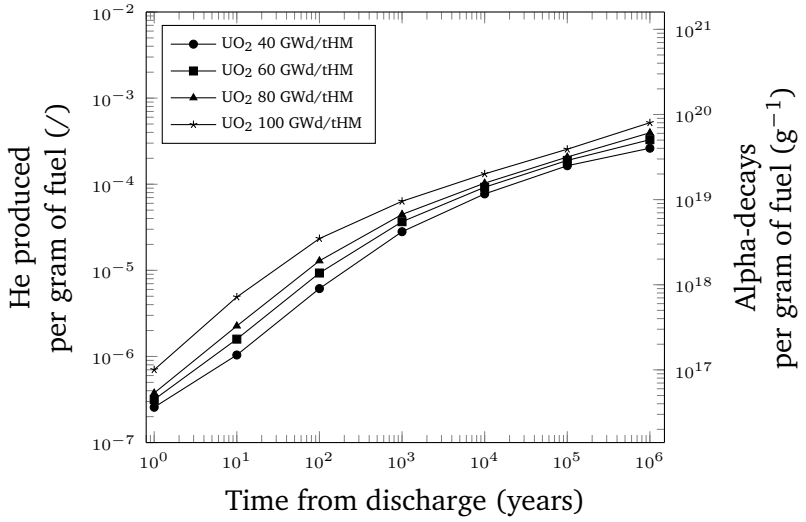

Figure 1.9.: He production during storage in LWR UO_2 fuels at different values of discharge burnup [93].

storage times under accelerated conditions [92–95, 99]. A key aspect is the He behaviour in the fuel. If He accumulates in the fuel matrix it causes fuel swelling, whereas if it is released to the plenum it could further pressurize the SNF rod during extended storage [100]. In both cases, it could have implications for spent fuel storage safety assessment since it increases the load of the cladding [100–102].

Experimental studies on polycrystalline UO_2 with infused [103] or implanted [104] He and calculations [105] indicate a limited solubility of He in the fuel matrix. Partially, the radiogenic He could be accommodated in existing fission gas bubbles, especially in the HBS, but most of it is expected to precipitate in nanometric bubbles [94], causing matrix swelling [92, 94]. The possibility of local embrittlement with consequent microcracking and He release to the plenum is still a matter of debate. Despite calculations showing that He bubble overpressurisation should not lead to microcracking of the fuel grains during 10000 years of storage [102], degradation of the SNF mechanical integrity with time cannot be completely excluded [94]. An increase of fuel hardness as a function of the cumulated dose has been measured in alpha-doped fuels [92]. If such increase could be correlated to a fracture toughness decrease, brittle fracture with consequent gas release might be possible [94]. However, so far such hypothesis is only speculative, since scarce results on fracture toughness and hardness of aged spent fuel are available [38, 82, 106]. Comparison between results from LWR spent fuel and alpha-doped analogous might not be straightforward, due to the combined effect of in-pile and out-of-pile damage accumulation in the real spent fuel.

1.4. High burnup fuel mechanical properties and porosity: experimental characterisation

When assessing the integrity of SNF, mechanical properties and porosity are two key macroscopic characteristics of high burnup fuel, given their importance in life-limiting phenomena such as PCMI and fission gas release.

Relatively scarce PIE results relate the mechanical properties of irradiated UO_2 to its local microstructure. The following section presents an overview of the available experimental data relating the fuel mechanical properties to local structure characteristics. The porosity, in particular the intergranular porosity, which accounts for most of the void fraction, is thought to have a major impact on the mechanical properties while reducing the load-bearing area [107–109]. In previous sections, the primary role for the safety and performance of the fuel during irradiation was described. The main experimental works performed to characterize the bubble population, with particular focus on the HBS, are briefly recalled in Section 1.4.2.

1.4.1. Fuel mechanical properties

Nowadays, microhardness and elastic moduli are among the few mechanical properties that can be directly measured on irradiated fuel with a spatial resolution comparable to the microstructural heterogeneities of a pellet radial cross-section. In the remaining part of the document, the focus will be on these two properties.

Microhardness and elastic moduli of irradiated UO_2 are affected by several microstructural factors, primarily accumulation of defects due to irradiation, oxygen to metal ratio, presence of fission products (both in solid solution and as secondary phases precipitates), porosity and grain size.

First studies on the effect of irradiation on single crystal UO_2 microhardness were performed by Bates [110]. A rapid increase of Knoop microhardness was reported already at fission density of 1×10^{14} fissions cm^{-3}, with an initial relative increase in microhardness of +2% which was rapidly growing further to +11% at 3×10^{15} fissions cm^{-3}. Kim and Kirihara [111] reported a monotonic increase of polycrystalline UO_2 microhardness in the range 1×10^{14}–1×10^{17} fissions cm^{-3}, followed by a decrease at dose value of 1×10^{18} fissions cm^{-3}. The trend was correlated to the evolution of the lattice parameter reported by Nakae *et al.* [112], which, after a first increase, shows a recovery attributed to annhilation of the saturated irradiation-induced defects [112]. No data is available in the range 1×10^{18}–1×10^{20} fissions cm^{-3}, but a further relative increase of +20-30% when exceeding 1×10^{20} fissions cm^{-3} is reported [110].

As the irradiation proceeds, fission products both in solid solution and as precipitates accumulate in the fuel. Vickers microindentation tests were performed on Simulated Spent Fuel (SIMFUEL) specimens simulating irradiated samples with burnup up to 180 GWd/tHM [82]. A slow hardening as a function of burnup was determined up to 80 GWd/tHM, and then the chemical hardening stagnates up to the maximum value of burnup measured, with a relative increase in the measured microhardness of ≈40% [82].

In-pile measurements of the effect of irradiation on the Young's modulus of UO_2 were carried out by Baranov and co-workers [113]. After an initial decrease, the Young's modulus was shown to increase monotonically and saturate rapidly. The initial decrease was attributed to a weakening of the atomic bonds in the lattice due to rapid increase in the concentration of point defects. As the irradiation proceeds, the competitive effect of dislocation pinning by these defects would cause the observed increase of the modulus of elasticity [113]. However, initial irradiation-induced densification might play a role in determining the observed trends. PIE to determine the Young's modulus in irradiated UO_2 fuel has been performed by Laux et al. [114] using acoustic microscopy. The results showed a progressive decrease of the fuel Young's modulus by up to 20-25% at ≈100 GWd/tHM due to accumulation of radiation damage and fission products. The same trend was reported on SIMFUEL by the same team [115].

The effects of oxygen to metal ratio on microhardness was studied in [116]. Increase of the measured microhardness was reported starting from deviation in the O/M of +0.01, which resulted in a relative increase of approximately +15%, rapidly saturating at +35-40% thereafter. Concerning the elastic modulus of UO_{2+x}, data are extremely scattered, due to strong influence of U_4O_{9-y} on the results. Martin [117] recommended a linear decrease of the Young's modulus with increasing of deviation from stoichiometry.

The relationship between fuel microhardness and porosity has been investigated by Bates [110] and Spino et al. [82]. An exponential decrease of UO_2 hardness with porosity was shown in [110]. A similar correlation was proposed by Spino et al. [82] to correlate Vickers microhardness to the local porosity in irradiated UO_2 in the burnup range 40-100 GWd/tHM.

So far, the porosity dependence of the UO_2 Young's modulus has been experimentally studied only for non-irradiated material [115, 117–119]. Typically, these expressions are linear correlations whose slope reflects the geometry of the lenticular pores in sintered solids [120].

1.4.2. Porosity

Porosity and pore size distribution are usually determined using two-dimensional (2D) quantitative image analysis of Optical Microscope (OM) and Scanning Electron Microscope (SEM) micrographs, either on polished or on fresh fracture surfaces. Rest et al. [121, 122] reported the intergranular bubble density per grain-boundary surface area measured on fresh fracture surfaces in U-Mo fuels showing a structure similar to the HBS. The experimental data on porosity and the bubble size distribution were used to support the validation of analytical models for nucleation and growth of fission gas bubbles. Une et al. [16, 50] compared the areal bubble size distribution of PCMI-free UO_2 samples and fuel pellets under PCMI conditions with burnup in the range 86-90 GWd/tHM. The study was aimed at investigating the influence of PCMI restrain on rim porosity formation using both OM and SEM micrographs of polished cross sections. It was concluded that the presence of an external pressure hinders the porosity development in the fuel [50]. Recently, Noirot et al. [68] analysed the evolution of the bubble size distribution on a

fuel disc of 103 GWd/tHM after annealing at 1200 °C. In addition to the "classical" HBS bubbles which swelled during the annealing test, appearance of very small intergranular bubbles (with diameter in the range 0.2–0.4 μm) was reported after the annealing test. Using SEM micrographs, Romano et al. [43] described the evolution of the rim bubble 2D diameter in the ultra-high burnup region of PWR UO_2 sample irradiated up to an average burnup of 105 GWd/tHM. In all cases, the data are in forms of histograms, obtained from 2D image analysis.

Extensive results have been reported by Spino and co-workers [38,41] on LWR fuel samples in the burnup range 40-100 GWd/tHM not only in 2D, but also in three-dimensional (3D) applying stereology. The methodology employed and its implications on the accuracy of the results are discussed in Section 2.4.3.

1.5. Research objectives and thesis outline

The principal goals of the research presented in this thesis are: (i) the experimental investigation of high burnup fuel mechanical properties and their correlation to the local microstructure, in particular the porosity, for which scarce PIE exist in literature; (ii) the experimental determination of the evolution of the pore population in the HBS by means of advanced image analysis techniques. Experimental data relating the mechanical properties of irradiated UO_2 to its local microstructure are of practical importance to ameliorate the understanding of how high burnup fuel properties can affect the PCMI. The tailored experimental investigations carried out in this thesis are used to improve the fuel mechanical property correlations available in fuel performance codes. In addition, an experimental campaign has been started to study the effect of decay damage on the fuel microhardness, which is relevant for safety assessment during spent fuel storage. Finally, the experimental data about the pore size characteristic collected in this work is complemented by a preliminary semi-empirical model to evaluate the fission gas behaviour in the HBS, particularly the mechanism inducing pore coarsening at very high burnup (above 100 GWd/tHM).

Chapter 2 introduces the characteristics of the fuels analysed in this work and the experimental techniques employed. In this chapter, also an improved methodology for the analysis of the pore-size distribution determination in the HBS is introduced, highlighting its advantages compared to the methodology employed so far.

Chapter 3 focuses on the experimental results. The first part of the chapter deals with the ageing study, in particular, the evolution of the microhardness of high burnup fuels, with focus on the effects of decay damage. In the second part, the measured fuel mechanical properties are compared to fuel materials property correlations available in fuel performance codes. In the last part, the new methodology introduced in Chapter 2 to measure the pore size distribution is used to compare the pore population characteristics in the HBS and in other radial zones of the fuels characterised by high bubble precipitation. The study of the pores characteristics is complemented with observations of the underlying grain structure, showing grain sub-division phenomena similar to what usually observed in the HBS, but at intermediate pellet radial locations. Finally, results of the pore density and mean pore diameter in the HBS as a function of the local burnup are presented.

Chapter 4 introduces a preliminary model that describes the observed evolution of the pore density and mean pore dimension in the HBS. The model is a first attempt towards a more physics-based description of the porosity growth in the HBS, albeit with an engineering approach in order to keep the level of complexity suitable for possible future application in fuel performance codes and employing as few parameters as possible.

In Chapter 5 the summary and conclusions of the work are drawn, including recommendations for future work.

2. Materials and experimental techniques

> It's not an experiment if you know it's going to work
>
> *Jeff Bezos*

Abstract *This chapter presents the characteristics of the fuel samples investigated, the experimental techniques and methodologies employed, namely the Vickers microindentation, the acoustic microscopy and the scanning electron microscopy coupled with quantitative image analysis. The stereological method commonly used to derive three-dimensional characteristics of the fission gas pores in the fuel is reviewed and its assumptions discussed on the basis of latest findings. An alternative methodology, based on the use of the adaptive kernel estimator, is proposed, without a-priori assumptions on the underlying pore size distribution. The approach shows advantages compared to the classical one based on the histogram in terms of detail in the description and accuracy within the experimental limits. Part of this chapter has been published in [123].*

2.1. Fuel samples

The commercial samples analysed were all cut from Pressurised Water Reactor (PWR) rods. They were cut at axial positions of the father rods with a flat axial burnup profile from the high power region of each rod, as measured from gamma scanning. The main fuel pellet characteristics are summarised in Table 2.1.

Table 2.1.: Pellet design data of the PWR fuel samples used in this work.

Average burnup (GWd/tHM)	Initial enrichment (wt% ^{235}U)	Initial fuel density (g cm^{-3})
67	3.95	10.52
80	3.8	10.40
100	3.5	10.40
102	3.5	10.40

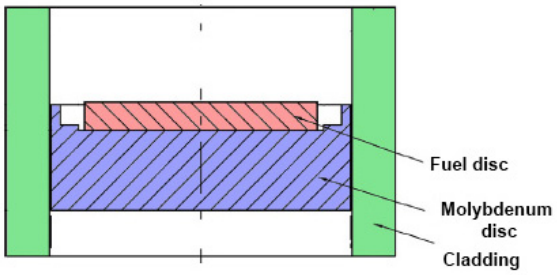

Figure 2.1.: NFIR fuel discs irradiation concept [68].

In addition, two special irradiation fuel discs irradiated in the Halden reactor part of the NFIR project [34] were used for investigation. The fuel rod was composed of fuel discs with ≈1 mm thickness and 8.2 mm diameter. Each fuel disc was sandwiched between Mo-discs to limit the temperature gradients in the radial direction. The fuel rod was filled with helium at an operating pressure of 8 MPa (Fig. 2.1) [34, 68]. The characteristics of the samples here analysed are reported in Table 2.2.

Table 2.2.: Summary of the irradiation parameters of the NFIR fuel discs used in this work.

Average burnup (GWd/tHM)	Initial grain size[a] (μm)	Initial enrichment (wt% ^{235}U)	Initial fuel density (g cm^{-3})	Mean irradiation temperature (°C)	Restrain pressure (MPa)
103	10	19.77	10.41-10.57	620	8
103	4	19.77	10.41-10.57	620	8

[a] Value obtained from 2D mean linear intercept.

Before carrying out the measurements, the samples were embedded in epoxy resin, carefully ground and polished in several steps using diamond suspensions with particle size from 12 µm to 1 µm. In order to perform investigation of the grain structure, the sample surface was scratched along the pellet diagonal using a diamond tip to expose a fresh fracture surface.

All the sample preparation steps and experimental investigations were performed in the hot cells (Fig. 2.2) or in shielded glove boxes.

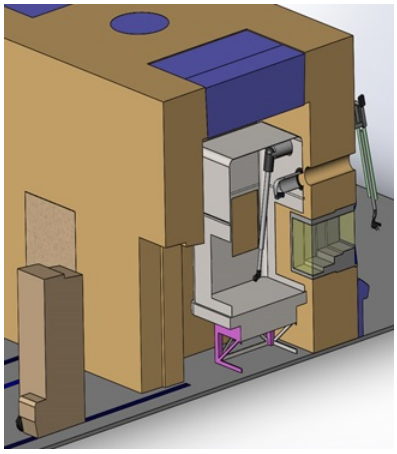

Figure 2.2.: Schematic representation of a hot cell installed at the JRC-Karlsruhe site of the Directorate for Nuclear Safety and Security where PIEs of the irradiated samples were performed.

2.2. Vickers microindentation

A general definition of hardness is not straightforward, since it is not a unique property of a material, rather a measure of the material response to an imposed external force depending on the specific test procedure employed [124]. Here I focus on static indentation tests, and in particular on Vickers indentation tests. In this type of measurements, a pyramid with apex of 136° is forced on the polished surface of a sample, leaving an impression on it (see Fig. 2.3). The load per unit area of impression is given as a measure of the sample hardness. When the applied load lies in the range 0.0098–1.96 N we speak about microhardness [125]. The Vickers microhardness HV (GPa) was computed using the following relation [126],

$$HV = 0.0018544\frac{P}{d^2} \tag{2.1}$$

where P (N) is the applied maximum load and d (mm) is the average length of the two diagonals of the indentation ($d_1$and d_2 in Fig. 2.3).

In this work, a Micro-Duromat 4000E microhardness Vickers tester, incorporated in a shielded LEICA Telatom 3 optical microscope, was used. The measurements were performed at room temperature under N_2 protective atmosphere. The diagonals of the imprints were measured from images acquired with the optical microscope at magnification 1500x. Generally, a 0.98 N load was employed, with a loading rate of $9.8 \times 10^{-3}\,\mathrm{N\,s^{-1}}$ and a hold time at the maximum load of 12 s, following reccommendation from the ASTM standard for Vickers indentation on ceramics [126]. Only in the case of the ageing study (see Section 3.1.1) a different set of experimental parameter was used, namely a 0.49 N load, a loading rate of $0.1\,\mathrm{N\,s^{-1}}$ and a hold time at the maximum load of 5 s. The choice

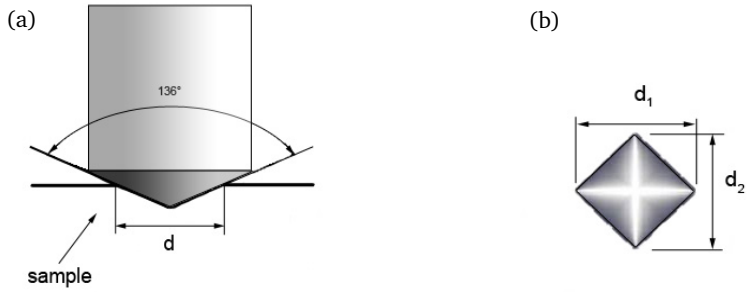

Figure 2.3.: (a) Schematic representation of a Vickers microindenter pyramidal tip. (b) Example of imprint left on the sample surface.

was done in order to compare the results with previous measurements reported in [82] using the same experimental parameters.

2.3. Acoustic microscopy

Scanning Acoustic Microscopy (SAM) is a powerful, non-destructive technique for imaging and measuring properties of various materials [127]. A scanning acoustic microscope has been developed and adapted to measure the elastic properties (i.e., Young's modulus E and shear modulus G) of irradiated UO_2 fuel in a hot cell [114, 118]. The acoustic sensor is composed of a piezoelectric crystal attached to the flat end of a silica sensor which focuses the ultrasonic waves through a spherical lens onto the sample surface (Fig. 2.4). The sample is mounted on a translational stage equipped with micrometric motors, and it is immersed in a coupling fluid that ensures acoustic wave propagation. For safety reason, no water could be employed in the hot cell; therefore methanol is used as coupling fluid. The device is remotely controlled through an electronic system placed outside the hot cell [118].

When investigating thick samples, a surface acoustic wave (called Rayleigh wave v_R) can be excited (see Fig. 2.4). Upon defocussing the sensor from the sample surface to the sample sub-surface, the Rayleigh wave interferes with the normal ray. The output of the transducer varies as a function of the defocussing distance z. The resulting pseudo-periodic signal is called acoustic signature $V(z)$ [127]. From the measurement of the pseudo-period Δz (m) of the acoustic signature, the Rayleigh wave can be computed using the following formula [114, 128]:

$$v_R = \frac{v_{cf}}{\sqrt{1 - \left(1 - \frac{v_{cf}}{2f\Delta z}\right)^2}} \tag{2.2}$$

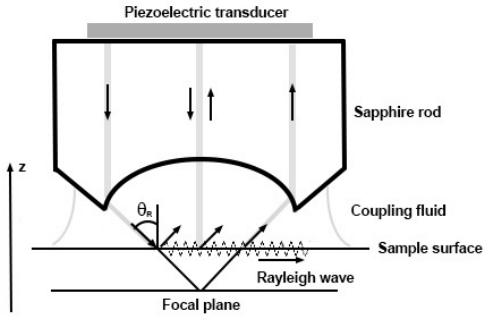

Figure 2.4.: Schematic representation of reflection SAM.

where v_{cf} ($\mathrm{m\,s^{-1}}$) is the signal velocity in the coupling fluid and f ($\mathrm{s^{-1}}$) is the frequency used.
It has been shown [114, 118] that the Young's modulus is related to the Rayleigh velocity according to the approximate relationship

$$E \approx 3\rho {v_R}^2 \tag{2.3}$$

where E (Pa) is the Young's modulus, ρ ($\mathrm{kg\,m^{-3}}$) is the sample local density, and v_R ($\mathrm{m\,s^{-1}}$) is the measured Rayleigh wave velocity. The sample local density can be empirically related to the Rayleigh wave velocity using the following equation [129]

$$\rho = 3.3 v_R + 2.0495 \cdot 10^3 \tag{2.4}$$

where all the symbols have the same meaning as in (2.3). Combining (2.3) and (2.4), the Young's modulus can be calculated from the single measurement of v_R.

2.4. Scanning Electron Microscopy and quantitative image analysis

In order to characterise the microstructure of heterogeneous (multiphase) materials, image analysis can be employed to directly extract microstructural descriptors of interest [130, 131]. In this work, I employed it mainly to characterise the fuel pores features, including fractional area, pore shape and pore size distribution at various samples locations. The main drawback of such approach is that it is operator dependent, since it is the operator that sets the detection threshold. Moreover, grain pullout or surface artifacts can affect the measurements [15]. Weather the last two factors can be reduced through careful sample preparation, the subjectivity of the threshold mask can only be tackled using semi-automatic threshold algorithms available in image processing softwares. Aware of the limitations, the technique is, nevertheless, the best available non-destructive way to direct quantify porosity in irradiated fuel [15]. In contrast to

immersion density measurements, which enable to obtain only an average value of the porosity in the whole pellet, image analysis allows direct visualisation of porosity gradients along the pellet radius [42]. This technique has been successfully applied in the past in a number of investigations [38, 41, 43, 50, 68, 70, 121, 132].

2.4.1. Image acquisition and processing

The Scanning Electron Microscopy (SEM) images were acquired using a shielded JEOL 6400® scanning electron microscope equipped with a MaxView® software package from SAMx. Previous works [38, 41] have shown that the pore size distribution in the HBS can be very polydisperse. In order to measure both small and large features, one possibility is to acquire images using different magnifications. From each image, only features within the appropriate size range are measured, and then the data from the different magnifications are combined [133].
In order to broaden the range of pores that could be measured and improve the accuracy of the measurements, the images were acquired using a low magnification (500x) and a high magnification (1500x). The images had a spatial resolution of $\approx$0.15 μm and of $\approx$0.05 μm, respectively.
The images were then processed using the softwares ImagePro Analyzer 7.0®, ImageJ and Photoshop CS5®. The first step in the image processing was a background noise reduction using a 3x3 median filter. Secondly, the pores were separated from the background creating a binary mask, based on the Otsu thresholding algorithm [134]. The pixels whose grey level is lower than a threshold level are considered to belong to the pores, whereas the rest belongs to the background. The result of the masking is the creation of a binary image (Fig. 2.5b).

As previously mentioned, the setting of the threshold in the mask is a subjective step in image processing that can have a major impact on the measured value of porosity. In order to evaluate the impact on the areal porosity value determined via image analysis, I varied the threshold mask level around the value automatically detected by the software. An example of such study is reported in Fig. 2.6. Taking a range of $\pm$2 grey level values around the one automatically detected, the maximum error introduced in the measurement of porosity is $\approx$2%, in agreement with the estimations in [15, 42].
Once the pores have been separated from the background, the total pore area is given by summing the areas of the measured pore sections after the merging. The areal porosity is calculated as the ratio between the total pore area and the image area.

In addition to the porosity measurements, also other microstructural descriptors can be obtained from the image analysis. The ones relevant to this work are reported in the next section.

2.4.2. Microstructural descriptors

Microstructural descriptors provide information about the statistical geometry of heterogeneous materials [135, 136]. The fuel is considered as a two-phase, statistically

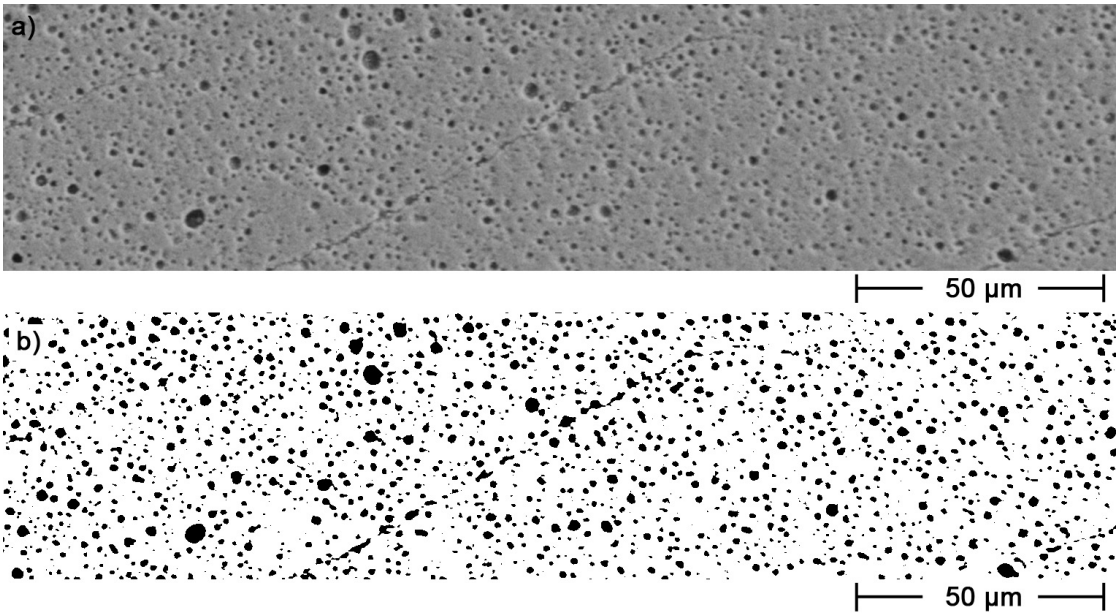

Figure 2.5.: Example of image thresholding to measure the fuel porosity and related properties: (a) original secondary electron SEM image; (b) binary mask obtained applying the Otsu thresholding algorithm [134].

homogeneous medium composed of the pore phase and the fuel matrix. The microstructural descriptors used to characterise the fuel pore phase, called phase 2 in the following, are briefly summarised here below.

n-point correlation function

For the pore phase we define the indicator function [131, 135]

$$\mathcal{I}(\mathbf{x}) = \begin{cases} 1 & \text{if } \mathbf{x} \in \text{phase 2} \\ 0 & \text{otherwise} \end{cases} \tag{2.5}$$

where $\mathbf{x}$ is a generic point in the fuel. The n-point correlation function is given by the following equation [135]

$$\mathcal{S}_n(\mathbf{x}_1, \mathbf{x}_2, ..., \mathbf{x}_n) = \langle \mathcal{I}(\mathbf{x}_1)\mathcal{I}(\mathbf{x}_2)...\mathcal{I}(\mathbf{x}_n) \rangle \tag{2.6}$$

where the brackets $\langle\ \rangle$ indicate the volume average. The n-point correlation function gives the probability that n points $\mathbf{x}_1, \mathbf{x}_2, ..., \mathbf{x}_n$ are found in the phase 2. For a statistically homogeneous and isotropic medium, the one-point correlation function $\mathcal{S}_1$ is constant everywhere and equal to the pore volume fraction [135]. The two-point correlation function (also known as autocorrelation) depends only on the relative distance between the two points. It can be obtained by randomly tossing a segment of length r into the

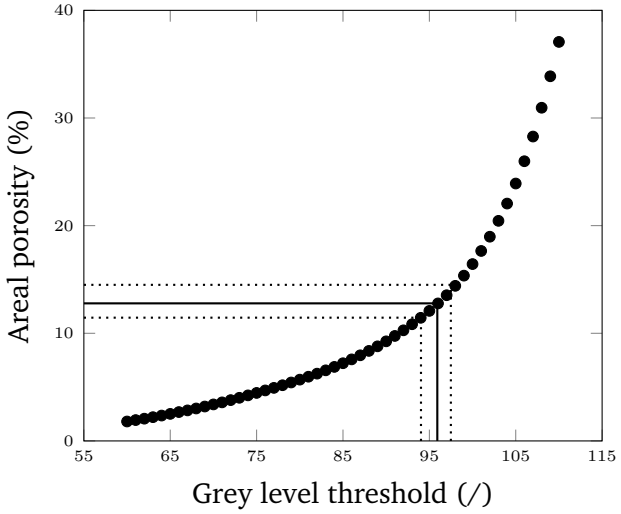

Figure 2.6.: Example of the error induced in the porosity measurement due to variation of the grey level threshold.

material and provides information of how the two end points in phase 2 are correlated [135]. Both functions can be measured from photographs of the cross sections of the material [130, 131], emphasizing specific features of the microstructure. Fig. 2.7 shows two examples of two-point correlation functions for isotropic particle systems of penetrable and impenetrable disks [135], which will be used in Chapter 4. When the disks are fully-penetrable, the two-point correlation function $\mathcal{S}_2(r)$ is characterised by an exponential decay and a constant value at large distance (Fig. 2.7a). Whereas, when the particles are impenetrable, the two-point correlation function $\mathcal{S}_2(r)$ shows oscillations that reflects the presence of excluded volumes among the particles and eventual interactions (Fig. 2.7b).

Pore size distribution

For a system composed of a solid matrix and spherical pores, the pore diameter probability density function $\mathcal{P}(D)$ (generally referred to as pore size distribution function) is the probability that the pore has a diameter between D and $D + dD$. The pores in the images can be categorised according to different measurement of pore/particle size [137]. The pores in the HBS are generally considered spherical [38, 41, 70]. Therefore, the pore section size distribution in 2D was determined by calculating for each pore section the equivalent-area diameter, which is the diameter of a 2D disk with the same projected area as the pore [138].
According to Shannon's sampling theorem, the smallest measurable detail in the image should be at least twice the spatial resolution of the image [139]. Since oversampling is recommended, a general resolution limit was chosen equal to ≈0.4 μm (which corresponds to an area of ≈0.16 μm^2) for the images at 500x and ≈0.13 μm (≈0.017 μm^2)

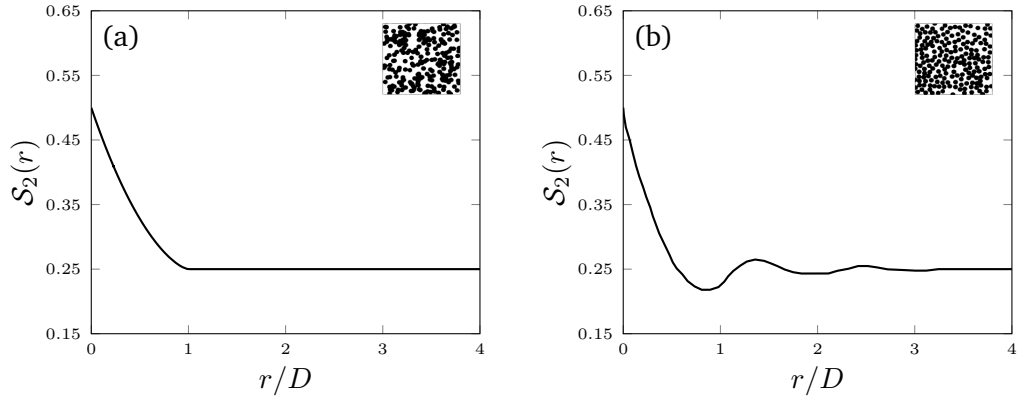

Figure 2.7.: The two-point correlation function $\mathcal{S}_2$ for phase 2 for a system of (a) overlapping disks, and (b) non-overlapping disks. In both figures the radial distance r is normalised to the disk diameter D [135].

for the others. All the measured pores smaller than those resolution limits were discarded. Then the two distributions from the images at different magnifications were merged. The cut-off diameter was chosen in an interval where the two distributions are comparable, as shown in Fig. 2.8. All the pores from the distribution obtained at high magnification with a diameter above the cut-off threshold were removed. The same was done for the pores in the distribution from the low magnification image with a diameter below the cut-off threshold. Finally, the remaining data were merged.

Generally, the pore size distribution function measured from a two-dimensional cross-section of the material does not coincide with the three-dimensional pore size distribution function [135]. However, under certain conditions, stereological methods can be applied to derive the three-dimensional pore size distribution function from the measured distribution of pore radius on a polished cross-section [140], as explained in the Section 2.4.3.

Pore shape factors

Even if in the HBS most of the pores are expected to be spherical [70], it is useful to evaluate possible variation in the expected behaviour within the analysed samples.
Image analysis allows to determine various pore shape factors [141] which provide a quantitative measurement of the pore shape. Among them, the ellipse ratio ER is defined as [142]

$$ER = \frac{x_{Lmax}}{x_{Lmin}} \tag{2.7}$$

where x_{Lmin} and x_{Lmax} are the minimum and maximum lengths of the axes of the ellipse with equivalent area to the considered pore. The descriptor has values between 1 and ∞. An ideal spherical pore has an ellipse ratio of 1, whereas the more the pore is elongated, the bigger the ER value.

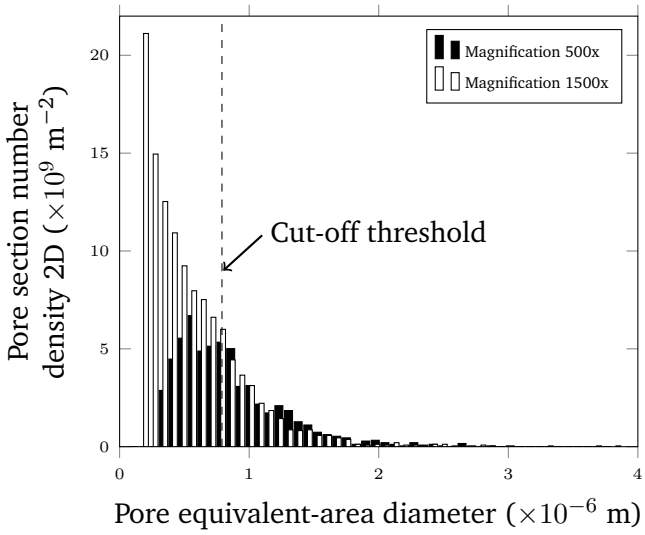

Figure 2.8.: Histogram showing the number of measured pores per unit area from high-magnification (1500x) and low-magnification (500x) images on the 67 GWd/tHM fuel cross-section at relative radial position $r/r_0 = 0.95$. The local burnup, calculated with the TRANSURANUS fuel performance code, is 82 GWd/tHM. The measured local porosity is 5%. The dashed vertical line shows the cut-off threshold. Total surface analysed: 24 000 μm^2 [123].

2.4.3. Stereological method to determine the three-dimensional pore size distribution in high burnup fuels

Stereology is used for obtaining three-dimensional (3D) quantitative information about the material microstructure, starting from two-dimensional (2D) measurements made on a material cross section [143]. It has been widely applied to derive 3D particle size distribution starting from a measurement of 2D contours in the plane section [140]. A review of all the available methods can be found in [144, 145]. Appendix A describes the Schwartz-Saltykov method, which is commonly employed to determine secondary-phase size distributions starting from a distribution of two-dimensional diameters [144]. Despite the fact that stereology does not provide topological information about possible pore interconnection, it allows to determine 3D pore characteristics from 2D data in a non-destructive way. Conversely, elaborate 3D reconstructions techniques involve time-consuming, stepwise polishing of sample surface and have limited applicability [70].

To my knowledge, Spino and co-workers [38, 41] were the only ones that applied stereology to estimate the 3D pore distribution and total pore density in LWR fuels at different burnups. They applied the Johnson-Saltykov [140, 144] method, which determines the 3D pore size distribution from the measured 2D section areas, under the assumption that the pores are log-normally distributed [146].

Assuming a log-normal distribution of the pores appears reasonable [147]; however, no direct proof has been given so far about the applicability of such hypothesis to the

porosity in the HBS. In fact, the mechanisms involved in the formation of the HBS and its porosity have not yet been completely clarified [22]. Moreover, in [41] the appearance of bi-modal and tri-modal distributions in the ultra-high HBS is claimed, in contradiction to the assumption of the method, i.e., log-normality of the pore distribution. Therefore, I have introduced a non-parametric approach to estimate the pore size distribution in the nuclear fuels, based on the adaptive kernel estimator (see Appendix B) [148–150].

Before introducing the new approach, I firstly revise the non-parametric methodology traditionally employed to estimate the 3D pore size distribution.
To obtain the 3D pore size distribution, traditionally histogram representation is used [140, 151]. The data are divided in N classes, containing $N_a(j)$ counts per area in each j class (m^{-2} per class, $j = 1...N$) and the selected unfolding procedure is applied [144] to obtain $N_v(j)$ counts per volume in each class j (m^{-3} per class). A scheme of the approach is depicted in Fig. 2.9, with particular reference to the Schwartz-Saltykov method (Appendix A). From the sum of the counts in each class also the total pore density (m^{-3}) can be obtained, by summing the counts in the various classes.

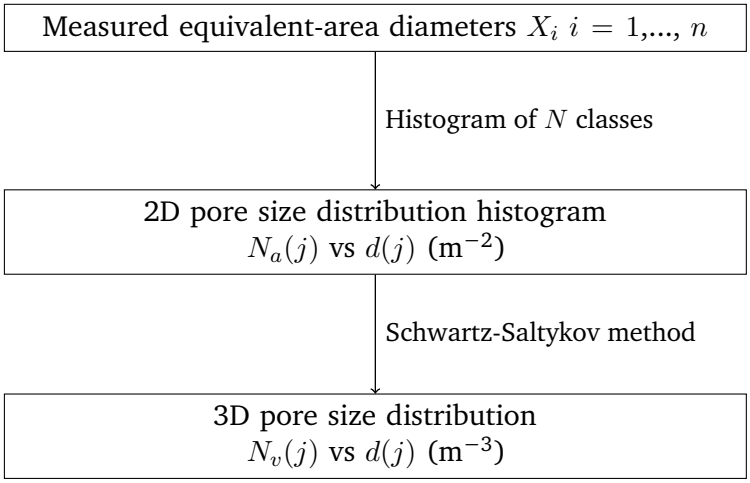

Figure 2.9.: Scheme of the approach used to determine the 3D pore size distribution based on the histogram and the Schwartz-Saltykov method [123].

In their study, Takahashi and Suito [152] evaluated the accuracy of the estimated total pore density obtained by the Schwartz-Saltykov method simulating the results of microscope observations on a test plane. The resolution limit and the number of classes N used in the histogram (or, alternatively, the bin width, which is inversely proportional to the number of classes N) were a source of bias in the estimation of the total pore density [152]. The effect of the resolution limit can be intuitively understood: it causes oversight of small sections, thus it determines an underestimation of the total particle density and an overestimation of the mean pore diameter [153]. Takahashi and Suito [152] analysed how the number of classes may determine a particle density underestimation. They showed that magnitude decreases upon increasing the number of classes. It is therefore advisable to increase the number of classes to minimise the

negative bias in the estimation. However, one of the main drawback of increasing the number of classes to construct the histogram is the appearance of oscillations in the class counts (see Fig. 2.10a). Such oscillations are due both to the limited number of observations and to the spatial discretization of the image acquisition system.

When applying the Schwartz-Saltykov method to derive the 3D distribution, some classes may present non-physical negative counts (see Fig. 2.10b). They are a consequence of the successive subtractions in Eq. (A.3). The negative counts appear in two different regions: below the resolution limit and above the resolution limit. On one hand, the negative counts below the resolution represent a limitation of the experimental approach and cannot be fully eliminated. I tried to reduce the occurrence of such counts by using high magnification pictures. However, a compromise between accuracy and the time involved in the analysis of the pictures had to be found. A resolution limit of $\approx$0.13 μm was considered satisfactory and the negative counts appearing below the resolution limit are simply neglected and set to zero.

On the other hand, the negative counts above the resolution limit are related to poor statistics, since only limited amount of data can be measured with the microscope in reasonable time. To overcome this second problem, I introduced a smoothing technique to estimate the 2D pore-size distribution. This second approach is depicted in Fig. 2.11. If an a-priori functional form for the pore size distribution could be assumed, the 2D data can be fitted with the appropriate distribution (e.g., a log-normal distribution) as reported in Fig. 2.11.

In both cases, i.e. either using a non-parametric approach based on the adaptive kernel estimator or using a log-normal fit of the data, once the probability density function of the pore size has been calculated, it is converted into a distribution of pores per area (m^{-2}). The distribution is approximated to a histogram with very fine bin width (i.e., high number of classes) and the Schwartz-Saltykov method is applied to unfold the 3D distribution using the generalised table of coefficients reported in [152] (see Appendix A for details). The advantage is to start from a smooth histogram so that the number of classes can be increased avoiding the oscillations and the negative counts above the resolution limit (see Fig. 2.10b). Only the negative counts below the resolution limit cannot be eliminated, as they are related to the experimental conditions (i.e., oversight of small sections). Increasing the magnification to avoid oversight of small pores would not be a complete solution since, in principle, the true distribution of pore size could extend to the atomic scale. In any case, the relevance of such small pores in terms of contribution to total void volume is limited[1] [147]. The resulting distribution in 3D is much more detailed and the bias in the estimation of the total pore density, calculated by summing up the counts in the various classes, can be decreased. For instance, Figure 2.12 shows how the estimated total pore density increases by increasing the number of classes used (i.e., decreasing the bin width) when starting from the log-normal fitting of the data, as demonstrated in [152]. The difference in the estimation can be up to 50%.

[1] However, the neglected small pores might be relevant for development of bubble nucleation models in the HBS.

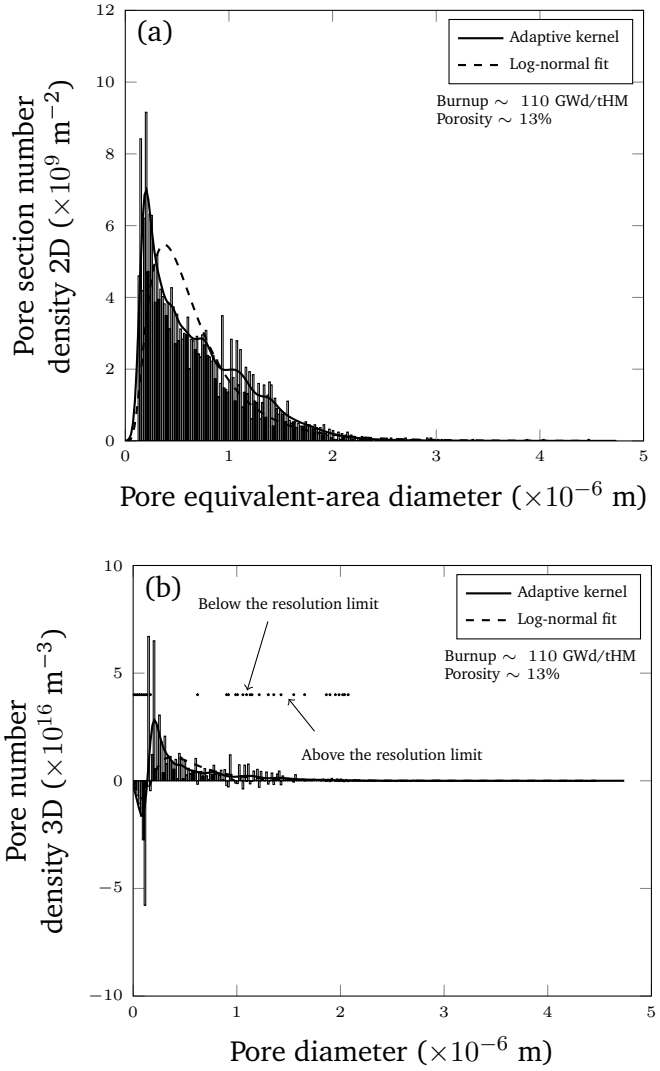

Figure 2.10.: Example of application of the porosity analysis methods. (a) 2D pore size distribution in the peripheral region of high burnup fuel (local burnup 110 GWd/tHM) determined with the histogram (256 classes), the adaptive kernel estimator and a log-normal fit of the data. (b) Estimated 3D pore size distribution using the Schwartz-Saltykov method from distributions in Fig. 2.10a. The stars indicate the size classes with negative values that are generated by the use of the histogram. Using the other two approaches, negative counts appear only below the resolution limit. Total surface analysed: 24 000 μm^2 [123].

The consistency of the estimation can be checked by comparing the estimated volume porosity to the measured areal porosity. Since the Schwartz-Saltykov method supposes

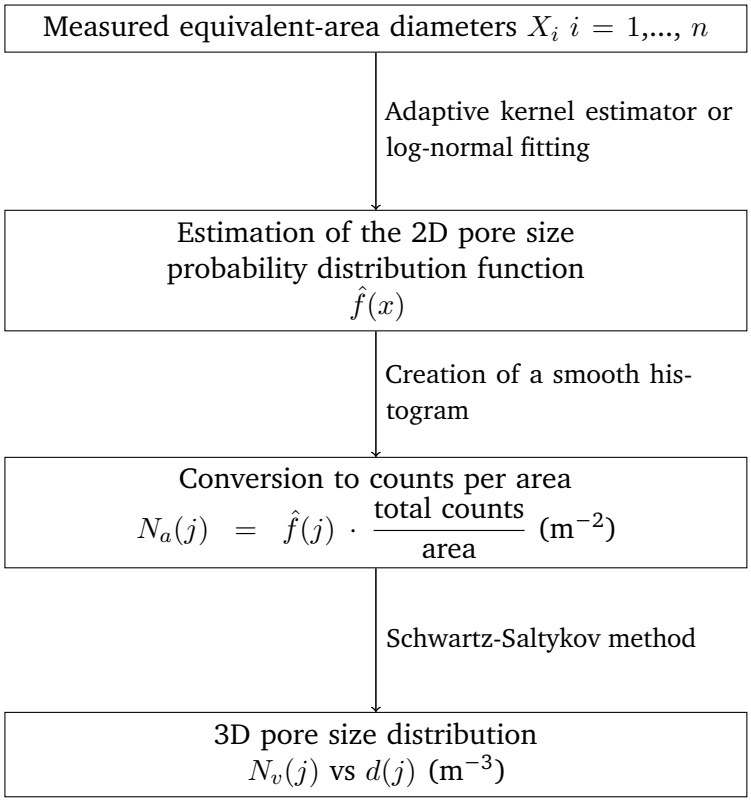

Figure 2.11.: Scheme of the approach used in this work to determine the 3D pore size distribution based on the smoothing technique and the Schwartz-Saltykov method [123].

that the pores are randomly dispersed, the estimated volume porosity has to be equal to the areal porosity measured by image analysis [38, 41, 143]. The volume porosity is calculated as follows,

$$P_{3D} = \frac{\pi}{6} \sum_{i=1}^{N} N_v(i) d(i)^3 \tag{2.8}$$

where $N_v(i)$ are the counts per volume and $d(i)$ the mean pore diameter in the i-th class. A comparison between the estimated total pore density obtained using the histogram (approach in Fig. 2.9) and the adaptive kernel estimator (approach in Fig. 2.11) is shown in Figs. 2.13a and 2.14a for two representative cases. Only the positive counts in the classes are accounted for. If negative counts appear even above the resolution limit, those counts are crudely set to zero. The comparison between the estimated volume porosity and the measured areal porosity is shown in Figs. 2.13b and 2.14b. In Figs. 2.13b and 2.14b the estimated volume porosity is normalised to the measured areal porosity. Using the histogram, the total pore density extrapolated to zero bin width [152] would

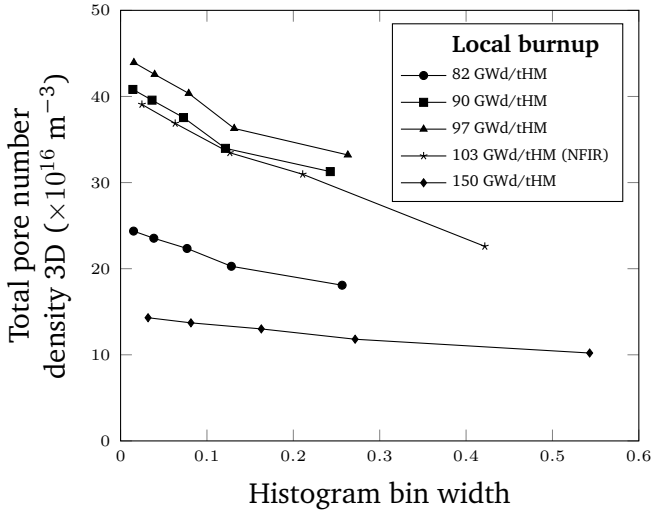

Figure 2.12.: Examples of the influence of the bin width on the estimated total pore density. The estimation is done starting from a log-normal fitting of the measured pore equivalent-area diameter in 2D [123].

result in an inconsistent estimation, because the equality between volume and areal porosity is violated (Figs. 2.13b and 2.14b). In order to have an estimation congruent with the results obtained using the adaptive kernel the number of classes must be reduced (Figs. 2.13 and 2.14). This requires an operator-dependent choice of the number of classes, which might be not optimal. Instead, the choice of the smoothing parameter of the adaptive kernel is automatic and optimised on the data (see Appendix B). The use of the adaptive kernel estimator has the advantage to limit the influence of the operator, while keeping a high level of detail in the description of the pore size distribution.

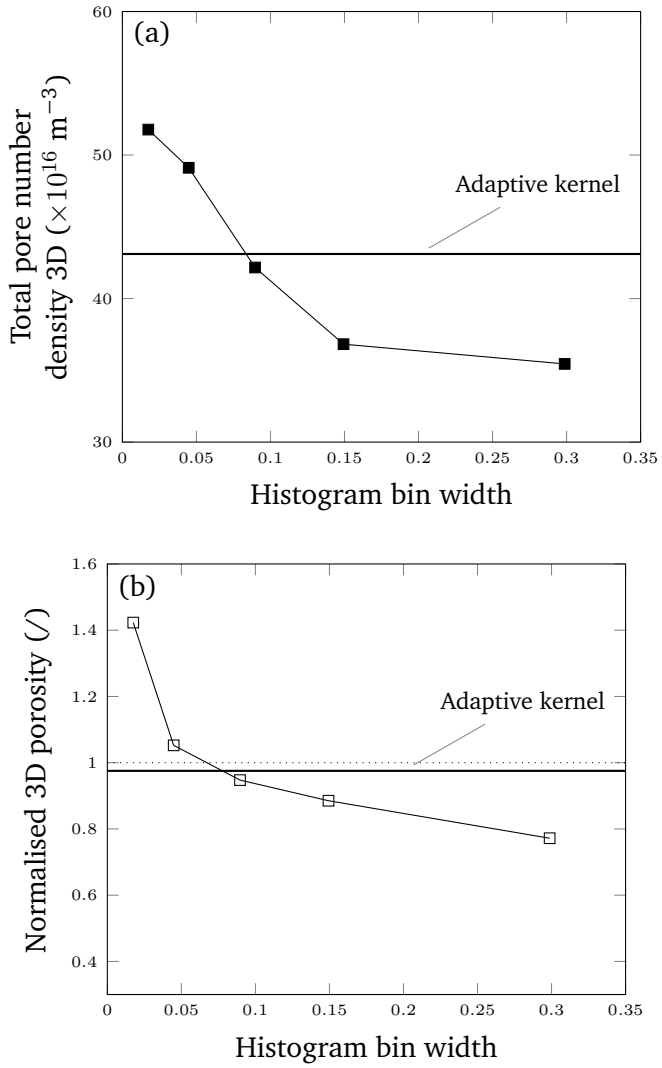

Figure 2.13.: (a) Estimated total pore density as a function of the histogram bin width obtained applying the method in Fig. 2.9 to a sample with a local burnup of 110 GWd/tHM (histogram reported in Fig. 2.10b). The negative values that appear in some of the histogram classes are set equal to zero. The estimated total pore density obtained by applying the adaptive kernel estimator is shown (solid line). (b) Verification of the consistency of the 3D estimation in Fig. 2.13a by comparing the estimated volume porosity to the areal porosity. The volume porosity is normalised to the measured areal porosity. Values above 1 (dotted line) indicate overestimation and below 1 indicate underestimation. The corresponding verification for the adaptive kernel is indicated by the solid line [123].

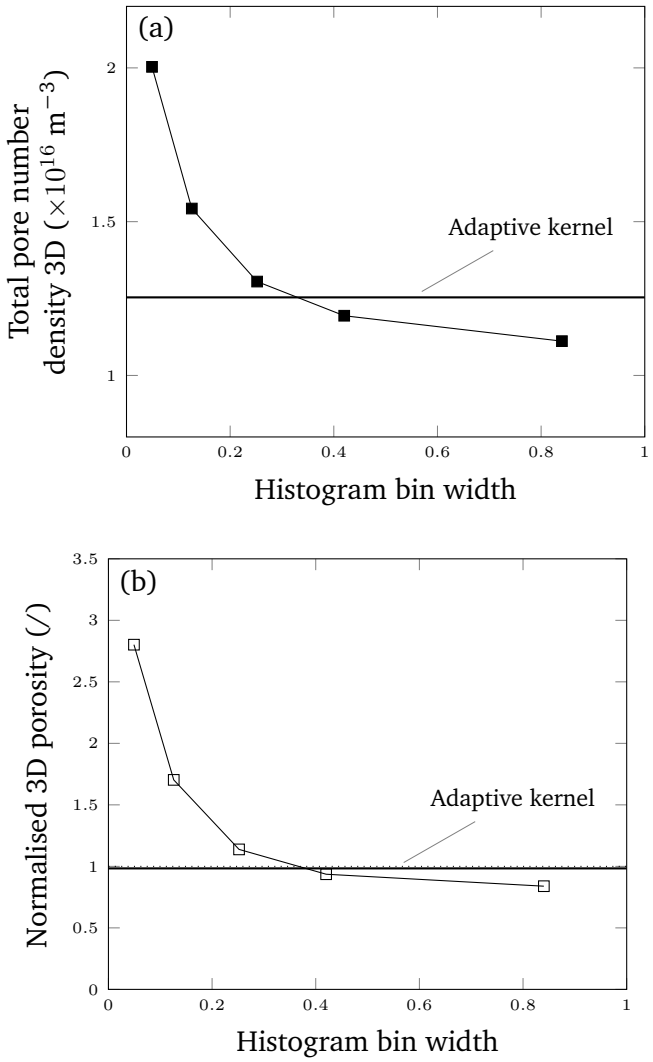

Figure 2.14.: (a) Estimated total pore density as a function of the histogram bin width obtained applying the method in Fig. 2.9 to a sample with a local burnup of 203 GWd/tHM. The negative values that appear in some of the histogram classes are set equal to zero. The estimated total pore density obtained by applying the adaptive kernel estimator is shown (solid line). (b) Verification of the consistency of the 3D estimation in Fig. 2.14a by comparing the estimated volume porosity to the areal porosity. The volume porosity is normalised to the measured areal porosity. Values above 1 (dotted line) indicate overestimation and below 1 indicate underestimation. The corresponding verification for the adaptive kernel is indicated by the solid line [123].

3. Experimental results

> However beautiful the strategy, you should occasionally look at the results
>
> *Winston Churchill*

Abstract *Here the experimental results are presented and discussed. The chapter is divided into two main parts. The first describes the fuel mechanical properties and their relationship with the local microstructure and porosity, while the second focuses on the characterisation of the samples grain structure and porosity along the pellets radius.*

In the context of the safety studies on the back-end of the high burnup fuel cycle, indentation tests are carried out on fuels previously investigated after additional 15-20 years of storage in the hot cells to assess possible ageing effects due to accumulation of microstructural decay damage. No significant hardening is observed. The microhardness values vs. the accumulated alpha-damage seem to saturate at a dpa level ≈ 0.1*, similar to what observed for the* ^{238}*Pu-doped samples. These results are a first comparison between* ^{238}*Pu-doped analogues and spent fuel, paving the way for validation of alpha-doped analogues as predictors of the spent fuel long-term properties evolution during storage.*

New data concerning the high burnup fuel microhardness and Young's modulus are obtained. The relationship between the two properties was found constant over a large range of burnups and porosity, suggesting that the microhardness could be used as a probe of the Young's modulus in the HBS, where direct measurements are difficult. Based on the new data, the correlation for the Young's modulus of irradiated UO_2 *fuel used in the fuel performance code TRANSURANUS was updated, including the effect of burnup.*

In addition to the investigations on the samples rim, complete radial analyses of the porosity and grain morphology evolution has been performed for selected samples with average burnup in the range of the "pulverisation threshold" (i.e. 60-80 GWd/tHM) during LOCA-type transients. The scope of these investigations was to provide a set of data in order to support further development and refinements of dedicated models.

Finally, the analysis of the pore density and pore mean diameter as a function of the local burnup in the rim region of the samples has been performed. Starting at $\approx$*100 GWd/tHM, the pore number density decreases and the mean pore diameter increases, suggesting that pore coalescence occurs.*

3.1. High burnup fuel mechanical properties

In this section, the experimental results illustrating the measured mechanical properties of fuel at high burnup are reported. Part of the results here presented have been published in [154, 155].

3.1.1. Ageing studies of spent fuel microhardness

The microstructural damage experienced by the fuel continues after discharge from the reactor. During storage, the radioactive decay of the various radionuclides still causes damage in the fuel matrix; in the long term, this is mainly due to the α-emitters. Although in-pile fission damage is much more severe, the decay damage extends for time scales up to millennia. Moreover, such damage occurs at relatively low temperatures, which do not allow thermal recovery of the defects.

When performing post-irradiation examinations, it is generally not possible to separate the effects due to in-pile damage and out-of-pile damage. However, samples from two rods that were already analysed in the past by Spino and co-workers [81, 156] are still available in JRC-Karlsruhe hot cells. I measured them again to assess possible ageing effects on the microhardness which were caused by further α-damage accumulated during the additional storage period in the hot cells. Figs. 3.1 and 3.2 report the measured microhardness radial profiles for the two samples, which had an average burnup 80 GWd/tHM and 102 GWd/tHM, respectively.

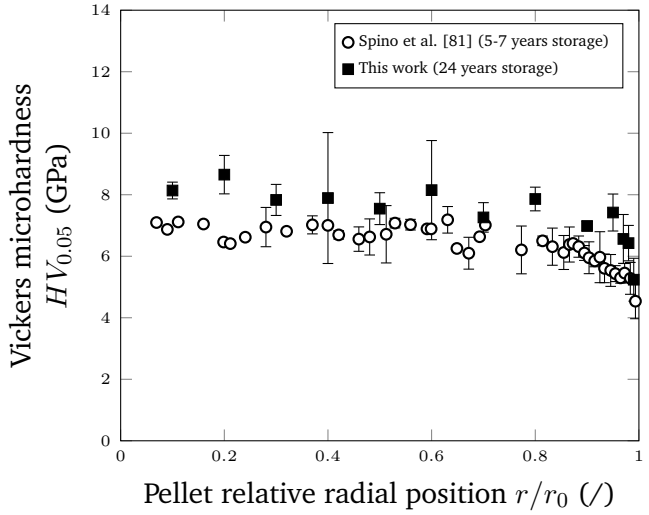

Figure 3.1.: Vickers microhardness radial profile for the sample with average burnup 80 GWd/tHM after 5-7 years of storage (circles) [81] and 24 years of storage (squares) in the hot cells. A slight hardening is indicated by the two curves.

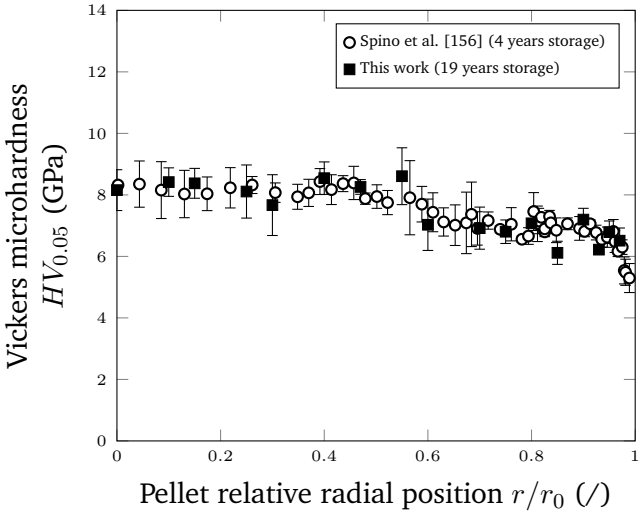

Figure 3.2.: Vickers microhardness radial profile for the sample with average burnup 102 GWd/tHM after 5-7 years of storage (circles) [156] and 19 years of storage (squares) in the hot cells. No additional hardening can be observed after additional >10 years of storage. The outermost part of the pellet ($r/r_0 > 0.98$) could not be measured in this work because the fuel decladded during handling.

For the sample at 80 GWd/tHM, minor hardening was distinguishable after additional ≈18 years of storage (Fig. 3.1). Instead, no hardening was observed for the sample at 102 GWd/tHM.

The average concentrations of the main α-emitters at End of Life (EOL) were calculated using the web-based KORIGEN code [98], on the basis of the fuel rod characteristics and irradiation history reported in [4, 157] and the fuel specifications in Table 2.1. The calculated concentrations are given in Tables E.1 and E.2 in Appendix E.

The cumulated damage dose at the different times when microhardness measurements were performed is expressed as displacements per atom (dpa), which is related to the number of atoms displaced from their original lattice site. The dpa dose was calculated assuming a constant conversion factor between the cumulative alpha-dose, expressed as α-decays per gram of uranium (α/g), and the number of atoms permanently displaced following a decay event. The conversion factor, according to Wiss et al. [94], is

$$\frac{\text{dose (dpa)}}{\text{dose } (\alpha/\text{g})} = 2.7778 \cdot 10^{-20} \tag{3.1}$$

The calculated average doses at the times of measurement for the two samples are reported in Tables 3.1 and 3.2.

The nuclear data library included in webKORIGEN is relatively old [158, 159]. Uncertainties in the calculated inventory lead to variability in the calculated dose. In order to

Table 3.1.: Cumulative α-dose for the PWR SNF sample with average burnup 80 GWd/tHM at different times from discharge based on the inventory calculations of two codes.

Time from discharge (y)	webKORIGEN Cumulated dose (dpa)	SERPENT Cumulated dose (dpa)	Difference[a] (%)
6	$1.54 \cdot 10^{-2}$	$1.94 \cdot 10^{-2}$	-20.79
24	$4.55 \cdot 10^{-2}$	$5.61 \cdot 10^{-2}$	-18.83

[a] Relative error in the calculated dpa using the inventory calculated with webKORIGEN and the one calculated with SERPENT, taken as reference.

Table 3.2.: Cumulative α-dose for the PWR SNF sample with average burnup 102 GWd/tHM at different times from discharge based on the inventory calculations of two codes.

Time from discharge (y)	webKORIGEN Cumulated dose (dpa)	SERPENT Cumulated dose (dpa)	Difference[a] (%)
4	$1.84 \cdot 10^{-2}$	$1.70 \cdot 10^{-2}$	+8.68
19	$6.38 \cdot 10^{-2}$	$5.66 \cdot 10^{-2}$	+12.77

[a] Relative error in the calculated dpa using the inventory calculated with webKORIGEN and the one calculated with SERPENT, taken as reference.

give a qualitative estimation of the uncertainty, the results were benchmarked against inventory calculations [160] obtained with the SERPENT code [161], which is based on the more modern JEFF-3.1.1 library [162]. The differences in the calculated nuclide initial inventory are not systematic (see Tables E.1 and E.2), which are reflected in the dose differences (Tables 3.1 and 3.2). In the case of the sample at 80 GWd/tHM, the difference in the calculated dose is approximately -20% (Table 3.1), whereas for the other sample there is a positive difference of $\approx$13% (Table 3.2). It has to be noted that the burnup of the two rods is considerably higher compared to the burnup range usually encountered in commercial fuel rods and covered by the inventory codes. Therefore, the calculated inventory will be invariably approximative, being the actinide inventory affected by relatively large uncertainty [162]. On the basis of the first comparisons reported here, I considered a mean value between the two calculated doses and I assigned a conservative error of $\pm$ 30 %.

The actinides are not uniformly distributed along the fuel cross section, rather their concentration increases towards the pellet rim (Fig. 3.3). In order to evaluate a potential enhanced hardening of the pellet rim during the additional years of storage, the maximum local α-dose was calculated according to the radial profiles of the α-emitters concentrations obtained with SERPENT [160], resulting in a local value of 0.103 dpa for

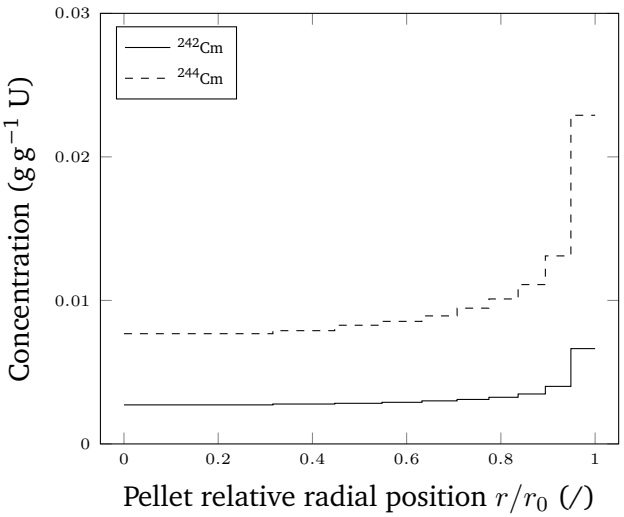

Figure 3.3.: Radial profile of ^{242}Cm,^{244}Cm concentrations.

the sample with 80 GWd/tHM, and 0.108 dpa for the other for relative radial positions $r/r_0 > 0.95$. No benchmark with the webKORIGEN code could be performed in this case, since only an average concentration can be calculated with this code.

The microhardness values measured on SNF have to be corrected for porosity before comparing them to the values from ^{238}Pu-doped samples, which do not exhibit appreciable porosity. First, the relationship between the local microhardness and the local porosity measured via image analysis (Section 2.4) in the fuel samples has to be established. The results are reported in Fig. 3.4. In view of the big scatter of the data, it is not straightforward to establish a trend between the microhardness and the porosity. To my knowledge, there is a limited amount of models that study the dependence of microhardness on porosity in ceramics [108, 109, 163]. Spino et al. [82] used an exponential relationship to fit Vickers microhardness data of high burnup UO_2, on the basis of the minimum solid area approach [164, 165]. In the relatively small range of porosity measured here and considering the experimental scatter, also a linear fit can be employed (Fig. 3.4). In the two cases, the goodness of fit values, estimated on the basis of the adjusted R^2, are very similar and equal to 0.71 for the linear fit and 0.73 for the exponential fit.

The microhardness results corrected for the porosity according to the linear relationship in Fig. 3.4 are shown as a function of the cumulative α-dose in Fig. 3.5. The microhardness and porosity error are propagated assuming that the error of the two measurements are uncorrelated. An average of the microhardness and porosity radial profiles in Figs. 3.1 and 3.2 away from the pellet periphery ($r/r_0 < 0.80$) was considered as a function of the average dpa. Also the results of the samples rim with the maximum accumulated dose are shown in Fig. 3.5. In the figure, also the evolution of the microhardness in the ^{238}Pu-doped samples is reported, showing progressive hardening upon accumulation of the α-decay damage [94].

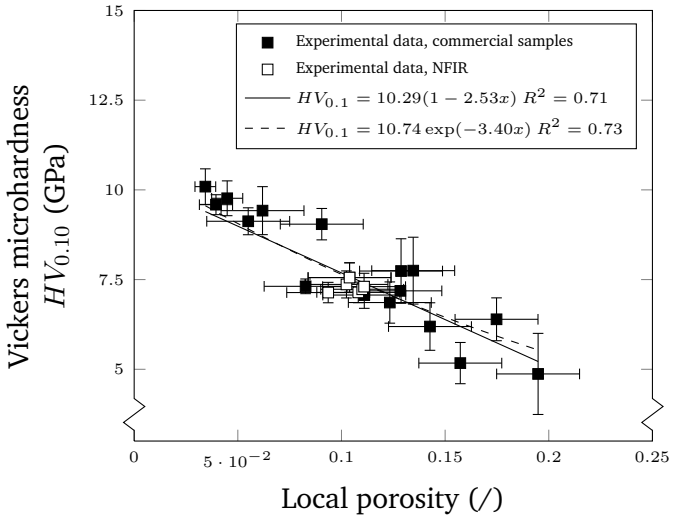

Figure 3.4.: Measured Vickers microhardness as a function of the local porosity. The error bars of the microhardness represent 95% confidence level. The error bars of the porosity represent the error in the porosity induced by the variation of the mask threshold (see Section 2.4.1) [154].

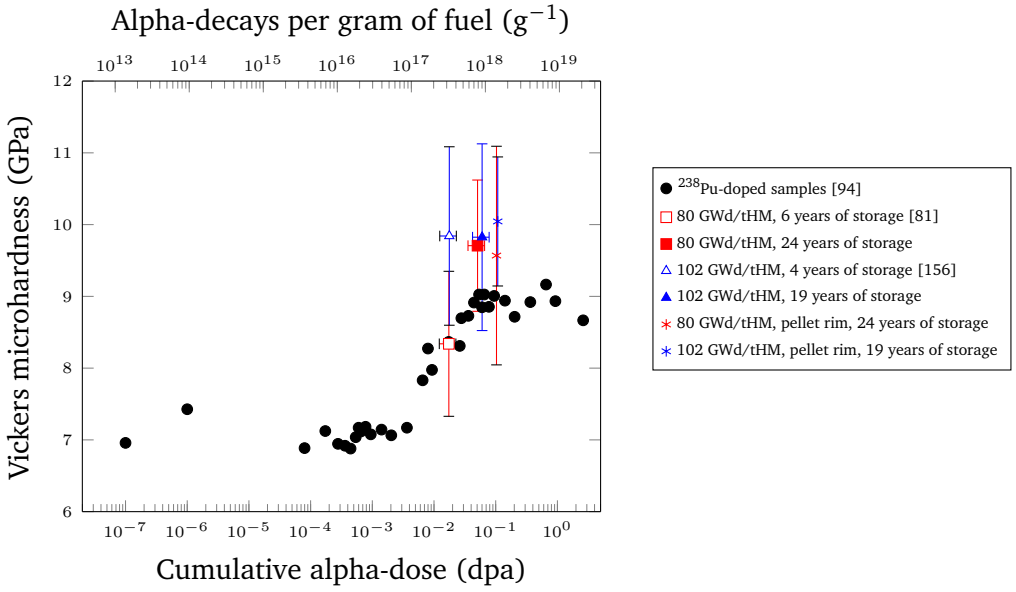

Figure 3.5.: Vickers microhardness as a function of the cumulative alpha-dose for SNF and ^{238}Pu-doped analogues [94].

It is possible to interpret the different hardening behaviour observed when re-measuring the Vickers microhardness in the two samples on the basis of Fig. 3.5. The additional small hardening shown by the 80 GWd/tHM fuel could be related to the fact that at the time when the first measurements were performed the fuel cumulative damage had not yet reached the saturation level. Viceversa, the 102 GWd/tHM fuel had essentially reached hardness saturation already at the time of the first measurement campaign. Within the limited dpa ranges corresponding to the damage that has been accumulated by the available SNF samples, and in spite of the experimental scatter, the present results contribute to show that the fuel microhardness saturates around 10 GPa, even in rim region which has accumulated more damage at a higher rate. The dose at which the saturation is reached is around 0.1 dpa, similar to the ^{238}Pu-doped samples. Further investigation is necessary to confirm and extend the present observation to other damage levels.

The SNF samples generally show a higher absolute value of microhardness compared to the ^{238}Pu-doped samples. Partially, the difference could be due to the fact that the ^{238}Pu-doped samples were tested using a 0.1 N load, whereas the measurements on the SNF were performed using a 0.05 N load, resulting in a slightly higher absolute value of the microhardness in the second case, being the microhardness load-dependent [124]. In addition, the difference could be due to fission damage not present in the ^{238}Pu-doped samples. Further increase of the microhardness as a consequence of chemical hardening effects due to the dissolved and/or precipitated fission products is also possible, as was demonstrated by Spino and co-workers on SIMFUEL (see Fig. 6 in [82]).

3.1.2. Comparison with fuel performance codes correlations

The microhardness data is not directly input in fuel performance codes, whereas the fuel Young's modulus is employed. The fuel Young's modulus relationship with local porosity is of particular interest, since the porosity has a strong impact on the elastic constants. As anticipated in the introduction, the correlations of the fuel Young's modulus with porosity implemented in the codes generally rely on data from non-irradiated UO_2 [166–168]. These correlations are linear relationships whose slope reflects the geometry of the lenticular pores in sintered solids [120]. As the porosity in the HBS is mainly composed of spherical cavities [38], direct application of such relationships to the HBS may be questionable.

Direct measurements of Young's modulus at the pellet rim, where the increase of porosity is the highest, are hindered by limitations in the currently available experimental set-up of the SAM. The HBS thickness is generally less than the current acoustic microscope spatial resolution. In addition, the cladding-fuel interface causes sidewalls reflections that could interfere with the incident signal.

I tackled the aforementioned experimental limitations by combining the results of Vickers microindentation and the available Young's modulus experimental data. A first investigation of the radial profiles of the two mechanical properties obtained on one commercial

sample irradiated at 67 GWd/tHM suggested a possible correlation between the local values of the two (Fig. 3.6).

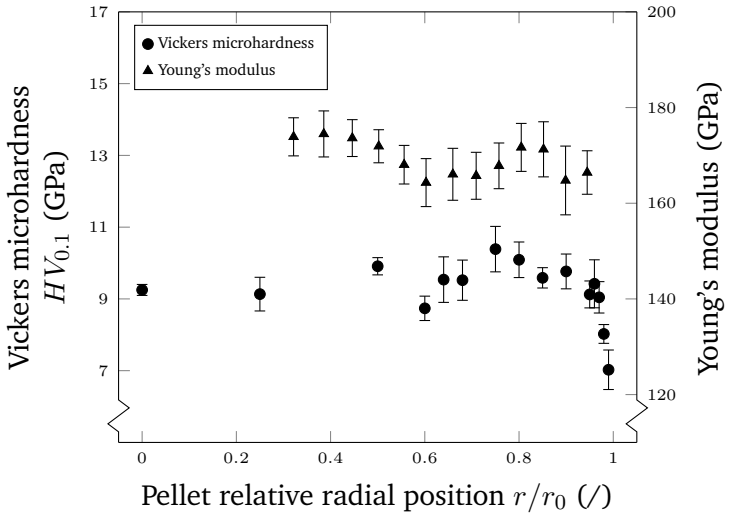

Figure 3.6.: Variation of the fuel microhardness radial profile compared to the corresponding Young's modulus radial profile. Sample average burnup: 67 GWd/tHM.

Extensive studies have been performed about the theoretical relationship between hardness and Young's modulus [169–172]. The models have been developed for instrumented indentation techniques and would have limited applicability to static indentation tests as the ones here performed. Firstly, in this work only the residual projected area of the hardness impression after load removal is measured, which might be different from the projected contact area during load application used in the instrumented indentation [173]. Secondly, no model specifically considers crack formation during the indentation tests, which were observed in some of the measurements (see Fig. 3.7). Therefore, I determined the relationship between the measured microhardness and the Young's modulus only empirically. The ratios between the measurements obtained from the Vickers microindentation tests and the acoustic microscopy at different values of local burnup were calculated and are reported in Fig. 3.8. A constant value of the ratio microhardness/elastic modulus ($HV_{0.1}/E$) was obtained, with a mean value 0.057. The values of Young's modulus measured on the irradiated fuel sample (ranging between 130 and 180 GPa, Figs. 3.6 and 3.10) are lower compared to the measured value for non-irradiated UO_2 (223$\pm$5 GPa [114, 117]). Both the porosity and the lattice distortions induced by fission products and radiation damage decrease the Rayleigh velocity [114], thus lowering the Young's modulus. On the other hand, the microhardness increases in irradiated fuel [41, 82, 110, 111] compared to non-irradiated UO_2 [110], due to accumulation of radiation damage [110, 111] and fission products [82]. For instance, Bates et al. [110] reported a Knoop hardness between 7.61 GPa and 7.98 GPa for polycrystalline UO_2 with 97% TD using a 0.1 kg load. In the irradiated samples here analysed, where

the measured porosity is around 3%-4% the Vickers microhardness measured at the same load was in the range 9 GPa–10 GPa (see Fig. 3.4). As a result, the determined $HV_{0.1}/E$ value is higher than values reported for non-irradiated UO_2 (0.0263-0.0304 [174] and 0.033 [175]) and for SIMFUEL (0.024 [176]) and in good agreement with values reported for irradiated fuel samples at different burnup [177].

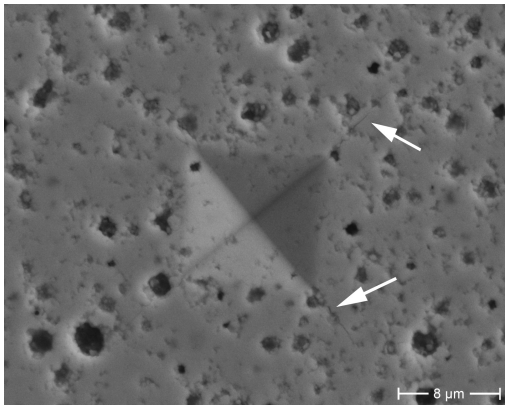

Figure 3.7.: Representative SEM-micrograph of fuel indentation imprint using 0.98 N load. White arrows point out the cracks sometimes observed at the imprint tips.

The ratio $HV_{0.1}/E$ is constant over a large range of burnups (60-112 GWd/tHM) and, hence, pore volume fractions (0.04-0.13), including also ranges where the HBS has formed (data points above 80 GWd/tHM in Fig. 3.8). On the basis of this finding and assuming that, as a first approximation, the porosity dependence of hardness should reflect that of the elastic moduli [82, 108, 109], I could use the measured microhardness as local probe for the variation of Young's modulus with local porosity in the HBS.

The correlations obtained in Fig. 3.4 were compared to the relationships available in literature and implemented in various fuel performance codes [117, 119, 166, 178–184]. The Young's modulus of stoichiometric UO_2 is generally expressed as follows [166, 167, 179]

$$E = E_0 \; f(p) \; g(T) \tag{3.2}$$

where E_0 (GPa) is the Young's modulus of the fully dense, non-irradiated UO_2 at room temperature, p (/) is the fractional porosity, T (°C) the temperature. Table 3.3 reports the values of several correlations available.

The experimental measurements performed in this study were conducted at room temperature. Therefore, the focus of the analysis was only on the relationship with porosity. Comparing the porosity correlations in Table 3.3 to the calculated linear relationship plotted in Fig. 3.4, no major differences are identifiable in the Young's modulus dependence on porosity between irradiated and non-irradiated UO_2. When taking into account the experimental uncertainties, the present set of data would not justify the introduction of a

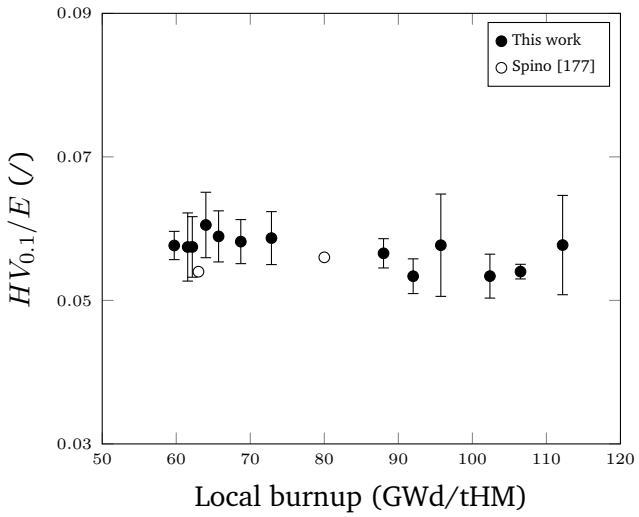

Figure 3.8.: Measured Vickers microhardness to Young's modulus ratio $HV_{0.1}/E$ as a function of the local burnup [154]. The results of the present work (black circles) are in good agreement with previous results by Spino (white circles) [177].

Table 3.3.: Correlations of stoichiometric UO_2 Young's modulus available in literature.

E_0	$f(p)$	$g(T)$	Ref.
223.7	$1 - 2.6\ p$	$1 - 1.394 \cdot 10^{-4}(T - 20)$	[166]
226	$1 - 2.62\ p$	$1 - 1.131 \cdot 10^{-4}\ T$	[167]
226.4	$1 - 2.752\ p$	$1 - 1.125 \cdot 10^{-4}\ T$	[168]
222.46	$1 - 2.5\ p$	$1 - 8.428 \cdot 10^{-5}\ T - 4.381 \cdot 10^{-8}\ T^2$	[117]
220	$1 - 2.34\ p$	not reported	[119]

different correlation to describe the decrease of Young's modulus with porosity in high burnup irradiated UO_2, in particular in the HBS. The present results do not confirm the findings in a previous work reported by Spino et al. [82], where the decreasing trend of Vickers microhardness in irradiated and non-irradiated fuel was found to be different. The reason of the different behaviour was explained in [82] in terms of pore shape. The pores in the HBS are spherical, whereas the intergranular pores outside the HBS have a more lenticular shape, thus contributing to a larger mechanical property decrease at a fixed value of porosity [82].

To evaluate the potential effect of the shape factor [141], a pore shape factor was calculated from the SEM images, namely the pore ellipse ratio defined in Eq. (2.7). The majority of pore shape factors measured at various porosity remains fairly close to one, indicating the good approximation of the pore shape to a sphere (see Fig. 3.9). However, coarsened cavities (i.e. with ellipse ratio > 2) are observed, with a frequency up to $\approx$5%

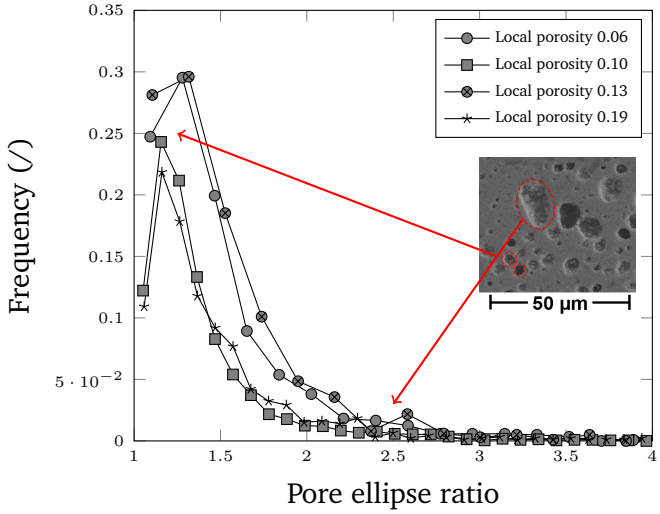

Figure 3.9.: Frequency distributions of the pore ellipse ratios for various level of local porosity. Pore ellipse ratios in the range 1-1.5 (corresponding to almost spherical pores) represent the majority of pore population. Coarsened pores (pore ellipse ratio >2) are also present (see inset in the Figure) [154].

(inset of Fig. 3.9). The pore-pore contact onset was also recognised for other similar samples [41, 43]. This may explain a deviation from the behaviour observed by Spino et al. [82]. A similar explanation was given in [185] to justify deviation in the trend of the mechanical properties vs. porosity in HBS-analogue material compared to what was found in [82] for irradiated fuel. Hence, on the basis of the present analysis, it is fair to conclude that the validity of the relationships $f(p)$ in Table 3.3 could be extended from non-irradiated to high burnup UO_2 fuel, including the HBS.

From the microhardness data as a function of local porosity (Fig. 3.4), the Young's modulus was calculated using the measured mean ratio $HV_{0.1}/E$ (Fig. 3.8). The calculated results are reported in Fig. 3.10 together with the available data from acoustic microscopy both from this work and from the HBRP results [114].

The correlation currently implemented in TRANSURANUS V1M1J14 [166] and the MATPRO correlation [168], both evaluated at room temperature, are also plotted in Fig. 3.10 (dashed and dotted line, respectively). They generally overpredict the value of the Young's modulus of irradiated UO_2 at each value of porosity. The same conclusion is valid for the other correlations in Table 3.3, which are not included in the figure for clarity. Within the range of porosity analysed, the difference between the correlations presently available in literature (see Table 3.3) and the trend of the measured data is between 5% and 15%. The discrepancy is attributed to a burnup accumulation effect, in agreement with a previous investigation [115, 118].

Therefore, a modified relationship for the Young's modulus has been introduced (black and grey solid line in Fig. 3.10). An additional factor that takes into account the "apparent

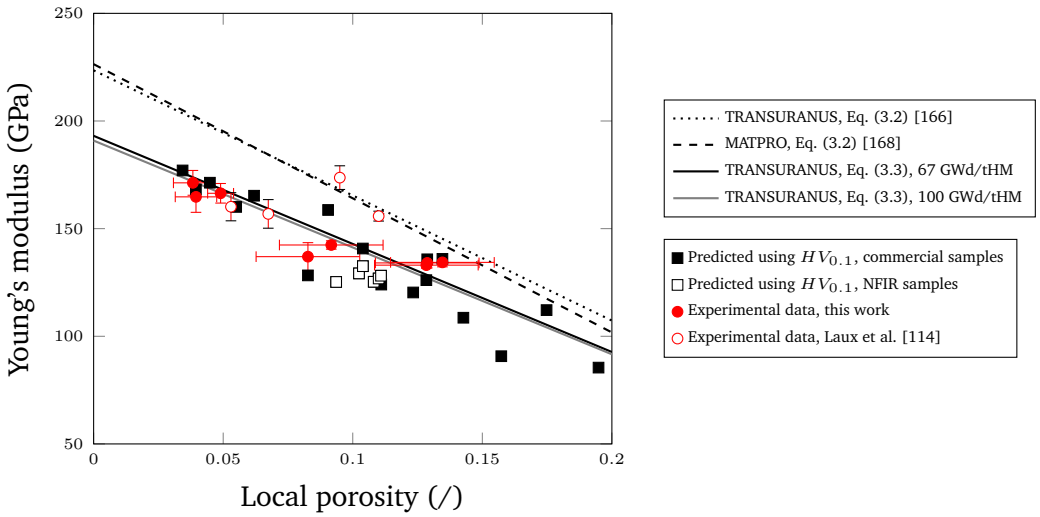

Figure 3.10.: Young's modulus as a function of local porosity and comparison to correlations used in fuel performance codes [154]. Black and white squares: values predicted using Vickers microhardness data and the measured ratio $HV_{0.1}/E$. Red circles: data from acoustic microscopy in this work. White circles: data from literature [114]. Dashed black line: TRANSURANUS V1M1J14 correlation currently available [166]. Dotted black line: MATPRO correlation [168]. Solid black and grey lines: TRANSURANUS correlation implemented in this work for two values of local burnup.

softening" due to burn-up was included, based on the experimental results reported by Laux et al. [114, 115]. The new expression of E (GPa) is then given by

$$E = E_0 \; f(p) \; g(T) \; h(bu) \tag{3.3}$$

where E_0, $f(p)$, and $g(T)$ have the same meaning as before and bu (GWd/tHM) is the local burn-up. The new factor introduced is

$$h(bu) = 1 - 0.1506 \; [1 - \exp(-0.035 \; bu)] \tag{3.4}$$

The new correlation of the Young's modulus (Eq. (3.3)) is in better agreement both with the experimental data and the predicted E using the microhardness measurements when compared to Eq. (3.2).

3.2. Characterisation of the samples microstructure

3.2.1. Porosity and grain structure along the pellet radius

During irradiation, the fuel pellet experiences radial temperature and burnup gradients, which cause a complex radial evolution of the microstructure. Moreover, variations in the power history also influence the microstructure final configuration. In high burnup fuels, the main microstructural changes are due to the HBS formation at the pellet rim, and to thermal fission gas precipitation in the central parts of the pellet. Figure 3.11 displays polished cross sections of two LWR UO_2 fuels irradiated at very high burnup analysed in this work. Concentric zones of different appearance (i.e., with different grey "shading" tones) are visible in the macrographs. On the polished surface, such radial differences in the grey shade are mainly due to difference in the bubble size and density. The analysis of this feature is relevant to assess safety and performance of LWR fuel. Turnbull et al. [79] have suggested that the high local concentration of bubbles renders the fuel susceptible to pulverization during LOCA. Given the potential strong influence of pores characteristics on the fission gas release kinetics in such type of accidents [75], it is of general interest to provide a more detailed quantification of the pore and grain characteristics across the entire pellet radius, information that is generally not fully available in literature for regions outside the rim area. Two samples with average burnup above or near the threshold for fine fragmentation were selected for detailed analysis, namely with 67 and 80 GWd/tHM (Fig. 3.11).

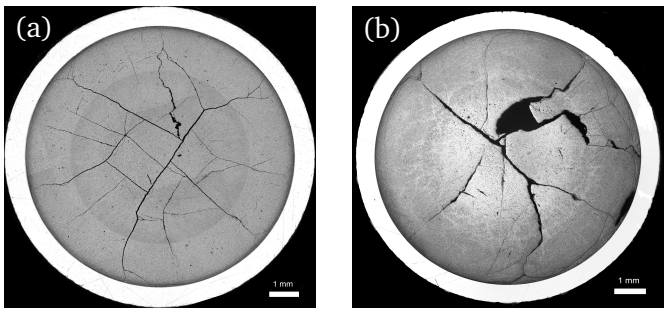

Figure 3.11.: Cross section of LWR UO_2 fuels with average pellet burnup (a) 67 GWd/tHM, (b) 80 GWd/tHM.

In the macrograph of the sample with average burnup 67 GWd/tHM (Fig. 3.11a), at the periphery of the pellet a very thin dark zone can be seen, corresponding to the HBS. At intermediate radial positions (i.e., $0.60 < r/r_0 < 0.65$) a second porous band is visible. This observation is similar to what reported by Stehle [186] and Walker et al. [35] on PWR fuels irradiated at 52 and 64 GWd/tHM average burnup, respectively. The increase in porosity in this zone corresponds to the so-called "dark zone" [72]. The increased porosity could be a consequence of enhanced precipitation of fission gas into grain boundary bubbles due to relatively high operating temperatures (generally between 900 °C and 1100 °C [72]). In the other sample, bubble precipitation has occurred more extensively

through more than half the fuel radius (Fig. 3.11b). The qualitative observations of the fuel macrographs are reflected in the porosity radial profiles of the two samples, reported in Figs. 3.12 and 3.13, respectively. The pore number density and mean pore diameter according to the methodology reported in Section 2.4 as a function of the pellet radius are shown in Figs. 3.14 and 3.16.

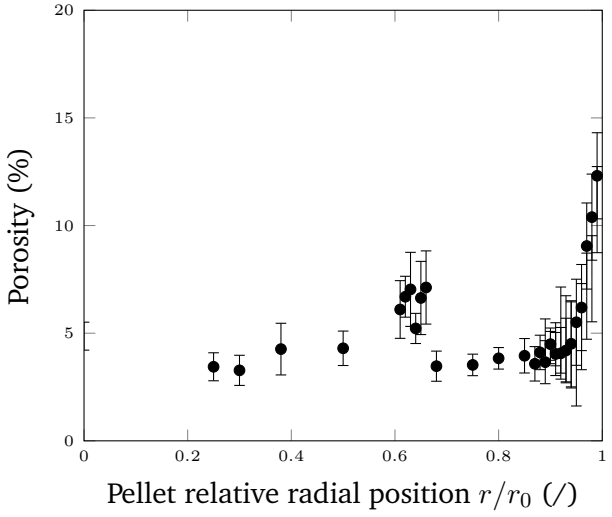

Figure 3.12.: Porosity radial profile for the sample with average burnup 67 GWd/tHM.

For the sample at 67 GWd/tHM, a clear increase in the total measured porosity in this intermediate zone is visible (Fig. 3.12). The porosity in the dark zone is characterised by a pore number density comparable to the values measured at the onset of the HBS (see Fig. 3.14 and comparison between Fig. 3.15b and Fig. 3.15c), but with a bigger average diameter, as shown in Fig. 3.14 (cf. also solid and dashed lines in Fig. 3.15a). The bigger value of the mean diameter at these positions could be due to a superimposition of irradiation induced and thermally activated pore-growth. Being the latter absent in the HBS and on the adjoining zone, the mean pore diameter results smaller than in the dark zone.
In Fig. 3.16 the results of the 80 GWd/tHM sample are reported. The mean diameter is quite scattered along the radius, but approximately constant around 0.5 μm, while there is a noticeable increase in the mean size in the outermost periphery of the pellet ($r/r_0 > 0.98$). The pore density drops correspondingly. A less evident drop in the pore density can be seen also in Fig. 3.14 at $r/r_0 = 0.99$. An analysis of the evolution of the pore density and mean diameter as a function of the local burnup is carried out in the next section.

Also the grain structure in the two samples was analysed opening fresh fracture surfaces on the pellet surfaces. From observation of SEM pictures obtained on fresh fracture in the sample with 67 GWd/tHM, the grain restructuring process in the dark zone appears much less developed than at the onset of the HBS (cf. Fig. 3.17a and Fig. 3.17c). The

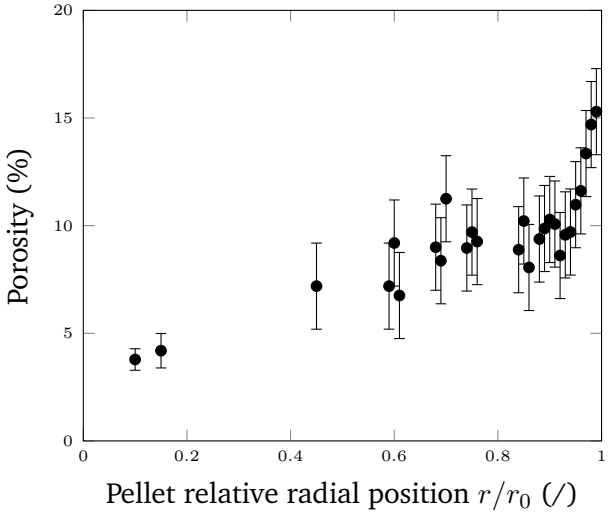

Figure 3.13.: Porosity radial profile for the sample with average burnup 80 GWd/tHM.

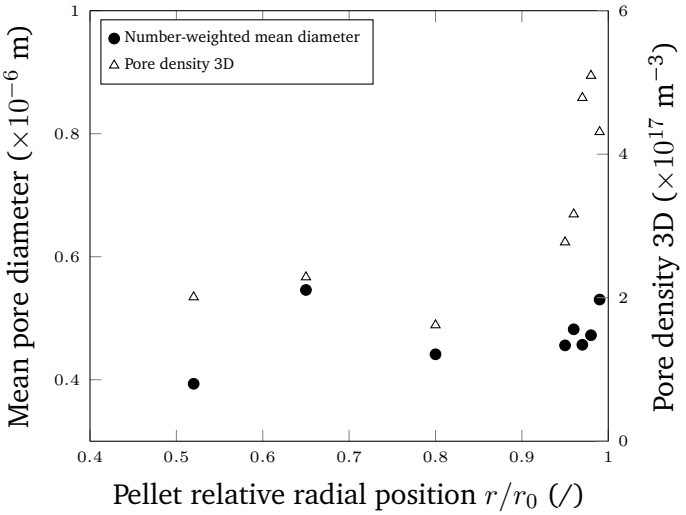

Figure 3.14.: Estimated mean pore diameter and pore density as a function of pellet radius for the sample with 67 GWd/tHM average burnup.

typical sub-micrometer polyedral grains are not visible in Fig. 3.17a, whereas they appear on the left and upper part of Fig. 3.17c. Electron Backscatter Diffraction (EBSD) analysis would be necessary to perform an orientation mapping of the crystals and verify possible initiation of polygonization.

Occasionally, on the surface of bigger pores, round sub-grains are visible (indicated by the black arrows in Fig. 3.17a). Such type of sub-grains are often associated to free surfaces or original grain boundaries [37, 39], as can be seen in Fig. 3.17b. The

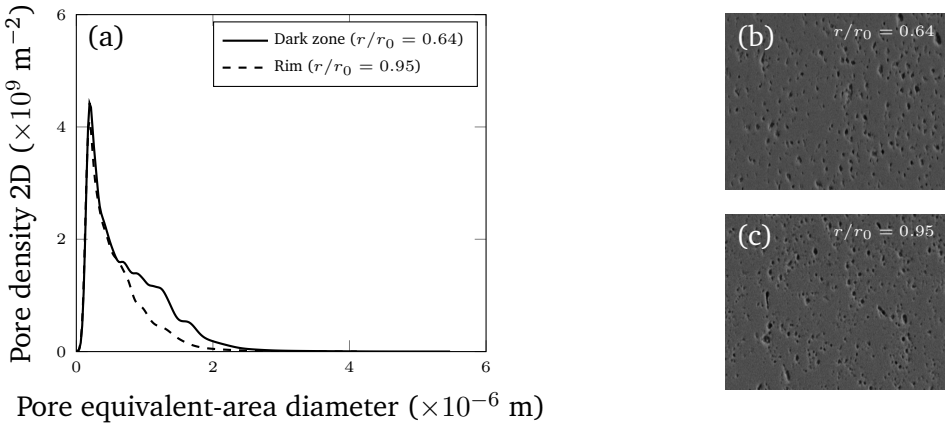

Figure 3.15.: (a) Measured 2D pore size distribution (adaptive kernel) in the dark zone (solid line) and at the onset of the HBS structure (dashed line). (b)-(c) SEM micrograph of polished surface in the dark zone ($r/r_0 = 0.64$) and at the onset of the HBS ($r/r_0 = 0.95$), respectively.

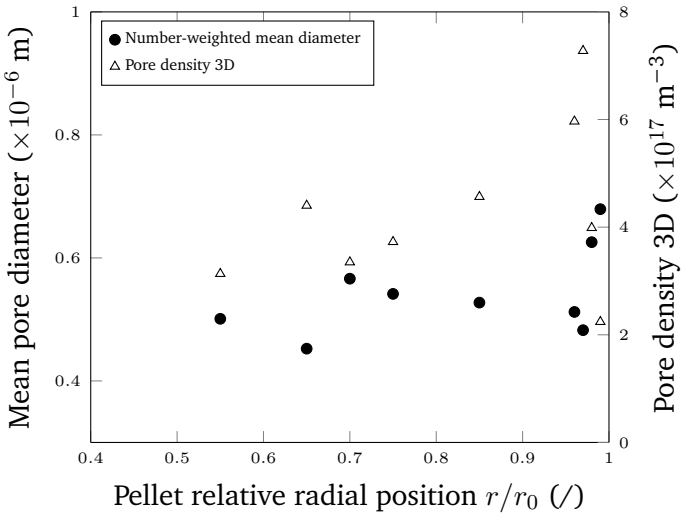

Figure 3.16.: Estimated mean pore diameter and pore density as a function of pellet radius for the sample with 80 GWd/tHM average burnup.

preferential location of rounded subdivided grains at surface of pores or free surfaces is a recognised feature of high burnup fuels [37, 39, 57]; their presence has been revealed even far from the pellet rim [39]. Rounded subgrain formation has been reported also for ion-implanted UO_2 using high energy (300 keV to 500 keV) Xe ions at high dose [23]. Interesting observations about the evolution of this type of subgrains were possible on the sample with average burnup 80 GWd/tHM. The black spot visible in Fig. 3.11b is not a missing pellet fragment, rather a “natural” cavity extending through most of the pellet

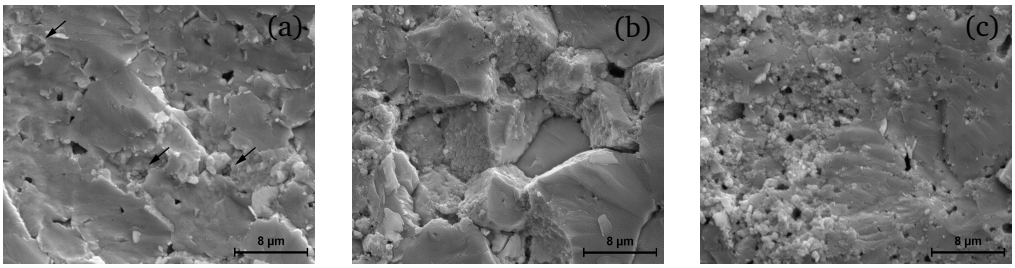

Figure 3.17.: SEM micrographs (fresh fracture surface) showing the fuel grain structure at different radial positions: (a) $r/r_0 = 0.64$ (dark zone) (b) $r/r_0 = 0.86$ and (c) $r/r_0 = 0.95$ (onset of the HBS). The black arrows in (a) indicate the round sub-grains observed on big pores surface.

radius. Through investigation of such cavity, the evolution of the original grain surface morphology at different radial locations was determined, as shown in Fig. 3.18.

In the first micrograph (Fig. 3.18a), corresponding to the central part of the pellet, the original grains, decorated on the grain boundaries with a number of metallic fission products precipitates, are visible. Already at radial positions $r/r_0 \approx 0.30$, grooves start to appear on the surface of the original grains (Fig. 3.18b). The amount of grain surface affected by the groove formation increases while proceeding towards the pellet periphery (Figs. 3.18c and 3.18d) till the original grain structure becomes hardly recognisable at $r/r_0 \approx 0.60$ (Fig. 3.18e). Structure morphologies similar to what observed in Fig. 3.18e are visible up to relative radial positions $r/r_0 \approx 0.85$. No open surface was present available for examination in the region $0.85 < r/r_0 < 0.95$, from which the fully restructured HBS is seen (Fig. 3.18f).

Lozano et al. observed rolls of round subgrains at radial locations far from the pellet rim [39, 187]. They concluded that the formation of such grains was due to a different mechanism with respect to the polyedral subgrains of the HBS, and they suggested a stress-induced surface modification due to the heterogeneous segregation of fission products (in particular metallic fission products and fission gases) on the grain surfaces. If the round subgrains formation were induced only by the segregation of fission products, they should be visible also in the central part of the pellet. Instead, the fact that the round subgrains are not visible in the centre and their formation increases towards the pellet periphery suggests that a temperature threshold for their formation exists. This would be consistent with the occurrence of subdivision processes similar to HBS formation. Detailed information about the irradiation history of this sample is not available at the time of writing. However, an approximated irradiation history has been published in [4]. By comparing it with the irradiation history of another high burnup fuel for which the end-of-cycle temperatures have been reported [41] (Fig. 3.19), an estimation of the temperature profiles in the sample here analysed could be obtained (Fig. 3.20).

Although the temperatures reported in Fig. 3.20 are to be considered only approximative, at the radial positions where no significant surface groove can be seen, namely $r/r_0 <$

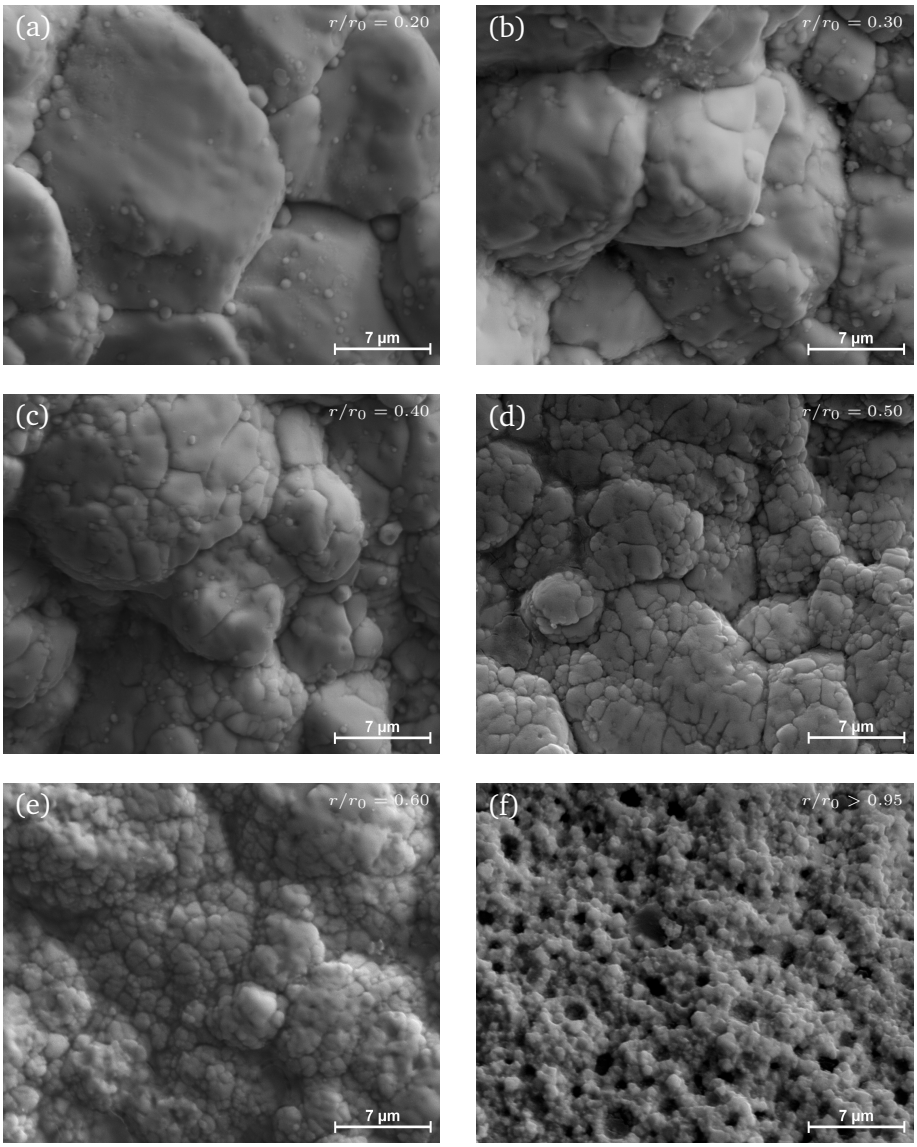

Figure 3.18.: (a)-(f) SEM images of the sample with average burnup 80 GWd/tHM showing the grain structure in a cavity cutting through the pellet radius.

0.30, the fuel has experienced during all the irradiation period temperatures above the temperature threshold for which most of the irradiation-induced defects are completely annealed [95]. This fact would suggest that the mechanism responsible for the formation of the round subgrains is related to irradiation-induced defect accumulation, which is inhibited at high temperature due to thermal recovery. Fresh fracture images taken at relative radial positions $r/r_0 \approx 0.7$, see for example Fig. 3.21, show appreciable round-subgrain formation at the pore surfaces, but the grain subdivision phenomenon is not

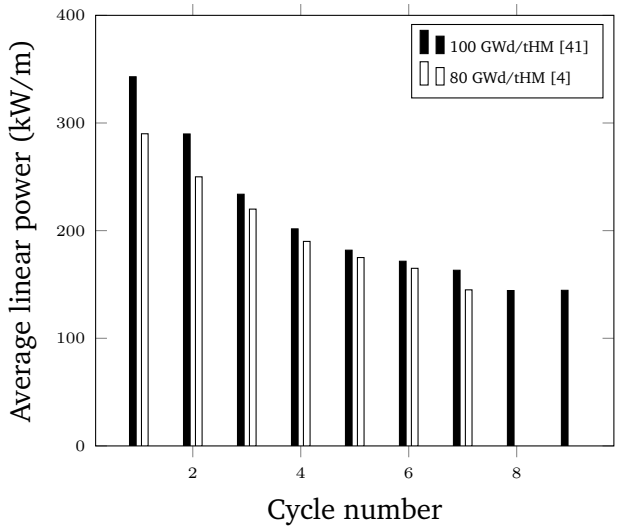

Figure 3.19.: Irradiation history for the sample analysed in this work (according to [4]) and for a sample analysed in [41].

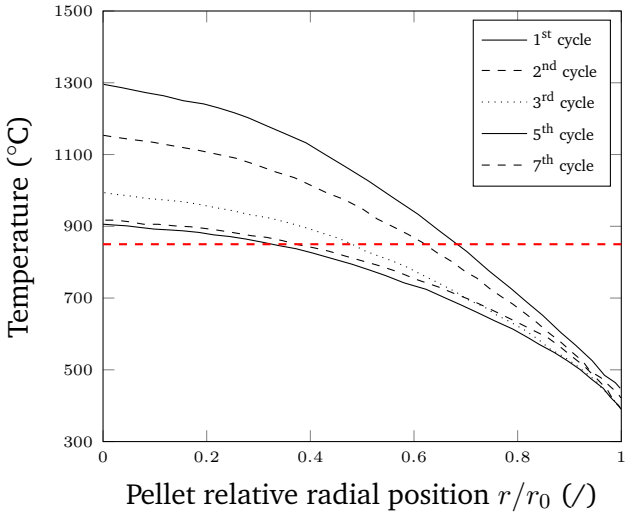

Figure 3.20.: Temperature profiles for the sample in [41], taken as approximate reference for the sample with 80 GWd/tHM used in this work.

yet developed in the bulk, confirming that free surfaces are preferential sites for grain subdivision. As for the previous sample, further investigations using EBSD would help in obtaining direct insight in claryfing grain orientation and subdivision.

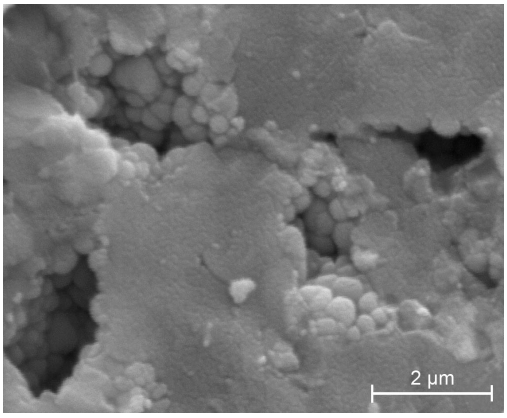

Figure 3.21.: Representative SEM-micrograph of fresh fracture surface at relative radial position $r/r_0 \approx 0.7$ for the sample with 80 GWd/tHM. Rounded sub-grains are visible around the pores, whereas no clear evidence of grain subdivision is visible in between the pores.

3.2.2. Stereological evolution of the pores in the HBS and ultra-high HBS

The methodology introduced in Section 2.4.3 was employed to study the evolution of the pore size distribution and related quantities (i.e., mean pore size and total pore number density) as a function of the local effective burnup. The local effective burnup is defined as the local burnup integrated under 1000 °C [188, 189].

Three commercial samples were analysed, with pellet average burnup 67, 80 and 100 GWd/tHM, respectively. Also the special irradiation discs from the NFIR program were investigated. The samples characteristics are summarized in Tables 2.1 and 2.2.
The radial profile of both local and local effective burnup are reported in Figs. 3.22a and 3.22b for the samples at 67 and 100 GWd/tHM, respectively. The burnups were calculated using the TRANSURANUS fuel performance code [190, 191], on the basis of the fuel rods characteristics and irradiation histories provided in [157, 192]. Concerning the rod with an average burnup of 80 GWd/tHM, local burnup calculations were already reported elsewhere [81]. Concerning this last commercial sample, only the extreme periphery (i.e., $r/r_0 > 0.96$) was analysed in this part of the work, therefore at those radial positions the local burnup coincides with the local effective burnup. The NFIR samples were irradiated isothermally below 1000 °C (Table 2.2), therefore the nominal burnup can be considered equal to the effective burnup.

In case of the commercial fuel samples (Fig. 3.23), each image was divided in bands of 50 µm in the pellet radial direction. The total area analysed for each radial position was between 12 000 µm^2 and 34 000 µm^2, depending on the sample. The main limitation was due to the presence of extensive cracking on the surface, particularly for the sample with average burnup 100 GWd/tHM. For each radial position, the corresponding value of local burnup is obtained from the calculations of radial burnup profiles (Fig. 3.22). For the NFIR discs, which are homogeneous in terms of burnup and irradiation temperature,

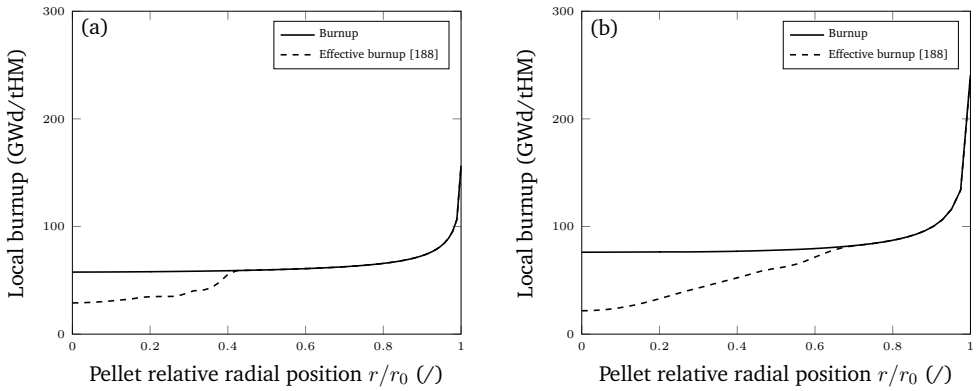

Figure 3.22.: Radial burnup and effective burnup profile of the sample with average burnup (a) 67 GWd/tHM, (b) 100 GWd/tHM, calculated with the TRANSURANUS fuel performance code.

the full image area is analysed. The investigated area ranged between 124 000 μm^2 and 144 000 μm^2.

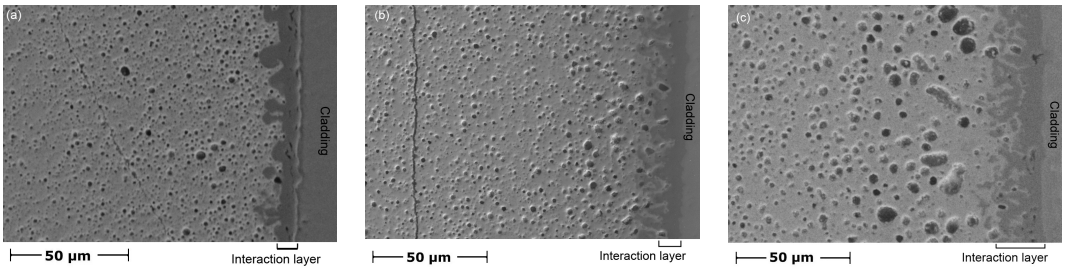

Figure 3.23.: SEM micrographs of the peripheral region of the samples at (a) average burnup 67 GWd/tHM, (b) 80 GWd/tHM, and (c) 100 GWd/tHM [123]. Magnification: 500x.

The data were processed as explained in Section 2.4. At the same time, I tested the hypothesis if a log-normal distribution could be assumed in any burnup range. Quantile-quantile plots (Fig. 3.24) suggest that at relatively low level of porosity the data are fairly represented by a log-normal distribution (Fig. 3.24a). Upon increasing porosity and local burnup all the data analysed showed deviation from the log-normal behaviour, being more long-tailed than a log-normal distribution (Figs. 3.24b, 3.24c and 3.24d).

Figure 3.25 shows some examples of the measured 2D distributions and the corresponding 3D distributions using the adaptive kernel estimator and a log-normal fit of the data.

Upon checking the consistency of the estimation (cf. Eq. (2.8)), the adaptive kernel method better estimates the porosity at high values of porosity (Fig. 3.26). As anticipated,

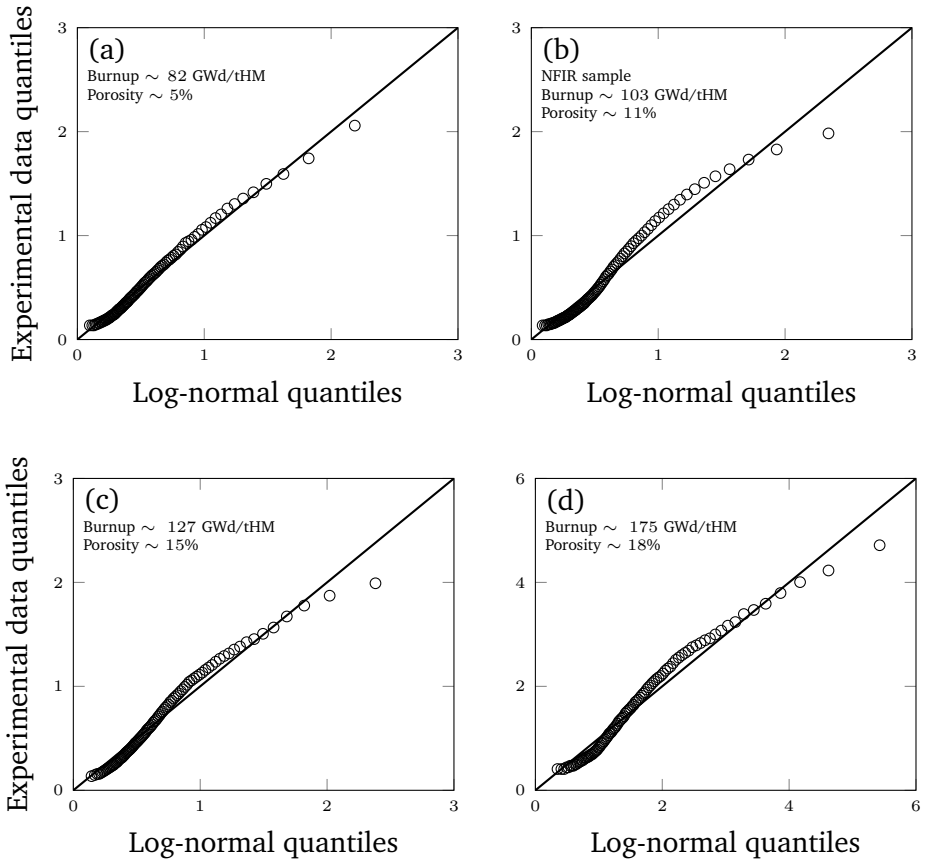

Figure 3.24.: Quantile-quantile plots of the measured 2D pore diameters at different values of porosity and local burnup [123].

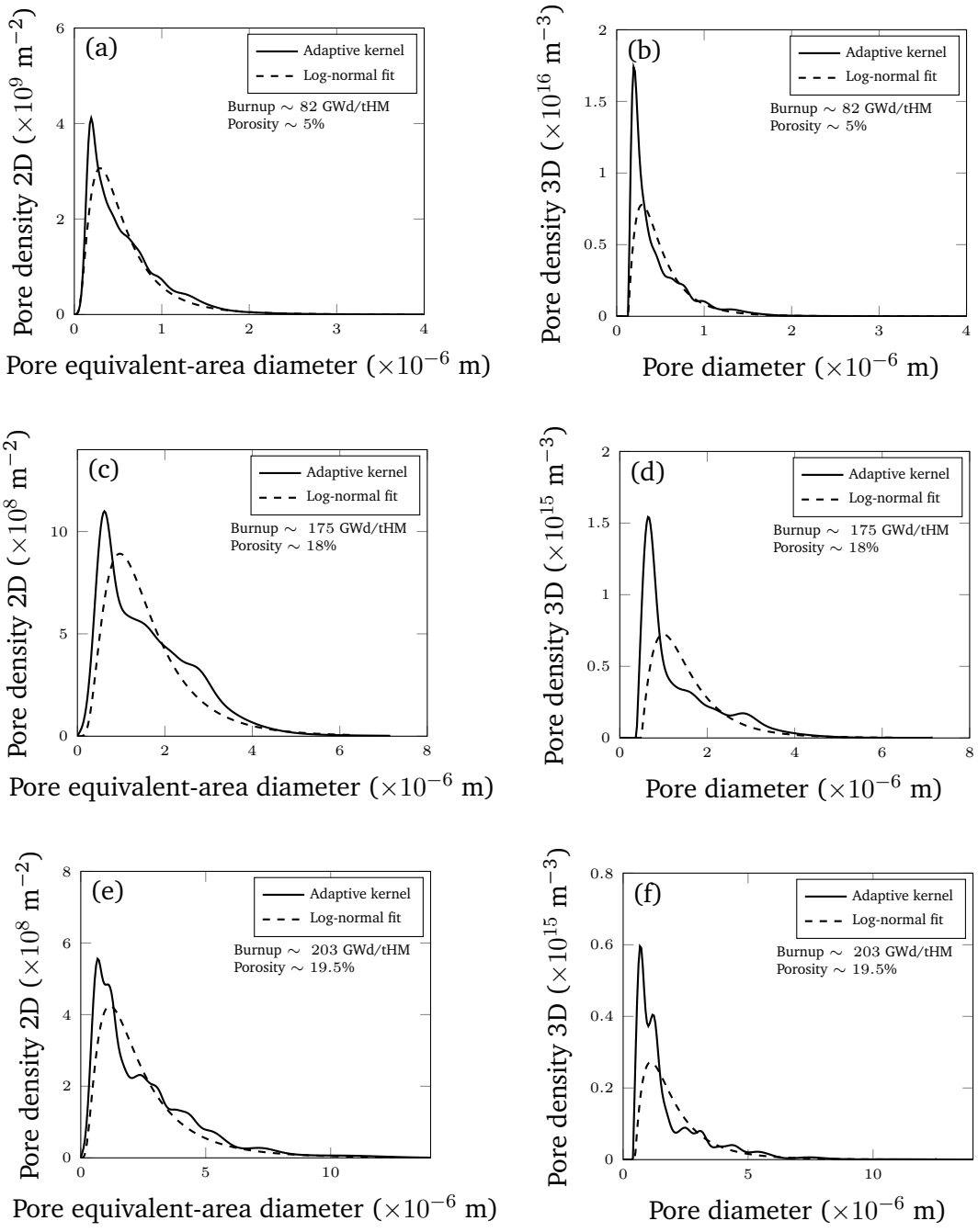

Figure 3.25.: Comparison of the estimated 2D and 3D pore density using the adaptive kernel estimator (solid line) and the log-normal fit (dashed line) [123].

at high values of burnup and porosity, i.e. above 150 GWd/tHM and above 0.15 respectively, the deviation from the log-normal behaviour increases (Fig. 3.24). The log-normal distribution does not account for the larger pores measured (see for example Fig. 3.25c) which, although less abundant, contribute the most to the void fraction. Therefore, using the log-normal fit at very high values of porosity causes underestimation of the volume porosity.

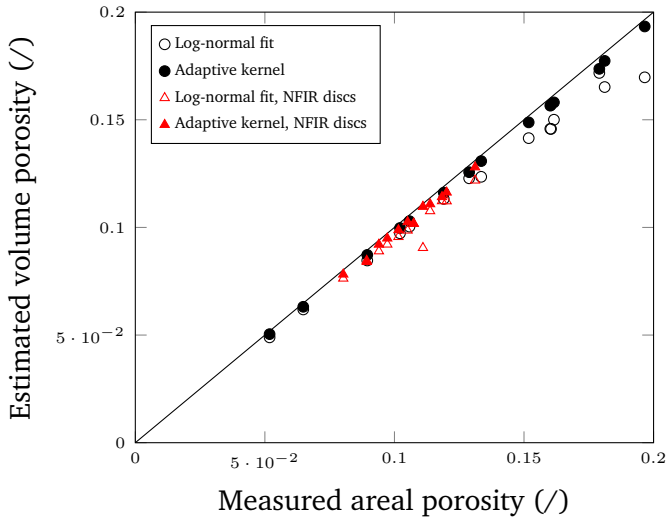

Figure 3.26.: Estimated volume porosity versus the measured areal porosity using the adaptive kernel estimator and the log-normal fit. For the two NFIR discs the comparison is made for each set of images [123].

At burnup values above 150 GWd/tHM, multi-modal distributions have been reported for 2D data (see Fig. 4 in [41]). By inspecting Figs. 3.25c to 3.25f the possible bimodal nature of the distributions is difficult to discern. The bimodality could be easily masked by data scatter resulting in wiggles using the kernel density estimation. I tried to assess bimodality of this two sets of data (i.e., taken from the images corresponding to the regions with 175 GWd/tHM and 203 GWd/tHM) by calculating the bimodality coefficient (BC) [193]

$$BC = \frac{s^2 + 1}{\kappa + \frac{3(n-1)^2}{(n-2)(n-3)}} \tag{3.5}$$

where n is the number of pores in the image, s and κ the sample's skewness and excess kurtosis, both corrected for the sample bias [194]. The calculated BC coefficients were 0.52 and 0.58, respectively. Only in the second case, a weak indication of bimodality appears. However, the coefficient is only indicative, because heavy-tailed distributions have small values of BC regardless of the number of modes [193, 195]. On the basis of such weak indication of bimodality, the present results do not clearly confirm the presence of multiple peaks in the pore size distribution at very high burnup.

From the 3D pore size distribution, in addition to the total pore density, the mean diameter can also be calculated. Clearly, the results of both total pore density and mean diameter will be biased by the resolution limit. However, the current resolution limit (≈0.13 μm) is considered sufficient to account for the pores that will contribute most to the total porosity. The results of the adaptive kernel estimator and the log-normal fit of the data are reported in Figs. 3.27 and 3.28. The total pore density is shown in Fig. 3.27 as a function of the local burnup for the two cases.

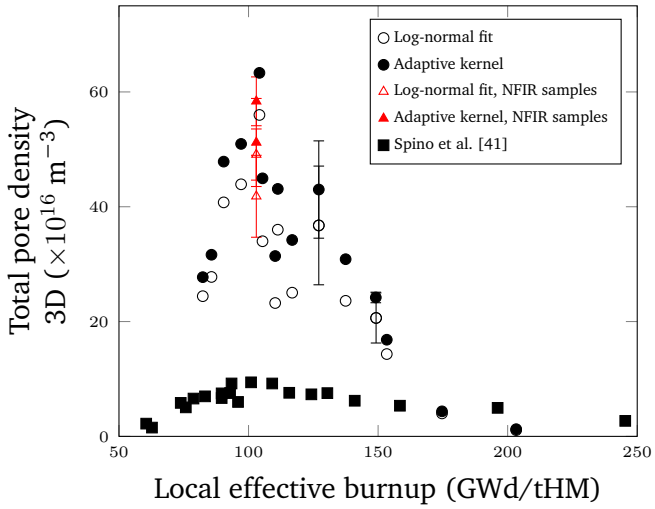

Figure 3.27.: Estimated total pore density as a function of the local burnup. For the commercial fuels, error bars are added when the analysis could be performed on different radius of the cross-section. In the case of the special irradiation discs of the NFIR project, the results represent the average of several sets of images at various locations with error bars being 95% confidence bands [123].

The number-weighted and volume-weighted mean diameter were calculated according to the following formula,

$$\overline{d} = \frac{\sum_{i=1}^{N} w(i)d(i)}{\sum_{i=1}^{N} w(i)} \tag{3.6}$$

where $d(i)$ have the same meaning as in Eq. (2.8) and $w(i)$ are the weighting factors for each class. For the number-weighted mean (Fig. 3.28a), the factors $w(i)$ correspond to the pore number density in each class $N_v(i)$, whereas for the volume-weighted mean (Fig. 3.28b) they are proportional to the pore volume in each class, namely $d(i)^3 N_v(i)$. In addition, the cubic root of the third moment of the pore size distribution, which is proportional to the pore mean volume, has been calculated as well (Fig. 3.29).

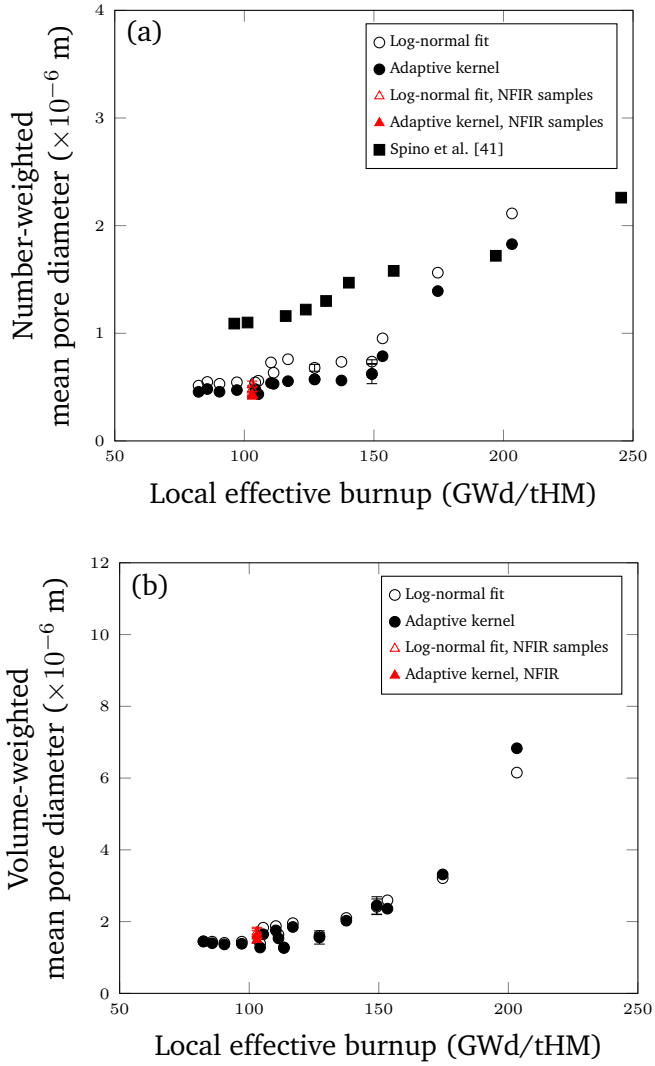

Figure 3.28.: Estimated (a) number-weigthed and (b) volume-weigthed mean pore diameter as a function of the local burnup. For the commercial fuels, error bars are added when the analysis could be performed on different radius of the cross-section. In the case of the special irradiation discs of the NFIR project, the results represent the average of several sets of images at various locations with error bars being 95% confidence bands [123].

At each value of local burnup, the estimations of total pore density, number-weighted, volume-weighted mean diameter and the cubic root of the third moment of the pore size distribution obtained using a log-normal fit are comparable to the estimations obtained with the more general adaptive kernel.

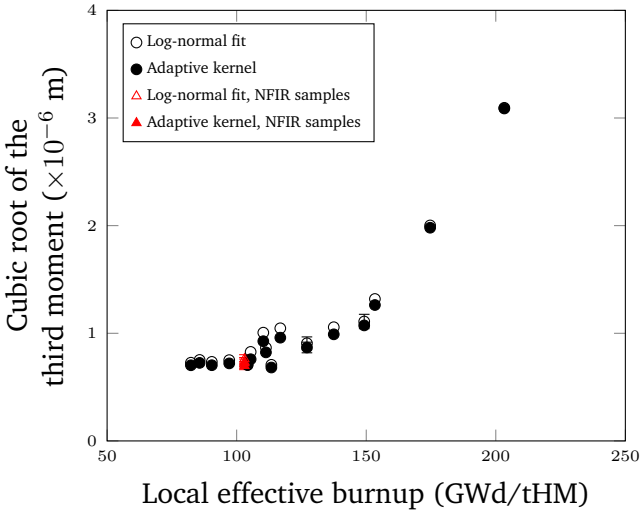

Figure 3.29.: Calculated cubic root of the third moment of the pore size distribution. For the commercial fuels, error bars are added when the analysis could be performed on different radius of the cross-section. In the case of the special irradiation discs of the NFIR project, the results represent the average of several sets of images at various locations with error bars being 95% confidence bands.

The results obtained in this work were compared to the available literature data for similar samples [41]. In this work, in the range 80-140 GWd/tHM, the estimated total pore density is higher and the mean pore radius smaller. The discrepancy is likely to arise from the different magnifications used to acquire the data, which results in different resolution limits. I used two magnifications (1500x and 500x) in order to increase the accuracy in the measurements of small pores, resulting in higher pore density and smaller mean diameter. Another source of discrepancy could arise due to the improved methodology employed here which should decrease the underestimation of the total pore density related to the use of the Schwartz-Saltykov method [152]. Instead, a similar critical burnup threshold around ≈100 GWd/tHM is observed as in [41] above which pore coarsening occurs. This is evident from the drop in the total pore density and increase in the mean pore diameter starting from ≈100 GWd/tHM. A preliminary model that could give an explanation of the physical mechanism underlying such behaviour is discussed in Chapter 4.

4. Preliminary model for the fission gas behaviour in the HBS

If you're not prepared to be wrong, you'll never come up with anything original

Ken Robinson

Abstract *The experimental determination of the porosity, pore number density and mean radius as a function of the local effective burnup is complemented in this last part of the thesis with modelling of the fission gas behaviour in the HBS, with particular focus on the coarsening mechanism experimentally observed above 100 GWd/tHM. The pore size increase is attributed to a mechanism of pore coalescence as a consequence of geometrical overlapping of growing pores. The rate of coalescence is modelled based on the formalism of the nearest-neighbour statistic of hard spheres, derived by Torquato [196]. The modelling approach, kept as simple as possible and with a limited amount of parameters, is specifically targeted to future application in engineering-scale fuel performance codes.*

4.1. Introduction

The relationship between fission gas behaviour and HBS formation is one of the key issues systematically addressed when dealing with fuel performance at high and very high burnup [2, 3, 22, 24, 197, 198]. It is accepted that the fission gas is depleted from the fuel matrix [35] and several studies have clearly demonstrated that most, possibly all, of the fission gas locally generated in the fuel periphery is retained in the HBS porosity [5, 17, 66, 67, 69, 70]. Much less is known about the physical mechanisms responsible for the HBS depletion and concomitant porosity formation and growth (see also discussion in Section 1.2.2).

In non-restructured irradiated fuels, the fundamental physical processes commonly considered to describe the kinetics of fission gas swelling and release comprise (a) single atom gas diffusion within the grain volume, (b) trapping and resolution from intragranular bubbles, (c) diffusion-controlled precipitation in intergranular bubbles, (d) resolution from the grain boundary to the grain interior and, eventually (e) grain boundary bubbles interconnection leading to fission gas release [199, 200]. It is not

straightforward if and to which extent those processes can be applied to the fission gas kinetics in the HBS, due to the different microstructure configuration with respect to the initial one (see Section 1.2). The uncertainty pertaining to the physical phenomena involved is reflected in the variety of models that have been proposed to describe the fission gas behaviour in the HBS. In the open literature, the models used in the fuel performance codes range from purely empirical to fully-mechanistic.

One of the first models was proposed by Lassmann and co-workers. An empirical first order differential equation is used to calculate the Xe depletion from the fuel matrix as a function solely of the local burnup [27]. At the same time, the porosity growth is linearly related to the local burnup increase, till a saturation level is reached [201]. The two phenomena are not related, but derived directly from EPMA and image analysis data, respectively. These two models are currently used in the TRANSURANUS code [202].

Veshchunov and Shestak [59] developed a model which predicts the macroscopic characteristics of the fuel (e.g., the fission gas release) from the mechanistic description of point and lineal defects evolution (e.g., vacancies, interstitials and dislocations) and their interactions with volume defects such as bubbles and pores. In particular, the fuel restructuring is associated with the dislocation density decrease predicted by the model in the temperature range 1000 °C–1100 °C. The model shows good agreement with the experimental results of dislocation density concentration [59], but it contains a considerable number of parameters whose value cannot be verified directly. Growing of the pores is considered as a consequence of vacancies and interstitials precipitation and resolution [59]. The models are currently implemented in the MFPR code. In a later work, Tarasov and Veshchunov [203] extended several models for fuel porosity evolution in UO_2. At very high burnup, pore coalescence due to their growth and impingement is taken into account, assuming that the pores are Poisson distributed, i.e., that they are a system of randomly distributed overlapping spheres [204]. No comparison with experimental data was made in this first paper and the model of pore coalescence could not be verified. This year, Veshchunov and Tarasov [205] extended the model previously presented by including the effect of triple impingement, since consideration of solely pair interactions underestimated the pore number density decrease reported by Spino [41].

Noirot et al. [206, 207] relates the fraction of fuel that undergoes restructuring to the fraction of fuel that has reached a certain critical value of dislocation density. The dislocation density evolution is modelled empirically as a decay process, depending on fission density and temperature. It is assumed that upon switching from the non-restructured geometry to the restructured one the swelling is conserved. That implies that the gas previously contained in intra- and intergranular bubbles is transferred to a new population of spherical pores. The HBS pore nucleation is not addressed in a mechanistic manner, instead an initial number of pores per unit volume is assumed, based on experimental observation. While the restructuring process proceeds, new HBS pores nucleate proportionally to the amount of restructured fuel volume. Subsequently, the HBS pores grow by trapping of the gas generated in proximity of the pore. The trapping of the gas by the closed pores leads to departure from mechanical equilibrium, which, generally, results in pore growth. A second term related to the precipitation

of vacancies is considered, based on the corresponding equations of the fundamental diffusion-controlled reaction rate theory in the mean-field approach [208]. A large multiplication parameter (of the order of $\approx 1 \times 10^5$) is added to this term to enhance pore growth. The introduction of such parameter is qualitatively justified by a possible low-temperature sliding of the HBS subgrains, based on the observation of a remarkable interdiffusion layer between the fuel and the cladding [207]. However, there is no clear experimental evidence supporting this supposition, which remain largely speculative. No coalescence or interaction mechanism among the pores is considered. This could set a limit to the burnup range of applicability of the HBS model, since pore coarsening is clearly experimentally observed at very high burnup [41, 43, 67, 123]. This model is part of the more general code MARGARET, which calculates the fission gas behaviour in nuclear fuels. The model is currently used in the fuel thermomechanics codes METEOR and ALCYONE.

The Gas Release and gaseous SWelling Advanced (GRSW-A) model by Khvostov et al. [209] describes the polygonisation process based on the Kolmogorov-Johnson-Mehl-Avrami equation [210]. The fraction of grains which polygonises is dependent on the local effective burnup, and an empirical proportionality constant takes into account the possible different initial grain sizes, which influence the subdivision process [11]. The gas mass balance equations are solved in a cell domain smaller and smaller, due to the progressive grain size reduction following polygonisation, resulting in gas depletion in the grains as a consequence of an increasing gas flux across the cell boundary. The polygonisation process is assumed to start at the original grain boundaries. Therefore, the spherical HBS pores are predominantly formed on the grain boundaries, due to shape relaxation of the lenticular pores favoured by the grain sub-division. This assumption can be considered appropriate in general, but not in the case of large grain fuels, which show formation of pores in the interior of the original grains [11, 211]. The gas depleted from the grains is collected on the grain boundaries. Here, the gas can either form a new gas cluster (i.e., a fixed-size object) or precipitate in the already existing pores. Pore growth proceeds via trapping of gas and point defects. The rate of point defect precipitation is calculated also in this case considering an effective-medium approach [208]. The vacancies mobility in the HBS is increased by using an effective diffusion coefficient dependent on the surface self-diffusion coefficient pre-exponential, the uranium-vacancy self-diffusion coefficient and the fraction of restructured fuel volume [209]. Further growth is due to compound interactions between pores (coarsening), which are accounted for using a probabilistic theory [212]. Fission gas release is also considered in the model, based on the probability that a closed pore interacts with either an open surface or an already vented pore [212]. The model has been implemented in the START-3 code and FALCON [209].

In his work, Blair [13, 213] proposed a one-dimensional, steady-state model which considers grain boundary diffusion as the main transport mechanism in addition to two of the processes commonly considered in fission gas release models (i.e., volume diffusion within the fuel matrix, including the precipitation of single atoms into intra-granular bubbles, and precipitation and growth of grain boundary gas bubbles). Grain boundary diffusion is normally neglected in the non-restructured fuel, since the diffusion mean free

path is comparable to or smaller than the average width of the grain face [214]. According to [13], since in the HBS the concentration of grain boundaries dramatically increases following grain-size reduction, grain boundary transport mechanisms are dramatically enhanced, resulting in Xe depletion from the matrix. The porosity growth/shrinkage, coarsening and venting are modelled on the basis of the reaction rate equations reported by Khvostov et al. [209]. Such approach has been applied to model HBS porosity growth both under out-of-pile annealing tests [215] and under in-pile conditions [13], on the basis of PIE results [41,43]. Also in this case an enhanced vacancy diffusion coefficient (3 orders of magnitude higher than the vacancy athermal diffusion coefficient recommended in [216]) was used to reproduce the porosity increase above 100 GWd/tHM reported in [41]. The model has been integrated in the SPHERE fission gas model [217].

The empirical model by Lemes et al. [218], used in the DIONISIO code [219], is a modification of the depletion model by Lassmann et al. [27], which takes into account the isotopic ratio between Xe and Kr. The porosity evolution is based on the model by Blair et al. [215].

Recently, Pizzocri et al. [191] proposed a new semi-empirical model to describe the formation and Xe depletion in the HBS. The main new contribution of this model is the description of grain recrystallisation/polygonisation and intragranular Xe depletion as two mechanisms inherently related. An exponential reduction of the average grain size with local effective burnup is assumed, based on grain size measurements in partially restructured zones. The grain size reduction is paired with a simultaneous depletion of intra-granular fission gas, due to the decrease in the intragranular diffusion distance. The model shows good agreement with the experimental EPMA results. Two strong points of the model are (i) the coupling of the grain size reduction with the intragranular fission gas behaviour on a physically sound basis, but with a degree of complexity suitable for applications in integral fuel performance codes, and (ii) the capability of predicting the HBS formation delay reported for large-grained fuels [211,220].

The results reported in [191] were the first step towards a more consistent modelling of the phenomena involved in the HBS formation and porosity evolution, in the framework of a collaborative project with D. Pizzocri. Extension of this model to include the growth of the HBS pores is reported in [221]. In addition to the experimental investigations, my task consisted in extending the gas bubble growth model in order to take into account the bubble coarsening experimentally observed (see Section 3.2.2 and [41,43]). Given the influence of the pore growth mechanisms on the pore coarsening, the main pillars of that part of the model are firstly briefly summarised in the next section. In the last section, the model for the pore coarsening is outlined.

4.2. Fission gas accumulation and HBS pore growth

While burnup accumulation proceeds, the progressive reduction of the mean grain size results in an increased total grain surface-to-volume ratio. The formation of new HBS pores is assumed to be directly proportional to the surface-to-volume increase. The pores

are considered to be spherical, monodisperse with radius R_p. The initial concentration of pores is directly proportional to the original grain surface-to-volume ratio [191]. From Eq. (2) in [191], the number density of pores N_v that nucleate per fuel unit volume (m^{-3}) can be written as

$$\frac{dN_v}{dt} = -K\frac{3}{a^2}\frac{da}{dt} \tag{4.1}$$

where a (m) is the grain radius, t is a general measure of time, which can be thought to be the local effective burnup bu_{eff} (GWd/tHM), and K (m^{-2}) is the proportionality constant. The new pores are assumed to contain an initial gas quantity n_{g0} (atoms), which is a model parameter. An initial pore radius R_{p0} (m) pertains to such concentration according to the following equation

$$\frac{4}{3}\pi {R_{p0}}^3 = n_{g0}\,\omega \tag{4.2}$$

where ω (m^3) is the xenon Van der Waals atomic volume, equal to 8.50×10^{-29} m^3. During the grain size reduction phase, the mean pore radius is calculated as number-weighted average between the growing pores with radius R_p and the new pores which have nucleated with initial radius R_{p0}.

A cell-model is used to describe the pore growth [199]. The fuel volume can be schematically represented as being composed of a 3D regular array of volume-equivalent spherical Wigner-Seitz cells surrounding each pore (see Fig. 4.1 for a representation of a planar section) [199, 221].

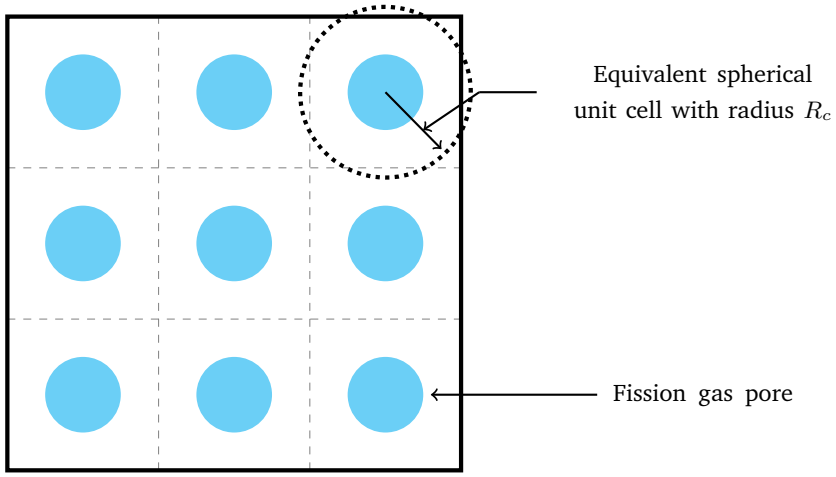

Figure 4.1.: Schematic representation of the cell model used for modelling the pore growth [221].

In each cell, the gas that diffuses out of the grain interior precipitates at the sub-grain boundaries. No resolution back to the grain interior is considered. Within the cell, the gas on the grain boundaries diffuses towards the pores, acting as perfect sinks. Due to

the high density of traps typically encountered in HBS, competition between the sinks is accounted for in the reaction rate [222]

$$k = 4\pi D_{gb}^{Xe} R_p (1 + 1.8\phi^{1/3}) \tag{4.3}$$

where D_{gb}^{Xe} ($m^2\,s^{-1}$) is the Xe grain boundary diffusion coefficient, R_p (m) is the pore radius, and ϕ is the fuel porosity, i.e.

$$\phi = N_v \frac{4}{3} \pi {R_p}^3 \tag{4.4}$$

The inflow of gas atoms causes departure from mechanical equilibrium. The pore overpressure is calculated as

$$\Delta p = p - p_{eq} \tag{4.5}$$

where p_{eq} (Pa) is the equilibrium pressure, and p (Pa) is the pore pressure which, for a Van der Waals' gas, is

$$p = \frac{k_b T}{\Omega - \xi\,\omega}\,\xi \tag{4.6}$$

where k_b ($J\,K^{-1}$) is the Boltzmann's constant, T (K) is the temperature, Ω (m^3) is the vacancy volume, and ξ is the ratio between the number of gas atoms n_g (atoms/pore) and the number of vacancies n_v (vacancy/pore) in each pore. The vacancy volume Ω is assumed equal to $4.09 \times 10^{-29}\,m^3$ [223]. The equilibrium pressure p_{eq} is determined by

$$p_{eq} = \frac{2\gamma}{R_p} - \sigma_0 \tag{4.7}$$

where γ ($J\,m^{-2}$) is the fuel specific surface energy and σ_0 (Pa) is the hydrostatic stress. The hydrostatic stress is conventionally assumed negative when compressive.

The absorption/emission of vacancies is driven by the bubble overpressure, according to Speight and Beere [224]

$$\frac{dn_v}{dt} = \frac{2\pi D_{gb}^v R_c}{k_b T F} \Delta p \tag{4.8}$$

where n_v is again the number of vacancies per pore, D_{gb}^v ($m^2\,s^{-1}$) is the vacancy grain boundary diffusion coefficient, R_c (m) is the radius of the Wigner-Seitz cell (see Fig. 4.1), and F (/) is calculated as [221]

$$F = \frac{-10\,\varphi\,(1+\varphi^3)}{\varphi^6 - 5\varphi^2 + 9\varphi - 5} \tag{4.9}$$

$\varphi = R_p/R_c$ being the ratio between the pore radius and the cell radius.
The rate of vacancy precipitation causes an increase in the pore volume V_p due to growth which can be expressed as

$$\left.\frac{dV_p}{dt}\right|_g = \frac{dn_v\Omega}{dt} \tag{4.10}$$

The hypothesis that the HBS pores are distributed based on a regular array is certainly not representative of the physical reality that suggest that the pores are randomly distributed in the fuel matrix (see for instance Fig. 3.23). However, the cell model representation is a necessary simplification to treat the precipitation of the gas and vacancies using analytical expressions.

4.3. Pore coarsening

Inert gas bubbles formed in solids may coarsen by different processes. Three mechanisms are generally identified: coalescence following bubble migration [225, 226], Ostwald ripening [227] and coalescence by impingement of growing pores [204, 228].

Bubbles with diameter larger than 2 nm have very low mobility even at temperature as high as 1800 °C [229]. At temperatures characterising the edge of the fuel pellet, the micrometric HBS pores are practically immobile. Coarsening due to migration can therefore be excluded as main driving force.

Ostwald ripening describes the resolution of particles with radius smaller than a critical radius and their re-absorption by the bigger ones, which grow at the expenses of the formers [227, 230].

Spino et al. [41] proposed this mechanism as responsible for the decrease of the pore number density in the HBS above 100 GWd/tHM, comparing the log-log plot of the pore number density and mean radius vs. burnup to the theoretical predictions. However, data uncertainties are large as compared with the small differences between the theoretically predicted slopes for Ostwald ripening and coalescence [231], making the identification of the operating coarsening process doubtful. As it was noticed in [205], for rim pores, whose internal pressure can be reasonably estimated in the range of few tens of MPa, the thermal resolution is strongly suppressed, suggesting that the mechanism is insignificant [205]. Another contradiction arises from the analysis of the pore size distribution. Ostwald ripening theories predict a negative skewed distribution [227, 230, 232], while a positive skewness is experimentally observed [41, 123].

Recently, Xiao and Long [233] developed a numerical model based on Ostwald ripening theory. Despite the model could fairly well reproduce the experimental trends by Spino et al. [41], several questionable assumptions were made. First of all, the results stem from the arbitrary assumption that pores are overpressurised at pressure for dislocation punching. Secondly, the pore radius growth rate is critically dependent on the average concentration of gas dissolved in the fuel matrix (Eq. (26) in [233]), which does not account for the intragranular gas depletion [35].

The third mechanism, i.e., coalescence by impingement, provides an alternative explanation for the observed pore coarsening. When the pores are sufficiently numerous and large, pore growth may lead to impingement between neighbour pores sufficiently

close to each other so that they will coalesce [204, 228]. For a system of randomly Poisson-distributed three-dimensional spheres in another phase, it has been shown that random contact between the spheres will occur when the phase volume fraction exceeds 8.9 % [234, 235]. The experimentally reported values of porosity encountered in the HBS largely exceed this limit (see for instance Fig. 3.13 or [38, 43, 67]), with maximum measured porosity up to 25 % [41]. The pore density drop occurring around $\approx$ 100 GWd/tHM firstly observed in [41] and confirmed in this work could be related to random pore coalescence between growing pores. The measured porosity values at that level of burnup are in fact 9-10 %, very close to the theoretical limit. In addition, a coalescence mechanism is consistent with the observed positive skewness of the pore size distribution (cf. Fig. 3.25) and with the observation of elongated cavities highlighting pore-contact onset at high burnup, as shown in the inset of Fig. 3.9 and in Fig. 3.23c. Therefore, this mechanism for pore coarsening is used in the model. Differently from the assumption of the regular array used to describe the pore growth, in order to model the pore coarsening the pores are treated supposing that they are randomly distributed in the fuel matrix. Eventually, pore growth may lead to impingement between neighbour pores sufficiently close to each other so that they will coalesce [228].

The probability of interaction will depend on the relative distance between two growing pores: they will coalesce if their centres are at distance r in the range $2R_p < r < 2(R_p + dR_p)$, being dR_p the pore radius increment due to growth (see Eq. (4.10)). In order to determine the number of interactions occurring in the system, knowledge of the spatial configuration of the pores, i.e., the knowledge of N-particle probability density function[1] would be required.

The two-point correlation functions analysed at various porosity and burnup values show an oscillating behaviour in a wide range of porosity (see Fig. 4.2), which could be ascribed to some short-range order in the spatial distribution of the pores, reflecting a spatial configuration of the pores typical of a system of randomly distributed hard spheres in a matrix [136] (see for example Fig. 2.7b). Generally, the determination of the specific N-particle probability density function for a system of hard spheres is non trivial [236].

I tried to overcome the problem by introducing some simplifying hypotheses for estimating the rate of coalescence. First of all, I suppose that the pores could be modelled as a system of equilibrium[2] hard spheres. Secondly, I consider only pair interactions. In this case, only the knowledge of the nearest-neighbour distribution function (see Appendix D) is required. Given these assumptions, the relative variation in the pore number density due to coalescence can be written as follows,

[1] The N-particle probability density function $P_N(r_1, r_2, ..., r_N, t)$ is defined so that, $P_N(r_1, r_2, ..., r_N, t)dr_1dr_2...dr_N$ is the probability of finding the centre of particle one in volume element dr_1 about r_1, the centre of particle two in volume element dr_2 about r_2 ... , and the centre of particle N in volume element dr_N about r_N at time t [236].

[2] The adjective equilibrium in this context is used referred to the spatial configuration of the hard spheres and should be considered as thermal equilibrium as opposed to nonequilibrium states, e.g. a random sequential addition process [236].

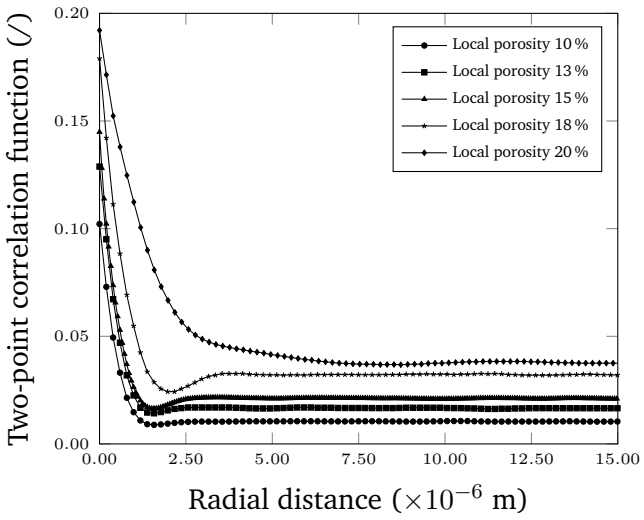

Figure 4.2.: Two-point correlation function estimated from image analysis [237] at different values of local porosity.

$$\left.\frac{dN_v}{N_v}\right|_c = -\frac{1}{2}\int_1^{1+\frac{dR_p}{R_p}} H_p(x)dx \tag{4.11}$$

where x is the normalised distance $x = r/2R_p$ and $H_p(x)$ is the nearest-neighbour distribution function for hard spheres defined in Eq. (D.3) [196]. The factor $1/2$ in Eq. (4.11) avoids counting twice the pair interactions. Equation (4.11) is solved numerically using the semi-empirical Euler method and root finding (Appendix C).

Once a coalescence event occurs, the volume of the interacting pores is preserved [238]. Moreover, the spherical geometry of the pores is immediately restored after coalescence. This assumption implies that the mechanisms of vacancy diffusion along the deformed pore geometry are fast in comparison with the rate of coalescence.

No fission gas release from the HBS pores is considered in the present model. In a 3D geometry comprising spherical pores in a matrix, the theoretical percolation threshold is reached for porosity fractions exceeding 0.2895 [239], which are well above the currently maximum values of porosity measured in the fuel. In addition, 3D-image analysis reconstruction performed on very high burnup fuel showed no significant pore tunnels [70]. Some fission gas release might occur through direct contact between the pores and open surfaces. Under normal operating conditions, the open surfaces can be expected to be small. To my knowledge, there is no data that could be used to estimate the density of open surfaces. Therefore, at this stage, I preferred not to introduce release from open surfaces, in order to avoid the introduction of an additional, arbitrary parameter in the model.

4.4. Stand-alone modeling and comparison with the experimental data

The new models of HBS depletion [191] and fission gas swelling ([221] and Section 4.3) were coded as stand-alone version. The computer program gathers as input some information about the local environment of the fuel relevant for the modeling of fission gas behaviour in the HBS. This comprises fuel fabrication data (e.g., initial porosity ϕ_0 and fabrication grain size a_0), local fission density, temperature and hydrostatic stress. The model parameters used are listed in Table 4.1.
The Xe intra-granular diffusion coefficient suggested by Brémier and Walker [240] was used for the intragranular diffusion process [191]. For the expression of the Xe grain boundary diffusion coefficient D_{gb}^{Xe} ($m^2\,s^{-1}$), the model adopted by Turnbull [241] was employed, based on the values suggested by Matzke [200]

$$D_{gb}^{Xe} = 10^{-8}\exp(-\frac{4.8\cdot 10^{-19}}{k_b T}) + 5.64\cdot 10^{-25}\sqrt{\dot{F}}\exp(-\frac{1.9\cdot 10^{-19}}{k_b T}) + 10^{-39}\dot{F} \quad (4.12)$$

where k_b and T have been previously defined and $\dot{F}$ ($m^3\,s^{-1}$) is the local fission density. The same was done for the vacancy diffusion coefficient D_{gb}^{v}, which was taken equal to [216, 228]

$$D_{gb}^{v} = 8.86\cdot 10^{-6}\exp(-\frac{5.75\cdot 10^{-19}}{k_b T}) + 10^{-39}\dot{F} \quad (4.13)$$

Table 4.1.: In-pile HBS fission gas behaviour model parameters.

Parameter	Value	Units
K	4.5×10^{10}	m^{-2}
R_{p0}	0.25×10^{-6}	m
σ_0 [a]	-20×10^{6}	Pa
$\dot{F}$	1.2×10^{19}	$m^{-3}\,s^{-1}$
T	900.15	K
a_0 [b]	13.5×10^{-6}	m
ϕ_0	4	%

[a] The hydrostatic stress is assumed negative when of compressive type.
[b] 3D diameter

In Figs. 4.3 to 4.5 the model predictions (solid lines) are compared to the experimental results (circles) reported in the previous chapter. In each figure, also the results using the coalescence model introduced by White [228] are reported, adapted for a 3D geometry. White's model can be derived from Eq. (4.11) by using the nearest-neighbour density function for overlapping spheres (Eq. (D.1)) instead of the one for hard spheres. By expanding the exponentials in Taylor's series at the first order, one obtains

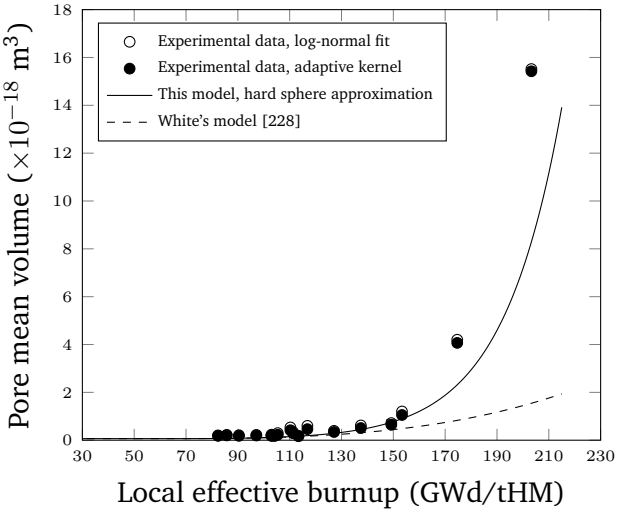

Figure 4.3.: Mean pore volume as a function of the local effective burnup. Circles: experimental values obtained in this work; solid line: model prediction using the hard sphere approximation (Section 4.3); dashed line: model prediction using White's approximation for pore coalescence [228].

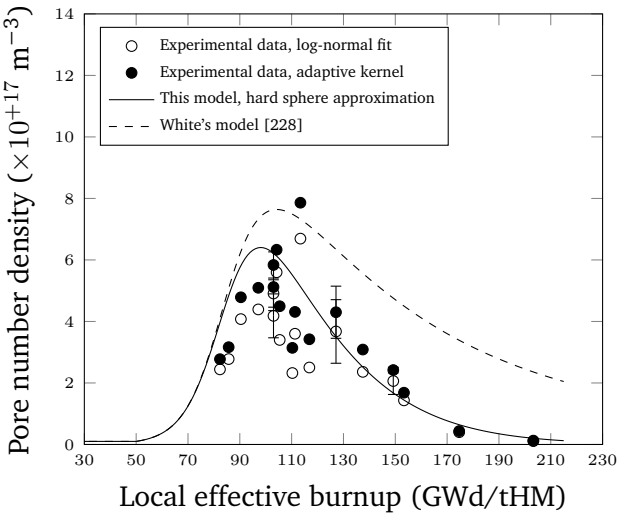

Figure 4.4.: Pore number density as a function of the local effective burnup. Circles: experimental values obtained in this work; solid line: model prediction using the hard sphere approximation (Section 4.3); dashed line: model prediction using White's approximation for pore coalescence [228].

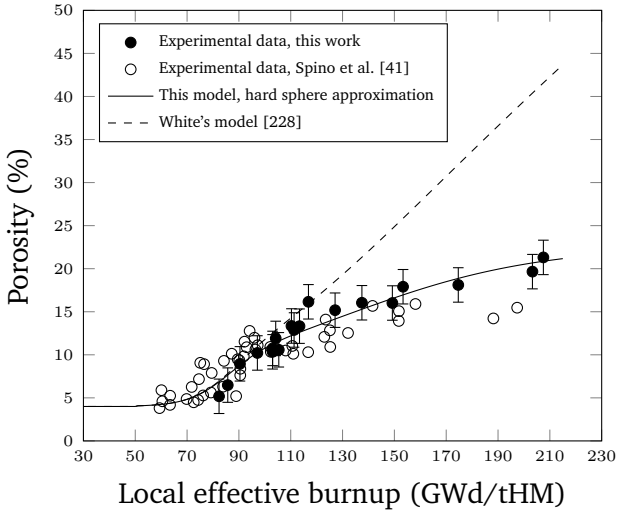

Figure 4.5.: Total porosity as a function of the local effective burnup. Filled circles: experimental values obtained in this work; open circles: experimental values according to Spino et al. [41]; solid line: model prediction using the hard sphere approximation (Section 4.3); dashed line: model prediction using White's approximation for pore coalescence [228].

$$\left.\frac{dN_v}{N_v}\right|_c \approx -\frac{1}{2}\left\{8\frac{4\pi}{3}N_v\left[(R_p+dR_p)^3-R_p^3\right]\right\} \tag{4.14}$$

Neglecting the quadratic and cubic terms in dR_p in Eq. (4.14), White's approximation for the pore coalescence is recovered, namely

$$dN_v|_c \approx -4N_v^2 dV_p \tag{4.15}$$

The better agreement with the experimental data observed when using the hard sphere approximation depends on the substantially different functional form of the nearest-neighbour density function in the two cases (see Fig. D.2). In the case of the hard spheres approximation, which accounts for the excluded volume of each pore, $H_p(x)$ attains a much higher maximum at contact, resulting in faster coalescence when compared to the case of overlapping spheres (Fig. 4.4). The faster coalescence results in enhanced increase of the mean pore volume, due to the conservation of the parent pores volumes [238] (Fig. 4.3). In Fig. 4.5 the predicted porosity increase, calculated as in Eq. (4.4), is reported against the experimental results obtained in this work and in [41]. The model correctly predicts the rate variation of porosity increase experimentally observed above 100 GWd/tHM, without introducing any enhancement in the vacancy diffusion coefficient or precipitation rate.

5. Conclusions and recommendations for future work

> "Begin at the beginning," the King said, very gravely, "and go on till you come to the end: then stop."
>
> *Alice in Wonderland*

5.1. Summary and main achievements

Specific experimental investigations have been carried out to study the high burnup fuel mechanical properties and the local microstructure, in particular the porosity. It has to be mentioned that the experimental investigations of such heavily irradiated materials is very time-consuming and often limited by the fact that the handling has to be carried out remotely via telemanipulators. In particular, experimental limitations in the measurements of the fuel Young's modulus have been encountered, given the difficult and limited applicability of the technique to the pellet periphery. A new approach has been implemented, exploiting the synergy between PIE techniques, namely the acoustic microscopy and the Vickers microindentation.

The ratio between the Young's modulus and the Vickers microhardness was found constant over a large range of burnups and porosity, suggesting that the Young's modulus dependence on porosity in high burnup fuel, in particular in the HBS, could be estimated via the microhardness measurements. The data, in combination with Young's modulus data of irradiated UO_2 available in literature, were used for the first time to introduce a new correlation for the Young's modulus of irradiated UO_2 fuel that exhibits better agreement with the experimental results. The range of experimental validation of the TRANSURANUS code correlation for the fuel Young's modulus was thus extended from non-irradiated to irradiated UO_2 fuel and to porosity up to 20%.

Advanced image analysis techniques, e.g. the adaptive kernel estimator and measurements of the two-point correlation functions, have been introduced to analyse the evolution of the pore size distribution and related moments along the radius of the samples here investigated, in particular in the HBS and ultra-high HBS. The introduction of the adaptive kernel estimator to determine the pore size distribution provides advantages and accuracy improvements in comparison to the methodology implemented so far. It

is flexible because it relies on a non-parametric approach, allowing the description of multi-modal distributions; therefore, it can be employed for the investigations of the pore size distribution in various types of fuel, for instance the MIMAS MOX, which typically show different porosities in the Pu-islands and in the UO_2 matrix.

The new methodology has been applied to characterise the radial profile of the porosity in samples with average burnup in the range of the "pulverisation threshold" (i.e. 60-70 GWd/tHM) during LOCA-type of transients. A high density of intergranular porosity along the pellet radius has been widely reported, but the porosity and related characteristics in such fuel regions have not been precisely quantified previously. Values of porosity and pore density comparable to the values generally measured at the fuel pellet radial periphery, characterised by pores with faceted appearance like those in the pellet periphery, have been measured outside the "traditional" rim. Discussions are on-going concerning the role played by the fuel microstructure configurations, particularly the density of closed bubbles at various radial locations, on the fragmentation of the fuel during accidents. The present data could support further development and refinements of dedicated models.

Observations of the grain morphology on a natural cavity and fresh fracture surfaces in a sample with 80 GWd/tHM average have revealed rounded sub-grains formation through most of the pellet radius (up to relative radial positions $r/r_0 \approx 0.3$), confirming the role of free surfaces as preferential locations for grain subdivision. Outside the rim, where the fission density can be considered approximately constant along the fuel radius, the process of subdivision appears more pronounced on the colder zones of the pellet, confirming that the phenomenon could be associated to accumulation and re-organisation of defects by radiation-enhanced surface diffusion along the original intergranular planes, partially inhibited by thermal recovery in the hotter zones. The extent of similarities between the HBS and this type of restructuring process is still not fully ascertained.

The study of the evolution of the pore density and pore mean diameter as a function of the local burnup has shown that, upon reaching a critical burnup threshold equal to ≈100 GWd/tHM, pore coarsening occurs, confirming a previous investigation. The observations suggest that a pore coalescence mechanism due to contact between growing pores is active.

The experimental results have been complemented by simple modelling, in order to verify whether the supposed mechanism could be consistent. A new model for pore coarsening has been introduced, assuming that the pores in the HBS can be modelled as a system of random monodisperse hard spheres in a matrix. The model is part of a more general model aimed at describing semi-empirically the xenon depletion and porosity growth in the HBS. The model correctly predicts the trends observed in the data, leverages on physics-based phenomena while introducing a limited amount of parameters. The mechanisms are kept as simple as possible, in order to contain the computational cost for its possible integration in fuel performance codes.

Finally, a first ageing study focussed on high burnup fuel microhardness has been performed. Within the limited number of SNF samples and dpa values that could be investigated, the present results show that the fuel microhardness does not significantly increase when the dose due to the additional decay damage accumulated during storage

reaches ≈0.1 dpa, in agreement with what was observed on ^{238}Pu-doped analogues. The analysis of SNF hardening and the comparison with the microhardness of ^{238}Pu-doped samples, first of its kind, provides a valuable contribution to the validation process of accelerated ageing condition studies using the α-doped samples. These studies are used as predictors of the SNF property evolution during extended storage.

5.2. Recommendations for future work

In the framework of the experimental investigations of the high burnup fuel mechanical properties, it is recommended to complement the available experimental techniques with additional PIE tools. For instance, installation of a shielded dynamic nano-indenter could offer the possibility of direct investigation of the relationship between the microhardness and Young's modulus in high burnup fuel, in order to provide validation and support to the measurements and observations here made. In addition, the technique could be a valid complement and alternative to the acoustic microscopy for Young's modulus measurements, avoiding technical problems like the one here experienced as a consequence of the degradation of the epoxy resin when in contact with the coupling liquid.

The high radioactivity of the samples was a major issue, limiting the number of experimental techniques that could be employed to study the characteristics of the local microstructure with a systematic approach. The possibility of miniaturising samples while keeping track of their original location in the fuel pellet, using for instance a Focused Ion Beam (FIB), will be a major improvement, opening up unprecedented possibilities in terms of adding and coupling experimental investigation capabilities on SNF.

Concerning the preliminary model about the fission gas behaviour, in particular the pore coarsening mechanism here introduced, it is clear that the model is still incomplete; however, the work here reported provides indications about the physical mechanisms that are causing the observed trends of gaseous swelling in the HBS. First step to be taken would be a sensitivity analysis of all the model parameters, in particular the diffusion coefficients, which are generally affected by the biggest uncertainty. It would be of extreme importance as it will serve as a further bolster of the modelling methodology. Furthermore, it would be advisable to integrate the model in a fuel performance code, in order to validate the model predictions against swelling and integral fission gas release data in a more comprehensive database than the one here presented.

With respect to the part I have developed, I foresee a main direction for extension of the present coarsening model: introduction of fission gas release through open surfaces, whose presence due to cracking is natural. Pore venting impacts pore density and fission gas release and should be considered for a more realistic description of the porosity in the HBS. In particular, it is necessary to consider fission gas release mechanisms from the HBS if the model has to be extended to transient conditions. Further improvement would be brought by the introduction of a polydisperse size distribution, instead of the monodisperse distribution here considered.

Finally, regarding the ageing study, the results here presented are to be considered preliminary, since the analysis has been performed on two samples only, the ones available at the time this work was performed. Further investigations on samples with smaller accumulated dose would be advisable, in order to verify whether the kinetics of the SNF hardening due to decay damage accumulation is similar to that observed in the ^{238}Pu-doped samples.

A. Stereology and the Schwartz-Saltykov method

In the case of secondary phases dispersed in a matrix, a well-known problem is the so called "Wicksell's corpuscle problem" [242], i.e., the derivation of the 3D particle size distribution, starting from a measurement of 2D circular contours in the plane section. An established solution to the corpuscle problem was first advanced by Scheil and Schwartz and later modified by Saltykov. The original method has been proposed for estimating the size distribution of spherical grains whose centers are randomly distributed in the matrix, under the assumption that the largest 2D diameter measured (d_{max}) on the test plane corresponds to the true 3D sphere diameter of the largest particle in the distribution [144]. To avoid confusion, the measured 2D diameters are from now on called "sections", whereas the 3D diameters are called "diameters". Under the assumptions stated above, the measured 2D sections are split into N classes of width Δ

$$\Delta = \frac{d_{max}}{N} \tag{A.1}$$

A section in the class i (i.e., with 2D section in the range $d(i)$-Δ and $d(i)$) will appear either when a sphere with diameter $d(i)$ is intersected by the test plane on its diameter plane or when it is intersected on a different plane. The probability that a particle with diameter in the j class generates a section with diameter in the class i can be written as

$$B_{ij} = \begin{cases} \sqrt{j^2-(i-1)^2} - \sqrt{j^2-i^2}, & \text{if } i \leq j, \\ 0, & \text{if } i > j \end{cases} \tag{A.2}$$

Therefore, when counting the number of particles per unit volume in a certain class j ($N_v(j)$) from the number of particles in the unit area in the various classes ($N_a(j)$), it is necessary to subtract the number of particles in the bigger classes multiplied by the probability that they have generated a section in the class j.

The general formula for the number of particles in the unit volume in each class $N_v(j)$ can be expressed as [144],

$$N_v(j) = \frac{1}{\Delta} \sum_{i=j}^{N} \alpha_{ij} N_a(i) \qquad \text{for } j = 1...N \tag{A.3}$$

where the coefficients α_{ij} were generalised as follows [152]

$$\alpha_{ij} = \begin{cases} T_{ii}, & \text{if } i = j, \\ -\sum_{m=i}^{j-1} \alpha_{mi} T_{mj}, & \text{if } i < j \end{cases} \tag{A.4}$$

where T_{ij} are defined as [152]

$$T_{ij} = \begin{cases} \frac{1}{B_{jj}}, & \text{if } i = j, \\ \frac{B_{ij}}{B_{jj}}, & \text{if } i < j \end{cases} \tag{A.5}$$

The original coefficients α_{ij} were limited to 15 [144], but they have been extended to an arbitrary number of classes.

B. The kernel estimator

The kernel estimator is a non-parametric statistical method used for estimating density functions from a set of data when the underlying distribution is unknown [243]. A non-negative kernel function $K(x) : \mathbb{R} \to \mathbb{R}_0^+$ is any function which satisfies the condition

$$\int_{-\infty}^{+\infty} K(x)dx = 1 \tag{B.1}$$

Usually, the kernel K is a symmetric probability density function, for example the standard normal distribution. The kernel density estimator with kernel K is defined by [244]

$$\hat{f}(x) = \frac{1}{nh} \sum_{i=1}^{n} K\left(\frac{x - X_i}{h}\right) \tag{B.2}$$

where h is the smoothing parameter or (fixed) bandwidth, which is a positive, non-random number and n is the total number of data $X_i ... X_n$. Considering (B.2), the kernel density estimator can be thought of as a sum of "bumps" placed at the observations, which are then summed together to give a composite curve that estimates the data distribution (see Fig. B.1). The width of "bumps" is determined by the smoothing parameter h [244].

The adaptive kernel estimator is similar to the kernel estimator, but allows the smoothing parameter to vary across the data point, using broader kernel in regions of low density. It is advantageous when dealing with long-tailed distributions [245].

Starting from a pilot estimate of the density $\hat{f}(x)$ with fixed bandwidth, the local bandwidth factors are defined as

$$\lambda_i = \left(\frac{\hat{f}(X_i)}{g}\right)^{-\alpha} \tag{B.3}$$

where g is [245]

$$\log g = n^{-1} \sum \log \hat{f}(X_i) \tag{B.4}$$

and α is the sensitivity parameter, which varies between 0 and 1. Generally, α is set to 0.5 [245].

The adaptive kernel estimator is defined as

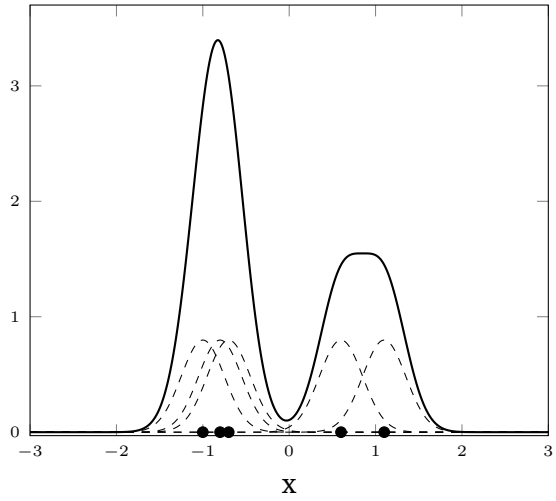

Figure B.1.: Univariate kernel density estimate example using a Gaussian kernel function. Solid line: kernel density estimate. Dashed lines: individual kernels centred on the data.

$$\tilde{f}(x) = \frac{1}{n}\sum_{i=1}^{n} h^{-1}{\lambda_i}^{-1} K\left(\frac{x - X_i}{h\lambda_i}\right) \tag{B.5}$$

where the symbols have the same meaning as in Eqs. (B.2) and (B.3).

The advantage of using a kernel instead of the histogram is double. First of all, using the kernel estimator, a continuous estimation of the density is obtained. Second of all, since the kernel function are placed at the position of the data points, the resulting shape of the density estimate is not influenced by the bin placement as it happens for the histogram. The kernel estimator depends only on one parameter, the smoothing parameter h, which influences the global accuracy of $\hat{f}(x)$ as an estimator of the true density $f(x)$. The mean integrated square error (MISE) is defined as

$$\text{MISE}(\hat{f}) = E\int \left(\hat{f}(x) - f(x)\right)^2 dx \tag{B.6}$$

where E indicates the expected value, $\hat{f}(x)$ the density estimation, $f(x)$ the true (unknown) density. If the MISE is taken as a measure of the global accuracy of $\hat{f}(x)$ as an estimator of the true density $f(x)$, then the optimal bandwidth h_{opt} is the value of h which minimise the MISE. Silverman showed that, taking into consideration some simple approximations in evaluating the MISE, the optimal bandwidth h_{opt} is proportional to the second derivative of the unknown true density [149], therefore, not determinable. Several authors have proposed different methods to estimate the optimal bandwidth.

To evaluate the pilot estimator with fixed smoothing parameter several methods are available in literature (see the review from Cao et al. [246]). In this particular case,

the Smoothed Cross Validation (SCV) method [247] was applied. The method is an automatic, data-driven optimisation technique based on the estimation of the mean integrated square error (MISE) [246]. The score function evaluation was included in the algorithm for the calculation of the pore distributions (see Section 2.4.3) using the algorithms implemented in the WAFO toolbox [248]. The values of h in which the optimisation was performed were chosen based on the data [149]

$$0.25n^{-0.2}\sigma < h < 1.25n^{-0.2}\sigma \tag{B.7}$$

where σ is the standard deviation of the data and n the number of data. If the convergence was reached below the pixel resolution limit, which influence the level of discretization of the data, the smoothing parameter was assumed equal to the resolution limit (examples in Fig. B.2). As being the parameter that pilots the amplitude of the kernels placed at each data point, h should not be smaller than the sampling resolution of the data, which in this case can be considered the minimum of the pixel spatial resolution. The approach is justify by the necessity of reducing the variance of the estimator. In fact, the MISE can be expressed as follows [149, 246],

$$MISE(\hat{f}) = \int \{E\hat{f}(x) - f(x)\}^2 dx + \int var\hat{f}(x)dx \tag{B.8}$$

where $E\hat{f}(x)$ is the expected value of the kernel estimator $\hat{f}(x)$ and $var\hat{f}(x)$ its variance. The term $\{E\hat{f}(x) - f(x)\}^2$ is the squared bias of the estimator. Following some approximations [149, 246] the two terms can be expressed as,

$$\int \{E\hat{f}(x) - f(x)\}^2 dx \approx \frac{1}{4}h^4 {k_2}^2 \int f''(x)^2 dx \tag{B.9}$$

where k_2 is

$$k_2 = \int x^2 K(x)dx \tag{B.10}$$

and f'' is the second derivative of the unknown density. Eq. (B.9) shows that the bias is proportional to h. Instead, the integrated variance can be expressed as

$$\int var\hat{f}(x)dx \approx \frac{1}{nh} \int K(x)^2 dx \tag{B.11}$$

showing how the variance is inversely proportional to h. If h is reduced in order to reduce the bias, the integrated variance become larger. Setting a lower limit to h consistent with the experimental limitations (i.e., the pixel resolution) is a trade-off in the estimation process.

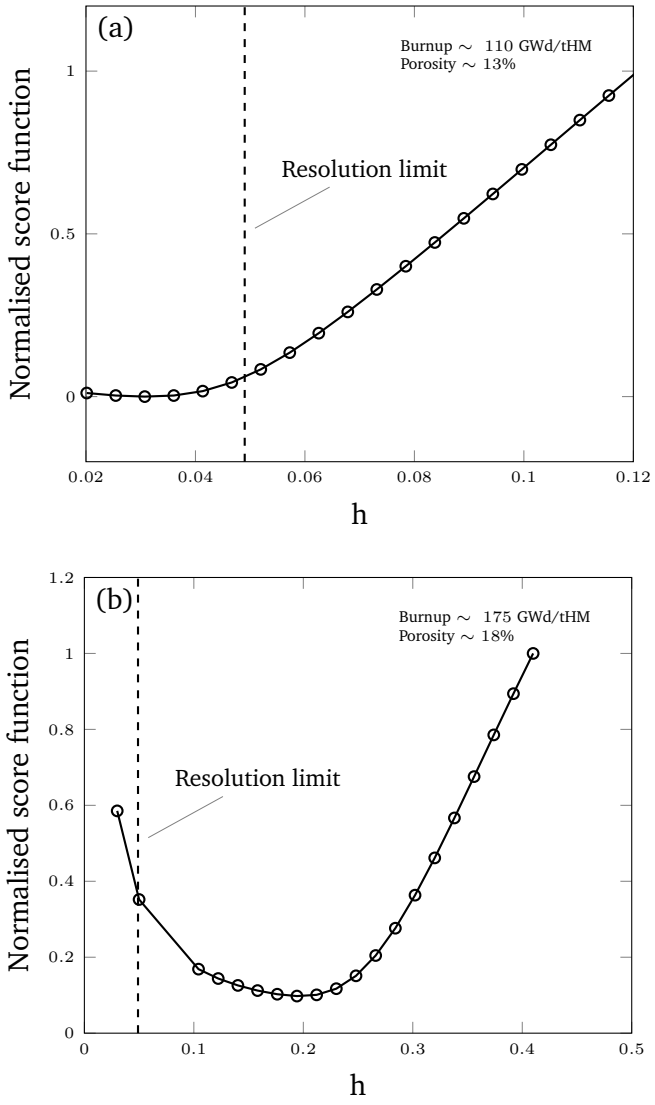

Figure B.2.: Optimization of the smoothing parameter for the sample at local burnup (a) 110 GWd/tHM; (b) 175 GWd/tHM.

C. Root finding

A root-finding algorithm is a numerical method, or algorithm, for finding a value x such that

$$f(x) = 0 \tag{C.1}$$

For non-linear functions, the solution of Eq. (C.1) proceeds iteratively. Some approximate trial solution has to be provided. The trial solution is used as input for the algorithm that has to improve the solution until some predetermined convergence criterion is satisfied. The initial trial solution is crucial in determining the success of convergence. A bad choice of the initial trial solution can result in divergence or cyclic behaviour.

Several numerical procedures can be employed in root finding. Here I summarise two methods that have been employed in this work: bisection and Newton-Raphson method.

C.1. Bisection method

The bisection method is the simplest and most robust algorithm for finding the root of a one-dimensional, continuous function $f(x)$ on a closed interval. In case of continuous functions, the intermediate value theorem states that, if in an interval $[a, b]$ $f(a)$ and $f(b)$ have opposite signs, there exists at least one value $r \in [a, b]$ such that $f(r) = 0$. The method makes use of this theorem iteratively. First, the function at the interval's midpoint is evaluated and its sign examined. The limit with the same sign is replaced by the midpoint so that after each iteration the interval length containing the root decreases by a factor of two. This process continues until the width of the interval shrinks below some predetermined error tolerance. The method converges linearly to the solution. The number of iteration required to achieve a given tolerance is

$$n = \log_2 \frac{\epsilon_0}{\epsilon} \tag{C.2}$$

where ϵ_0 is the size of the initially bracketing interval, ϵ is the desired ending tolerance.

C.2. Newton-Raphson method with derivatives

The method is based on the simple idea of linear approximation of a function. Starting from an estimation x_0 of the root r so that $r = x_0 + h$, where h is a measure of how far the estimation x_0 is far from the root r. If h is "small", $f(r)$ can be linearly approximate in Taylor's expansion

$$f(r) = f(x_0 + h) \approx f(x_0) + hf'(x_0) \tag{C.3}$$

and thus

$$h \approx -\frac{f(x_0)}{f'(x_0)} \tag{C.4}$$

from which it follows

$$r \approx x_0 - \frac{f(x_0)}{f'(x_0)} \tag{C.5}$$

The new estimate is therefore $x_1 = x_0 - \dfrac{f(x_0)}{f'(x_0)}$. The next estimate can b obtained in the same manner. If x_n is the current estimates, the estimate at the $n+1$-iteration is simply

$$x_{n+1} = x_n - \frac{f(x_n)}{f'(x_n)} \tag{C.6}$$

The attractive property of the Newton-Raphson method is its quadratic convergence rate. Let's consider two estimate to the root, x_i and x_{i+1} differ from the true root by ϵ_i and ϵ_{i+1}, respectively:

$$x_i = r - \epsilon_i \tag{C.7}$$

$$x_{i+1} = r - \epsilon_{i+1} \tag{C.8}$$

By substituting Eqs. (C.7) and (C.8) in Eq. (C.6) one obtains

$$\epsilon_{i+1} = \epsilon_i - \frac{f(r - \epsilon_i)}{f'(r - \epsilon_i)} \tag{C.9}$$

If the functions $f(r - \epsilon_i)$ and $f'(r - \epsilon_i)$ are expandend in Taylor's series the quadratic convergence rate is obtained,

$$\epsilon_{i+1} = \epsilon_i^2 \frac{f''(x)}{2\, f'(x)} \tag{C.10}$$

D. Nearest-neighbour statistics of monodisperse spheres

Given a system of monodisperse particles with diameter σ and number density ρ, the nearest-neighbour distribution function $H_p(r)$ is defined as the probability density associated with finding a nearest neighbour particle at some radial distance r from a reference particle (Fig. D.1) [196, 249].

Defining x as the normalised distance $x = r/\sigma$, for a system of fully-penetrable spheres $H_p(x)$ is [234]

$$H_p(x) = 24\phi x^2 \exp(-8\phi x^3) \tag{D.1}$$

where ϕ is the particle volume fraction, i.e.,

$$\phi = \frac{\pi}{6}\rho\sigma^3 \tag{D.2}$$

For a system of hard-spheres $H_p(x)$ is calculated as follows [196]

$$H_p(x) = 24\phi(a_0 x^2 + a_1 x + a_2)\exp(-\phi[8a_0(x^3-1) + 12a_1(x^2-1) + 24a_2(x-1)]) \tag{D.3}$$

The three factors a_0, a_1 and a_2 can be written as [196]

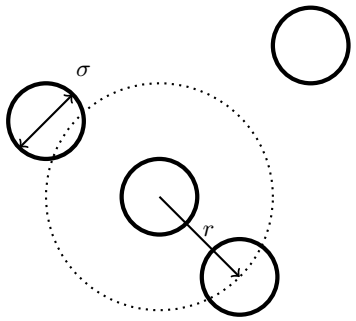

Figure D.1.: Schematic representations of a system of randomly distributed monodisperse particles with diameter σ.

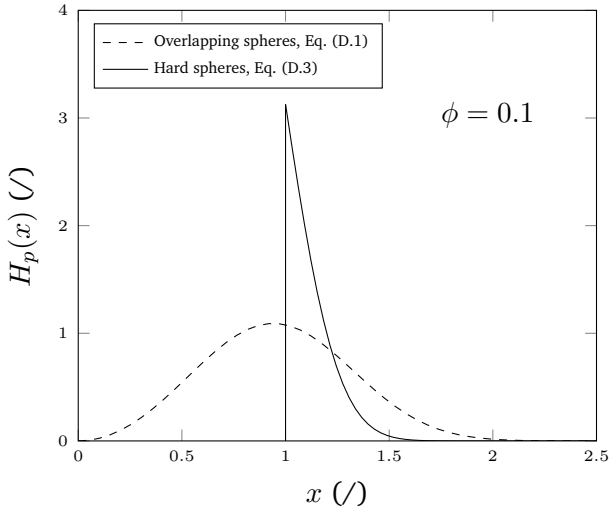

Figure D.2.: Nearest-neighbour distribution functions for monodisperse system of overlapping spheres (dashed line) and hard spheres (solid line) at a particle volume fraction $\phi = 0.1$.

$$a_0 = \frac{(1 + \phi + \phi^2 - \phi^3)}{(1 - \phi)^3} \tag{D.4}$$

$$a_1 = \frac{\phi(3\phi^2 - 4\phi - 3)}{2(1 - \phi)^3} \tag{D.5}$$

$$a_2 = \frac{\phi^2(2 - \phi)}{2(1 - \phi)^3} \tag{D.6}$$

Figure D.2 shows two examples of the nearest-neighbour distribution function $H_p(x)$ for a system of overlapping spheres and of hard spheres at a particle volume fraction of $\phi = 0.1$.

E. Alpha-emitters inventory calculations

The tables report the inventory of the main α-emitters in PWR SNF with average burnup 80 GWd/tHM and 102 GWd/tHM at EOL. The calculations performed with webKORIGEN were bechmarked against the calculated inventory using the code SERPENT [160], taken as reference.

Table E.1.: Calculated concentrations of the main α-emitters in PWR SNF with average burnup 80 GWd/tHM at the EOL.

Nuclide	webKORIGEN Concentration ($g\,g^{-1}$ U)	SERPENT Concentration ($g\,g^{-1}$ U)	Difference(%)
^{232}U	$3.10 \cdot 10^{-9}$	$2.17 \cdot 10^{-11}$	14185
^{233}U	$1.50 \cdot 10^{-9}$	$1.27 \cdot 10^{-9}$	18.27
^{234}U	$7.20 \cdot 10^{-5}$	$1.65 \cdot 10^{-5}$	335.72
^{236}U	$4.40 \cdot 10^{-3}$	$5.12 \cdot 10^{-3}$	-13.98
^{238}U	$8.90 \cdot 10^{-1}$	$8.56 \cdot 10^{-1}$	3.93
^{239}U[1]	$7.90 \cdot 10^{-7}$	$9.25 \cdot 10^{-7}$	-14.61
^{237}Np	$1.20 \cdot 10^{-3}$	$1.25 \cdot 10^{-3}$	-4.35
^{238}Np[1]	$5.00 \cdot 10^{-6}$	$4.57 \cdot 10^{-6}$	9.52
^{239}Np[1]	$1.10 \cdot 10^{-4}$	$1.33 \cdot 10^{-4}$	-17.50
^{240}Np[1]	$3.30 \cdot 10^{-9}$	$6.86 \cdot 10^{-9}$	-51.90
^{236}Pu	$5.80 \cdot 10^{-9}$	$8.51 \cdot 10^{-11}$	6712.23
^{238}Pu	$9.50 \cdot 10^{-4}$	$1.32 \cdot 10^{-3}$	-28.71
^{239}Pu	$7.90 \cdot 10^{-3}$	$1.60 \cdot 10^{-2}$	-50.77
^{240}Pu	$5.90 \cdot 10^{-3}$	$5.26 \cdot 10^{-3}$	12.07
^{241}Pu	$2.10 \cdot 10^{-3}$	$4.05 \cdot 10^{-3}$	-48.14
^{242}Pu	$1.40 \cdot 10^{-3}$	$1.52 \cdot 10^{-3}$	-7.67
^{243}Pu[1]	$4.9 \cdot 10^{-7}$	$5.10 \cdot 10^{-7}$	-3.87
^{244}Pu	$5.40 \cdot 10^{-7}$	$5.88 \cdot 10^{-7}$	-8.22
^{241}Am	$6.80 \cdot 10^{-5}$	$1.70 \cdot 10^{-4}$	-61.87
^{242}Am	$1.90 \cdot 10^{-7}$	$3.71 \cdot 10^{-7}$	-48.80
^{242m}Am	$3.90 \cdot 10^{-6}$	$5.51 \cdot 10^{-6}$	-29.18

[1] β-emitter generating α-emitters in the decay chain.

Table E.1.: (continued)

Nuclide	webKORIGEN Concentration (g g^{-1} U)	SERPENT Concentration (g g^{-1} U)	Difference(%)
^{243}Am	$5.90 \cdot 10^{-4}$	$6.49 \cdot 10^{-4}$	-9.14
^{244}Am[1]	$3.80 \cdot 10^{-8}$	$3.99 \cdot 10^{-8}$	-4.28
^{244m}Am[1]	$3.10 \cdot 10^{-8}$	$3.26 \cdot 10^{-8}$	-5.00
^{242}Cm	$3.40 \cdot 10^{-5}$	$6.30 \cdot 10^{-5}$	-47.64
^{243}Cm	$2.10 \cdot 10^{-6}$	$3.91 \cdot 10^{-6}$	-46.25
^{244}Cm	$6.50 \cdot 10^{-4}$	$6.80 \cdot 10^{-4}$	-4.35
^{245}Cm	$4.70 \cdot 10^{-5}$	$1.58 \cdot 10^{-4}$	-70.27
^{246}Cm	$1.90 \cdot 10^{-5}$	$2.32 \cdot 10^{-5}$	-17.95
^{247}Cm	$5.30 \cdot 10^{-7}$	$1.15 \cdot 10^{-6}$	-53.84
^{248}Cm	$1.00 \cdot 10^{-7}$	$1.93 \cdot 10^{-7}$	-48.27
^{249}Cm[1]	$1.80 \cdot 10^{-12}$	$5.25 \cdot 10^{-12}$	-65.70
^{249}Bk	$1.80 \cdot 10^{-9}$	$8.25 \cdot 10^{-9}$	-78.18
^{250}Bk[1]	$2.90 \cdot 10^{-12}$	$7.17 \cdot 10^{-12}$	-59.55
^{248}Cf	$8.40 \cdot 10^{-10}$	$8.90 \cdot 10^{-15}$	$9.44 \cdot 10^{6}$
^{249}Cf	$3.50 \cdot 10^{-10}$	$2.24 \cdot 10^{-9}$	-84.34
^{250}Cf	$4.70 \cdot 10^{-10}$	$4.77 \cdot 10^{-9}$	-90.14
^{251}Cf	$2.70 \cdot 10^{-10}$	$1.40 \cdot 10^{-9}$	-80.70
^{252}Cf	$4.30 \cdot 10^{-10}$	$8.79 \cdot 10^{-10}$	-51.10
^{253}Cf[1]	$9.50 \cdot 10^{-13}$	$1.92 \cdot 10^{-12}$	-52.12

Table E.2.: Calculated concentrations of the main α-emitters in PWR SNF with average burnup 102 GWd/tHM at the EOL.

Nuclide	webKORIGEN Concentration (g g^{-1} U)	SERPENT Concentration (g g^{-1} U)	Difference(%)
^{232}U	$3.90 \cdot 10^{-9}$	$2.28 \cdot 10^{-11}$	16988
^{233}U	$1.40 \cdot 10^{-9}$	$7.51 \cdot 10^{-10}$	86.31
^{234}U	$5.10 \cdot 10^{-5}$	$1.61 \cdot 10^{-5}$	217.11
^{236}U	$3.20 \cdot 10^{-3}$	$4.40 \cdot 10^{-3}$	-27.21
^{238}U	$8.70 \cdot 10^{-1}$	$8.23 \cdot 10^{-1}$	5.71
^{239}U[1]	$7.60 \cdot 10^{-7}$	$8.16 \cdot 10^{-7}$	-7.19
^{237}Np	$1.10 \cdot 10^{-3}$	$1.04 \cdot 10^{-3}$	5.90
^{238}Np[1]	$4.40 \cdot 10^{-6}$	$4.29 \cdot 10^{-6}$	2.45
^{239}Np[1]	$1.10 \cdot 10^{-4}$	$1.18 \cdot 10^{-4}$	-6.81
^{240}Np[1]	$3.10 \cdot 10^{-9}$	$5.78 \cdot 10^{-9}$	-46.34

[1] β-emitter generating α-emitters in the decay chain.

Table E.2.: (continued)

Nuclide	webKORIGEN Concentration ($g\,g^{-1}$ U)	SERPENT Concentration ($g\,g^{-1}$ U)	Difference(%)
^{236}Pu	$6.20 \cdot 10^{-9}$	$7.80 \cdot 10^{-11}$	7844.74
^{238}Pu	$1.10 \cdot 10^{-3}$	$1.09 \cdot 10^{-3}$	0.88
^{239}Pu	$7.80 \cdot 10^{-3}$	$7.04 \cdot 10^{-3}$	10.77
^{240}Pu	$6.50 \cdot 10^{-3}$	$3.91 \cdot 10^{-3}$	66.15
^{241}Pu	$2.50 \cdot 10^{-3}$	$2.47 \cdot 10^{-3}$	1.14
^{242}Pu	$1.80 \cdot 10^{-3}$	$2.40 \cdot 10^{-3}$	-25.14
^{243}Pu[1]	$6.40 \cdot 10^{-7}$	$6.78 \cdot 10^{-7}$	-5.56
^{244}Pu	$1.10 \cdot 10^{-6}$	$9.85 \cdot 10^{-7}$	11.72
^{241}Am	$9.80 \cdot 10^{-5}$	$7.61 \cdot 10^{-5}$	28.70
^{242}Am	$2.30 \cdot 10^{-7}$	$2.67 \cdot 10^{-7}$	-13.75
^{242m}Am	$4.70 \cdot 10^{-6}$	$1.61 \cdot 10^{-6}$	191.77
^{243}Am	$8.50 \cdot 10^{-4}$	$9.37 \cdot 10^{-4}$	-9.25
^{244}Am[1]	$5.40 \cdot 10^{-8}$	$5.62 \cdot 10^{-8}$	-3.85
^{244m}Am[1]	$4.40 \cdot 10^{-8}$	$4.60 \cdot 10^{-8}$	-4.36
^{242}Cm	$4.00 \cdot 10^{-5}$	$4.95 \cdot 10^{-5}$	-19.20
^{243}Cm	$2.70 \cdot 10^{-6}$	$2.48 \cdot 10^{-6}$	8.80
^{244}Cm	$1.30 \cdot 10^{-3}$	$1.09 \cdot 10^{-3}$	19.26
^{245}Cm	$9.80 \cdot 10^{-5}$	$1.45 \cdot 10^{-4}$	-32.24
^{246}Cm	$6.10 \cdot 10^{-5}$	$5.46 \cdot 10^{-5}$	11.74
^{247}Cm	$2.30 \cdot 10^{-6}$	$2.51 \cdot 10^{-6}$	-8.24
^{248}Cm	$6.60 \cdot 10^{-7}$	$5.62 \cdot 10^{-7}$	17.49
^{249}Cm[1]	$1.10 \cdot 10^{-11}$	$1.27 \cdot 10^{-11}$	-13.90
^{249}Bk	$1.20 \cdot 10^{-8}$	$1.33 \cdot 10^{-8}$	-9.85
^{250}Bk[1]	$2.00 \cdot 10^{-11}$	$2.58 \cdot 10^{-11}$	-22.61
^{248}Cf	$8.20 \cdot 10^{-9}$	$1.26 \cdot 10^{-14}$	$6.53 \cdot 10^{7}$
^{249}Cf	$2.90 \cdot 10^{-9}$	$2.93 \cdot 10^{-9}$	-0.98
^{250}Cf	$3.50 \cdot 10^{-9}$	$1.32 \cdot 10^{-8}$	-73.40
^{251}Cf	$2.10 \cdot 10^{-9}$	$3.89 \cdot 10^{-9}$	-45.98
^{252}Cf	$4.70 \cdot 10^{-9}$	$6.35 \cdot 10^{-9}$	-25-95
^{253}Cf[1]	$1.10 \cdot 10^{-11}$	$1.46 \cdot 10^{-11}$	-24.61

References

[1] International Atomic Energy Agency. Impact of high burnup uranium oxide and mixed uranium-plutonium oxide water reactor fuel on spent fuel management. Technical Report ISSN 1995-7807 NF-T-3.8, IAEA, 2011.

[2] Nuclear Energy Agency. Very high burn-ups in light water reactors. Technical Report NEA No. 6224, OECD-NEA, 2006.

[3] P. Rudling, R. Adamson, B. Cox, F. Garzarolli, and A. Strassers. High burnup fuel issues. *Nucl. Eng. Technol.*, 40:1–8, 2008.

[4] R. Manzel and M. Coquerelle. Fission gas release and pellet structure at extended burnup. In *International Topical Meeting on LWR fuel performance*, pages 463–470, Portland, Oregon, 1997. ANS.

[5] J. Noirot, I. Aubrun, L. Desgranges, K. Hanifi, J. Lamontagne, B. Pasquet, C. Valot, P. Blanpain, and H. Cognon. High burnup changes in UO_2 fuels irradiated up to 83 GWd/tHM in M5®claddings. In *Water Reactor Fuel Performance Meeting*, pages 131–149, Seoul, Korea, 2008.

[6] Hj. Matzke. Radiation effects in nuclear fuels. In K.E. Sickafus, E.A. Kotomin, and B.P. Uberuaga, editors, *Radiation effects in solids*, chapter 14, pages 401–420. Springer, 2007.

[7] Hj. Matzke. Radiation damage in crystalline insulators, oxides and ceramic nuclear fuels. *Radiat. Eff. Defects Solids*, 64:3–33, 1982.

[8] Hj. Matzke. Radiation damage effects in nuclear materials. *Nucl. Instrum. Meth. B*, 32:455–470, 1988.

[9] T. Wiss. Radiation effects in UO_2. In R.J.M. Konings, editor, *Comprehensive nuclear materials*, volume 2, chapter 18, pages 465–480. 2010.

[10] J. Soullard and A. Alamo. Etude du ralentissement des ions dans une cible diatomique. *Radiat. Eff. Defects Solids*, 38:133–139, 1978.

[11] D. Baron, M. Kinoshita, P. Thevenin, and R. Largenton. Discussion about the HBS transformation in high burn-up fuels. *Nucl. Eng. Technol.*, 41:199–214, 2009.

[12] D.R. Olander. *Fundamental aspects of nuclear reactor fuel elements*, chapter 17. Radiation damage, page 373. Technical Information Center, Office of Public Affairs Energy Research and Development Administration, 1st edition, 1976.

[13] P. Blair. *Modelling of Fission Gas Behaviour in High Burnup Nuclear Fuel*. PhD thesis, École Polytechnique Fédérale de Lausanne, 2008.

[14] J.O. Barner, M.E. Cunningham, M.D. Freshley, and D.D. Lanning. High Burnup Effects Program - Final Report. Technical Report DOE/NE/34046-1. HBEP-61(3P27), Battelle Pacific Northwest Laboratories, 1990.

[15] J. Spino, D. Papaioannou, and I. Ray. Rim formation and fission gas behaviour: some structure remarks. In *Fission gas behaviour in light water reactor fuels*, pages 247–268, Cadarache, France, 2000.

[16] K. Une, K. Nogita, Y. Suzawa, K. Hayashi, K. Ito, and Y. Etoh. High burnup rim project(III). Properties of the rim-structured fuel. In *International Topical Meeting on LWR fuel performance*, pages 615–625, Park City, Utah, 2000. ANS.

[17] M. Kinoshita, T. Sonoda, S. Kitajima, A. Sasahara, T. Kameyama, T. Matsumura, E. Kolstad, V.V. Rondinella, C. Ronchi, J.-P. Hiernaut, T. Wiss, F. Kinnart, J. Ejton, D. Papaioannou, and Hj. Matzke. High Burnup Rim Project(III). Properties of the rim-structured fuel. In *International Topical Meeting on LWR fuel performance*, page 1102, Orlando, Florida, 2004. ANS.

[18] X.-M. Bai, M. R. Tonks, Y. Zhang, and J. D. Hales. Multiscale modeling of thermal conductivity of high burnup structures in UO_2 fuels. *J. Nucl. Mater.*, 470:208–215, 2016.

[19] International Atomic Energy Agency. Spent fuel performance assessment and research. Technical Report IAEA-TECDOC-1771, IAEA, 2015.

[20] EPRI Inc. Extended storage collaboration program international subcommittee report. Technical Report 1026481, EPRI, 2012.

[21] J.R. Lamarsh. chapter 2. Interaction of neutron with matter, pages 38–39. Addison-Wesley Publishing Company, 1961.

[22] V.V. Rondinella and T. Wiss. The high burn-up structure in nuclear fuel. *Materials Today*, 13:24–32, 2010.

[23] Hj. Matzke. On the rim effect in high burnup UO_2 LWR fuels. *J. Nucl. Mater.*, 189:141–148, 1992.

[24] J. Belle, editor. chapter 9. Irradiation effects in uranium dioxide, pages 552–565. Naval Reactors Physics Handbook. U.S. Government Printing Office, 1961.

[25] M.L. Bleiberg, R.M. Bernman, and B. Lustman. Effects of high burn-up on oxide ceramic fuels. In *Proceedings of the Symposium on Radiation Damage in Solids and Reactor Materials*, pages 319–428, Venice, Italy, 1962. IAEA.

[26] W.K. Barney and B.D. Wemple. Metallography of UO_2-containing fuel elements. Technical Report KAPL-1836, Knolls Atomic Power Laboratory, 1958.

[27] K. Lassmann, C.T. Walker, J. van de Laar, and F. Lindström. Modeling the high burnup UO_2 structure in LWR fuel. *J. Nucl. Mater.*, 226:1–8, 1995.

[28] S.R. Pati, A.M. Garde, and L.J. Clink. Contribution of pellet rim porosity to low-temperature fission gas release at extended burnups. In *International Topical Meeting on LWR fuel performance*, Williamsburg, Virginia, 1988. ANS.

[29] M.E. Cunningham, M.D. Freshley, and D.D. Lanning. Development and characteristics of the rim region in high burnup UO_2 fuel pellets. *J. Nucl. Mater.*, 188:19–27, 1992.

[30] D. Baron. Abnormal porosity buildup in the fuel periphery at high burn-up. In *HBEP Steering Committee Meeting*, Wengen, Switzerland, 1986.

[31] M. Kinoshita, T. Sonoda, S. Kitajima, A. Sasahara, E. Kolstad, Hj. Matzke, V.V. Rondinella, A.D. Stalios, C.T. Walker, I.L.F. Ray, M. Sheindlin, D. Halton, and C. Ronchi. High Burnup Rim Project (II) Irradiation and Examination to investigate rim-structured fuels. In *International Topical Meeting on LWR fuel performance*, Park City, Utah, 2000. ANS.

[32] T. Sonoda, M. Kinoshita, I.L.F. Ray, T. Wiss, H. Thiele, D. Pellottiero, V.V. Rondinella, and Hj. Matzke. Transmission electron microscopy observation on irradiation-induced microstructural evolution in high burn-up UO_2 disk fuel. *Nucl. Instrum. Meth. B*, 191:622–628, 2002.

[33] M. Kinoshita, T. Kameyama, S. Kitajima, and Hj. Matzke. Temperature and fission rate effects on the rim structure formation in a UO_2 fuel with a burnup of 7.9% FIMA. *J. Nucl. Mater.*, 252:71–78, 1998.

[34] S. K. Yagnik, T. Tverberg, E. Kolstad, J. A. Turnbull, D. Baron, and M. Kinoshita. Fuel (UO_2) R&D: Needs, approaches and results. In *Water Reactor Fuel Performance Meeting*, Seoul, Republic of Korea, 2008.

[35] C.T. Walker, T. Kameyama, S. Kitajima, and M. Kinoshita. Concerning the microstructure changes that occur at the surface of UO_2 pellets on irradiation to high burnup. *J. Nucl. Mater.*, 188:73–79, 1992.

[36] P. Van Uffelen, R.J.M. Konings, C. Vitanza, and J. Tulenko. Analysis of reactor fuel rod behavior. In D.G. Cacuci, editor, *Handbook of Nuclear Engineering*, volume III Reactor Analysis, chapter 13, pages 1582–1584. 2010.

[37] J. Spino, D. Baron, M. Coquerelle, and A.D. Stalios. High burn-up rim structure: evidences that xenon-depletion, pore formation and grain subdivision start at different local burn-ups. *J. Nucl. Mater.*, 256:189–196, 1998.

[38] J. Spino, K. Vennix, and M. Coquerelle. Detailed characterisation of the rim microstructure in PWR fuels in the burn-up range 40-67 GWd/tHM. *J. Nucl. Mater.*, 231:179–190, 1996.

[39] N. Lozano, L. Desgranges, D. Aymes, and J.C. Niepce. High magnification SEM observations for two types of granularity in a high burnup PWR fuel rim. *J. Nucl. Mater.*, 257:78–87, 1998.

[40] K. Nogita and K. Une. Radiation-induced microstructural change in high burnup UO_2 fuel pellets. *Nucl. Instrum. Meth. B*, 91:301–306, 1994.

[41] J. Spino, A.D. Stalios, H. Santa Cruz, and D. Baron. Stereological evolution of the rim structure in PWR-fuels at prolonged irradiation: Dependencies with burn-up and temperature. *J. Nucl. Mater.*, 354:66–84, 2006.

[42] J. Spino, J. Rest, W. Goll, and C.T. Walker. Matrix swelling rate and cavity volume balance of UO_2 fuels at high burn-up. *J. Nucl. Mater.*, 346:131–144, 2005.

[43] A. Romano, M. I. Horvath, and R. Restani. Evolution of porosity in the high-burnup fuel structure. *J. Nucl. Mater.*, 361:62–68, 2007.

[44] J.-P. Hiernaut, T. Wiss, J.-Y. Colle, H. Thiele, C.T. Walker, W. Goll, and R.J.M. Konings. Fission product release and microstructure changes during laboratory annealing of a very high burn-up fuel specimen. *J. Nucl. Mater.*, 377:313–324, 2008.

[45] Hj. Matzke and M. Kinoshita. Polygonization and high burnup structure in nuclear fuels. *J. Nucl. Mater.*, 247:108–115, 1997.

[46] R.D. Doherty. Primary recrystallization. In K.H.J. Buschow, R.W. Cahn, M.C. Flemings, B. Ilschner, E.J. Kramer, S. Mahajan, and P. Veyssiére, editors, *Encyclopedia of Materials: Science and Technology*, pages 7847–7850. Elsevier, second edition, 2001.

[47] R. Abbaschian, L. Abbaschian, and E. Reed-Hill. chapter 8. Annealing, pages 223–226. Cengage Learning, 4th edition, 2009.

[48] K. Nogita and K. Une. Irradiation-induced recrystallization in high burnup in UO_2 fuel. *J. Nucl. Mater.*, 226:302–310, 1995.

[49] K. Nogita and K. Une. High resolution TEM of high burnup UO_2 fuel. *J. Nucl. Mater.*, 250:244–249, 1997.

[50] K. Une, K. Nogita, T. Shiratori, and K. Hayashi. Rim structure formation of isothermally irradiated UO_2 fuel discs. *J. Nucl. Mater.*, 288:20–28, 2001.

[51] J. Rest and G.L. Hofman. Dynamics of irradiation-induced grain subdivision and swelling in U_3Si_2 and UO_2 fuels. *J. Nucl. Mater.*, 210:187–202, 1994.

[52] J. Rest and G.L. Hofman. An alternative explanation for evidence that xenon depletion, pore formation, and grain subdivision begin at different local burnups. *J. Nucl. Mater.*, 277:231–238, 2000.

[53] J. Rest. A model for the influence of microstructure, precipitate pinning and fission gas behavior on irradiation-induced recrystallization of nuclear fuels. *J. Nucl. Mater.*, 326:175–184, 2004.

[54] H. Xiao, C. Long, and H. Chen. Model for evolution of grain size in the rim region of high burnup UO_2 fuel. *J. Nucl. Mater.*, 471:74–79, 2016.

[55] M. Kinoshita. Towards the mathematical model of rim structure formation. *J. Nucl. Mater.*, 248:185–190, 1997.

[56] Hj. Matzke, A. Turos, and G. Linker. Polygonization of single crystals of the fluorite-type oxide UO_2 due to high dose ion implantation. *Nucl. Instrum. Meth. B*, 91:294–300, 1994.

[57] I.L.F. Ray, Hj. Matzke, H.A. Thiele, and M. Kinoshita. An electron microscopy study of the rim structure of a UO_2 fuel with a high burnup of 7.9% FIMA. *J. Nucl. Mater.*, 245:115–123, 1997.

[58] J. Jonnet, B. Remy, and P. Van Uffelen. Stress function determination for dislocation configurations obtained from kröner's theory. *Theor. Appl. Fract. Mech.*, 45:238–251, 2006.

[59] M.S. Veshchunov and V.E. Shestak. Model for evolution of crystal defects in UO_2 under irradiation up to high burn-ups. *J. Nucl. Mater.*, 384:12–18, 2009.

[60] V.G. Baranov, A.V. Lunev, A.V. Tenishev, and A.V. Khlunov. Interaction of dislocations in UO_2 during high burn-up structure formation. *J. Nucl. Mater.*, 444:129–137, 2014.

[61] C. Mieszczynski, C. Degueldre, G. Kuri, J. Bertsch, and C.N. Borca. Investigation of irradiated uranium-plutonium mixed oxide fuel by synchrotron based micro X-ray diffraction. *Prog. Nucl. Ener.*, 57:130–137, 2012.

[62] D. Staicu. 2.17 - Thermal Properties of Irradiated UO_2 and MOX. In Rudy J.M. Konings, editor, *Comprehensive Nuclear Materials*, pages 439–464. 2012.

[63] C. Ronchi, M. Sheindlin, D. Staicu, and M. Kinoshita. Effect of burn-up on the thermal conductivity of uranium dioxide up to 100000 MWd t^{-1}. *J. Nucl. Mater.*, 327:58–76, 2004.

[64] D.R. Olander. *Fundamental aspects of nuclear reactor fuel elements*, chapter 10. Fuel element thermal performance, pages 124–127. Technical Information Center, Office of Public Affairs Energy Research and Development Administration, 1st edition, 1976.

[65] L. Desgranges, C. Valot, B. Pasquet, J. Lamontagne, T. Blay, and I. Roure. A method for the quantification of total xenon concentration in irradiated nuclear fuel with SIMS and EPMA. *Nucl. Instrum. Meth. B*, 266:147–154, 2008.

[66] C.T. Walker, S. Brémier, S. Portier, R. Hasnaoui, and W. Goll. SIMS analysis of an UO_2 fuel irradiated at low temperature to 65 GWd/tHM. *J. Nucl. Mater.*, 393:212–223, 2009.

[67] J. Noirot, L. Desgranges, and J. Lamontagne. Detailed characterisations of high burn-up structures in oxide fuels. *J. Nucl. Mater.*, 372:318–339, 2008.

[68] J. Noirot, Y. Pontillon, S. Yagnik, J.A. Turnbull, and T. Tverberg. Fission gas release behaviour of a 103 GWd/tHM fuel disc during a 1200°C annealing test. *J. Nucl. Mater.*, 446:163–171, 2014.

[69] M. Mogensen, J.H. Pearce, and C.T. Walker. Behaviour of fission gas in the rim region of high burn-up UO_2 fuel pellets with particular reference to results from an XRF investigation. *J. Nucl. Mater.*, 264:99–112, 1999.

[70] J. Spino, D. Papaioannou, and J.-P. Glatz. Comments on the threshold porosity for fission gas release in high burn-up fuels. *J. Nucl. Mater.*, 328:67–70, 2004.

[71] P. Van Uffelen, M. Sheindlin, V.V. Rondinella, and C. Ronchi. On the relations between the fission gas behaviour and the pellet-cladding mechanical interaction in LWR fuel rods. In *Pellet-cladding interaction in water reactor fuels*, pages 213–228, Aix-en-Provence, France, 2004. NEA.

[72] D. Baron and J. Spino. Does rim microstructure formation degrade the fuel rod performance? In *Technical and economic limits to fuel burnup extension*, pages 41–49, San Carlos de Bariloche, Argentina, 1999. IAEA.

[73] T. Fuketa. Transient response of LWR fuels (RIA). In R.J.M. Konings, editor, *Comprehensive nuclear materials*, volume 2, chapter 22, pages 579–593. 2010.

[74] F. Lemoine. High burnup fuel behavior related to fission gas effects under reactivity initiated accidents (RIA) conditions. *J. Nucl. Mater.*, 248:238–248, 1997.

[75] K. Kulacsy. Mechanistic model for the fragmentation of the high-burnup structure during LOCA. *J. Nucl. Mater.*, 466:409–416, 2015.

[76] Nuclear Energy Agency. Nuclear fuel behaviour in Loss-of-Coolant Accident (LOCA) Conditions. State-of-the-art Report. Technical Report NEA No. 6846, OECD-NEA, 2009.

[77] P. Chakraborty, M. R. Tonks, and G. Pastore. Modeling the influence of bubble pressure on grain boundary separation and fission gas release. *J. Nucl. Mater.*, 452:95–101, 2014.

[78] M. Flanagan, B.C. Oberländer, and A. Puranen. Fuel fragmentation, relocation and dispersal under LOCA conditions: experimental observations. In *International Topical Meeting on LWR fuel performance*, pages 660–668, Charlotte, North Carolina, 2013. ANS.

[79] J.A. Turnbull, S.K. Yagnik, M. Hirai, D.M. Staicu, and C.T. Walker. An assessment of the fuel pulverization threshold during LOCA-type temperature transients. *Nucl. Sci. Eng.*, 179:477–485, 2015.

[80] A. Bianco, C. Vitanza, M. Seidl, A. Wensauer, W. Faber, and R. Macián-Juan. Experimental investigation on the causes for pellet fragmentation under LOCA conditions. *J. Nucl. Mater.*, 465:260–267, 2015.

[81] J. Spino and D. Papaioannou. Lattice parameter changes associated with the rim-structure formation in high burn-up UO_2 fuels by micro X-ray diffraction. *J. Nucl. Mater.*, 281:146–162, 2000.

[82] J. Spino, J. Cobos-Sabate, and F. Rousseau. Room-temperature microindentation behaviour of LWR-fuels, part 1: fuel microhardness. *J. Nucl. Mater.*, 322:204–216, 2003.

[83] International Atomic Energy Agency. Storage of spent nuclear fuel. Technical Report Specific Safety Guide No. SSG-15, IAEA, 2012.

[84] International Atomic Energy Agency. Spent fuel reprocessing options. Technical Report IAEA-TECDOC-1587, IAEA, 2008.

[85] V.V. Rondinella. Failure mechanisms of high level nuclear waste forms in storage and geological disposal conditions. In M.I. Ojovan, editor, *Handbook of advanced radioactive waste conditioning technologies*, chapter 13, pages 397–432. Woodhead Publishing, 2011.

[86] International Atomic Energy Agency. Spent fuel performance assessment and research. Technical Report IAEA-TECDOC-1343, IAEA, 2003.

[87] DEMO - Coordinated Research Project (CRP) on demonstrating performance of spent fuel and related storage system components during very long term storage. `https://www.iaea.org/OurWork/ST/NE/NEFW/Technical-Areas/NFC/spent-fuel-management-CRP-T13014.html`.

[88] V.V. Rondinella, T. Wiss, D. Papaioannou, R. Nasyrow, S. van Winckel, D. Serrano-Purroy, and D.H. wegen. Nuclear fuel safety after discharge: property evolution and testing. In *International Topical Meeting on LWR fuel performance*, Charlotte, North Carolina, 2013. ANS.

[89] P. Carbol, D.H. Wegen, T. Wiss, and P. Fors. Spent fuel as waste material. In R.J.M. Konings, editor, *Comprehensive nuclear materials*, volume 5, chapter 16, pages 389–420. 2010.

[90] T. Fanghänel, J.-P. Glatz, R. J.M. Konings, V.V. Rondinella, and J. Somers. Transuranium elements in the nuclear fuel cycle. In D.G. Cacuci, editor, *Handbook of Nuclear Engineering*, volume IV. Reactors of Generation III and IV, chapter 26, pages 2937–2998. 2010.

[91] V.V. Rondinella, J. Cobos, Hj. Matzke, T. Wiss, P. Carbol, and D. Solatie. Leaching behavior and α-decay damage accumulation of UO_2 containing short-lived actinides. In *2000 MRS Fall Meeting*, 2000.

[92] V.V. Rondinella, T. Wiss, J.-P. Hiernaut, and D. Staicu. Dose rate effects on the accumulation of radiation damage. In *11^{th} Conference on Radioactive Waste Management and Environmental Remediation*, pages 7322:1–6, 2007.

[93] V.V. Rondinella, T. Wiss, J. Cobos, and H. Hiernaut. Studies on spent fuel alterations during storage and radiolysis effects on corrosion behaviour using alpha-doped UO_2. In *9^{th} Conference on Radioactive Waste Management and Environmental Remediation*, page 4593, 2003.

[94] T. Wiss, J.-P. Hiernaut, D. Roudil, J.-Y. Colle, E. Maugeri, Z. Talip, A. Janssen, V. Rondinella, R.J.M. Konings, H.-J. Matzke, and W.J. Weber. Evolution of spent nuclear fuel in dry storage conditions for millennia and beyond. *J. Nucl. Mater.*, 451:198–206, 2014.

[95] D. Staicu, T. Wiss, V.V. Rondinella, J.-P. Hiernaut, R.J.M. Konings, and C. Ronchi. Impact of auto-irradiation on the thermophysical properties of oxide nuclear reactor fuels. *J. Nucl. Mater.*, 397:8–18, 2010.

[96] J. Cobos, L. Havela, V.V. Rondinella, J. De Pablo, T. Gouder, J.P. Glatz, P. Carbol, and H.-J. Matzke. Corrosion and dissolution studies of UO_2 containing α-emitters. *Radiochim. Acta*, 90:597–602, 2002.

[97] C. Ferry, C. Poinssot, C. Cappelaere, L. Desgranges, C. Jegou, F. Miserque, J.P. Piron, D. Roudil, and J.M. Gras. Specific outcomes of the research on the spent fuel long-term evolution in interim dry storage and deep geological disposal. *J. Nucl. Mater.*, 352:246–253, 2006.

[98] H.W. Wiese and A. Schwenk-Ferrero. webKORIGEN: A new web-based KORIGEN package for nuclide depletion calculations in nucleonica. `http://www.nucleonica.net/`.

[99] Z. Talip, T. Wiss, V. Di Marcello, A. Janssen, J.-Y. Colle, P. Van Uffelen, P. Raison, and R.J.M. Konings. Thermal diffusion of helium in ^{238}Pu-doped UO_2. *J. Nucl. Mater.*, 445:117–127, 2014.

[100] P. A.C. Raynaud and R. E. Einziger. Cladding stress during extended storage of high burnup spent nuclear fuel. *J. Nucl. Mater.*, 464:304–312, 2015.

[101] V.V. Rondinella, T. Wiss, D. Papaioannou, and R. Nasyrow. Studies on nuclear evolution during storage and testing of used fuel response to impact loadings. In *11^{th} International Confererence on Probabilistic Safety Assessment and Management and Annual European Safety and Reliability Conference*, pages 3171–3179, 2012.

[102] C. Ferry, J.-P. Piron, and A. Ambard. Effect of helium on the microstructure of spent fuel in a repository: An operational approach. *J. Nucl. Mater.*, 407:100–109, 2010.

[103] E. Maugeri, T. Wiss, J.-P. Hiernaut, K. Desai, C. Thiriet, V.V. Rondinella, J.-Y. Colle, and R.J.M. Konings. Helium solubility and behaviour in uranium dioxide. *J. Nucl. Mater.*, 385:461–466, 2009.

[104] S. Guilbert, T. Sauvage, H. Erramli, M.-F. Barthe, P. Desgardin, G. Blondiaux, C. Corbel, and J.P. Piron. Helium behavior in UO_2 polycrystalline disks. *J. Nucl. Mater.*, 321:121–128, 2003.

[105] J.-P. Crocombette. Ab initio energetics of some fission products (Kr, I, Cs, Sr and He) in uranium dioxide. *J. Nucl. Mater.*, 305:29–36, 2002.

[106] Hj. Matzke and J. Spino. Formation of the rim structure in high burnup fuel. *J. Nucl. Mater.*, 248:170–179, 1997.

[107] R.W. Rice. In *Porosity of ceramics*, chapter 3 - Porosity and microcracks dependence of elastic properties at low to moderate temperatures, pages 100–167. Marcel Dekker Inc., 1998.

[108] R.W. Rice. In *Porosity of ceramics*, chapter 6 - Hardness and related properties, pages 276–291. Marcel Dekker Inc., 1998.

[109] J. Luo and R. Stevens. Porosity-dependence of elastic moduli and hardness of 3Y-TZP ceramics. *Ceram. Int.*, 25:281–286, 1999.

[110] J.L. Bates. Microhardness of uranium dioxide. Technical Report HW-77799, Hanford Atomic Products Operation, 1963.

[111] S. S. Kim and T. Kirihara. Micro-hardness of neutron irradiated uranium dioxide at room temperature. *J. Nucl. Sci. Technol.*, 20:1023–1031, 1983.

[112] N. Nakae, A. Harada, T. Kirihara, and S. Nasu. Irradiation induced lattice defects in UO_2. *J. Nucl. Mater.*, 71:314–319, 1978.

[113] V. M. Baranov, Yu. K. Bibilashvili, I. S. Golovnin, V. N. Kakurin, T. S. Men'shikova, Yu. V. Miloserdin, and A. V. Rimashevskii. In-reactor measurements of the modulus of elasticity of uranium dioxide. *Sov. Atom. Ener.*, 40:37–39, 1976.

[114] D. Laux, D. Baron, G. Despaux, A.I. Kellerbauer, and M. Kinoshita. Determination of high burn-up nuclear fuel elastic properties with acoustic microscopy. *J. Nucl. Mater.*, 420:94–100, 2012.

[115] D. Laux, G. Despaux, F. Augereau, J. Attal, D. Baron, J.M. Gatt, V. Basini, P. M. Chantoin, and J.-M. Saurel. Ultrasonic measurement of high burn-up fuel elastic properties. In *6^{th} international conference on WWER Fuel Performance, Modelling and Experimental Support*, Albena, Bulgaria, 2005.

[116] B.E. Schaner. Metallographic determination of the UO_2-U_4O_9 phase diagram. *J. Nucl. Mater.*, 2:110–120, 1960.

[117] D.G. Martin. The elastic constants of polycrystalline UO_2 and (U,Pu) mixed oxides: a review and recommendations. *High Temp.-High Press.*, 21:13–24, 1989.

[118] D. Laux. *Caractérisation mécanique de combustibles nucléaires à fort taux de combustion par méthodes micro-acoustiques*. PhD thesis, University Montpellier II, 2002.

[119] J. Boocock, A.S. Furzer, and J.R. Matthews. The effect of porosity on the elastic moduli of UO_2 as measured by an ultrasonic technique. AERE-M 2565, UK Atomic Energy Authority, 1972.

[120] E. A. Dean. Elastic moduli of porous sintered materials as modeled by variable-aspect-ratio self-consistent oblate-spheroidal-inclusion theory. *J. Amer. Ceram. Soc.*, 66:847–854, 1983.

[121] J. Rest, G.L. Hofman, and Y. S. Kim. Analysis of intergranular fission-gas bubble-size distributions in irradiated uranium-molybdenum alloy fuel. *J. Nucl. Mater.*, 385:563–571, 2009.

[122] J. Rest. Evolution of fission-gas-bubble-size distribution in recrystallized U-10Mo nuclear fuel. *J. Nucl. Mater.*, 407:55–58, 2010.

[123] F. Cappia, D. Pizzocri, A. Schubert, P. Van Uffelen, R. Macián-Juan, and V.V. Rondinella. Critical assessment of the pore size distribution in the rim region of high burnup UO_2 fuel. *J. Nucl. Mater.*, 480:138–149, 2016.

[124] I.J. McColm. In *Ceramic hardness*, chapter 1 - Introduction and overview, pages 1–31. Springer, 1990.

[125] I.J. McColm. In *Ceramic hardness*, chapter 2 - Some aspects of method, pages 33–34. Springer, 1990.

[126] Standard method for Vickers indentation hardness of advanced ceramics. ASTM C 1327-99, 1999.

[127] B.T. Khuri-Yakub. Scanning acoustic microscopy. *Ultrasonics*, 31:361–372, 1993.

[128] D. Laux, G. Despaux, and F. Augereau. Improvement of the minimal characterisation size available by acoustic microscopy for mechanical parameters evaluation. *Eur. Phys. J. A.P.*, 17:163–169, 2002.

[129] D. Laux, W. de Weerd, D. Papaioannou, S. Kitajima, V.V. Rondinella, and G. Despaux. Scanning acoustic microscope for mechanical characterization and density estimation of irradiated nuclear fuel. *Prog. Nucl. Energ.*, 72:63–66, 2014.

[130] P.B. Corson. Correlation functions for predicting properties of heterogeneous materials. I. Experimental measurement of spatial correlation functions in multiphase solids. *J. Appl. Phys.*, 45:3159–3164, 1974.

[131] J.G. Berryman and S.C. Blair. Use of digital image analysis to estimate fluid permeability of porous materials: Application of two-point correlation functions. *J. Appl. Phys.*, 60:1930–1938, 1986.

[132] J. Goebelbecker. Quantitative image analysis of unirradiated fast breeder reactor fuel. *J. Nucl. Mater.*, 153:59–65, 1988.

[133] J.C. Russ. *Image analysis of Food Microstructure*, pages 306–308. CRC Press, Boca Raton, Florida, USA, 2005.

[134] N. Otsu. A threshold selection method from gray-level histograms. *IEEE Transactions on Systems, Man, and Cybernetics*, 9:62–66, 1979.

[135] S. Torquato. *Random Heterogeneous Materials: Microstructure and Macroscopic Properties*, chapter 2. Microstructural descriptors, pages 23–58. Springer-Verlag, 2002.

[136] Y. Jiao, F.H. Stillinger, and S. Torquato. Modeling heterogeneous materials via two-point correlation functions: Basic principles. *Phys. Rev. E*, 76:031110, 2007.

[137] International Organization for Standardization. Representation of results of particle size analysis - Part 1: Graphical representation. ISO 9276-1:1998, Copyright© ISO, 1998.

[138] International Organization for Standardization. Representation of results of particle size analysis - Part 6: Descriptive and quantitative representation of particle shape and morphology. ISO 9276-6:2008, Copyright© ISO, 2008.

[139] S. Nagabhushana. *Computer Vision and Image Processing*, chapter 1. Introduction, pages 21–23. New Age International Publisher, 1st edition, 2005.

[140] E. E. Underwood. *Quantitative stereology*, chapter 5. Particle and grain-size distributions, pages 119–123. Addison-Wiley, 1st edition, 1970.

[141] J. C. Russ. 8 - Image Measurements. In *The Image Processing Handbook*. CRC Press, 1998.

[142] A. I. Medalia. Dynamic shape factors of particles. *Powder Technol.*, 4:117–138, 1971.

[143] R. T. DeHoff. *Quantitative microscopy*, chapter 5. Measurement of number and average size in volume, pages 136–142. McGraw-Hill, 1st edition, 1968.

[144] E. E. Underwood. *Quantitative microscopy*, chapter 6. Particle size distribution, pages 162–168. McGraw-Hill, 1st edition, 1968.

[145] E.E. Underwood. Stereology, or the quantitative evaluation of microstructures. *Journal of Microscopy*, 89:161–180, 1969.

[146] S.A. Saltikov. *Stereology: Proceedings of the Second International Congress for STEREOLOGY, Chicago April þ8-þ13*, chapter The Determination of the Size Distribution of Particles in an Opaque Material from a Measurement of the Size Distribution of Their Sections, pages 163–173. Springer Berlin Heidelberg, Berlin, Heidelberg, 1967.

[147] C. Ronchi. Physical processes and mechanisms related to fission gas swelling in MX-type nuclear fuels. *J. Nucl. Mater.*, 84:55–84, 1979.

[148] J. Jeppsson, K. Mannesson, A.a Borgenstam, and J. Agren. Inverse Saltykov analysis for particle-size distributions and their time evolution. *Acta Mater.*, 59:874 – 882, 2011.

[149] B.W. Silverman. *Density Estimation for Statistics and Data Analysis*, chapter 3. The kernel method for univariate data, pages 34–74. Chapman and Hall, 1st edition, 1986.

[150] C.C. Taylor. A new method for unfolding sphere size distributions. *Journal of Microscopy*, 132(1):57–66, 1983.

[151] Y. Gulbin. On estimation and hypothesis testing of the grain size distribution by the saltykov method. *Image Anal. Stereol.*, 27:163–174, 2008.

[152] J. Takahashi and H. Suito. Evaluation of the accuracy of the three-dimensional size distribution estimated from the Schwartz-Saltykov method. *Metall. Mater. Trans. A*, 34:171–181, 2003.

[153] J. Takahashi and H. Suito. Effect of omitting small sectioned particles with limited cross-sectional area on characterisation of secondary phase particles. *Materials Science and Technology*, 18:103–110, 2002.

[154] F. Cappia, D. Pizzocri, M. Marchetti, A. Schubert, P. Van Uffelen, L. Luzzi, D. Papaioannou, R. Macián-Juan, and V.V. Rondinella. Microhardness and Young's modulus of high burn-up UO_2 fuel. *J. Nucl. Mater.*, 479:447–454, 2016.

[155] F. Cappia, J.I. Tijero Cavia, R. Macián-Juan, and V.V. Rondinella. Investigations of very high burnup UO_2 fuels in Light Water Reactors. In *Proceedings of the European Nuclear Conference 2016*, Warsaw, Poland, 2016. ENS. Participation to the 10^{th} ENEN Ph.D Event & Prize.

[156] J. Spino. Safety of nuclear fuels - high burn-up performance. Annual Activity Report EUR 20252, European Commission, JRC-ITU, 2001.

[157] R. Manzel and C.T. Walker. EPMA and SEM of fuel samples from PWR rods with an average burn-up of around 100 MWd/kgHM. *J. Nucl. Mater.*, 301:170–182, 2002.

[158] U. Fischer and H. W. Wiese. Verbesserte konsistente Berechnung des nuklearen Inventars abgebrannter DWR-brennstoffe auf der Basis von Zell-Abbrand-Verfahren mit KORIGEN. Technical Report KfK 3014, Kernforschungszentrum Karlsruhe, 1983.

[159] U. Fischer and H. W. Wiese. Improved and consistent determination of the nuclear inventory of spent PWR fuel on the basis of cell-burnup methods usinq KORIGEN. Technical Report ORNL-tr-5043, ORNL, 1983. Translated from the German. Report KfK 3014 issued by the Kernforschungszentrum Karlsruhe.

[160] J. Tijero-Cavia. unpublished work, 2016.

[161] Jaakko Leppänen. Development of a new Monte Carlo reactor physics code. Technical Report VTT publications 640, VTT Technical Research Centre, Copyright ©, 2007. Dissertation for the degree of Doctor of Science in Technology.

[162] A. Santamarina, D. Bernard, P. Blaise, M. Coste, A. Courcelle, T.D. Huynh, C. Jouanne, P. Leconte, O. Litaize, S. Mengelle, G. Noguère, J.-M. Ruggiéri, O. Sérot, J. Tommasi, C. Vaglio, and J.-F. Vidal. The JEFF-3.1.1 Nuclear Data Library. Technical Report NEA No. 6807, OECD/NEA, 2009.

[163] P. Arató, E. Besenyei, A. Kele, and F. Wéber. Mechanical properties in the initial stage of sintering. *J. Mater. Sci.*, 30:1863–1871, 1995.

[164] R.W. Rice. Evaluation and extension of physical property-porosity models based on minimum solid area. *J. Mater. Sci.*, 31:102–118, 1996.

[165] R.W. Rice. In *Porosity of ceramics*, chapter 2 - Evaluation of porosity dependence of properties, pages 72–84. Marcel Dekker Inc., 1998.

[166] K. Lassmann and A. Moreno. The light-water-reactor version of the URANUS integral fuel-rod code. Technical report, Institute of Reactor Technology, Technical University of Darmstadt, 1977.

[167] P.E. MacDonald and L.B. Thompson. MATPRO - Version 09. A handbook of material properties for the use in the analysis of Light Water Reactor fuel rod behavior. TREE-NUREG-1005, Idaho National Engineering Lab., Idaho Falls (USA), 1976.

[168] D. L. Hagrman and G. A. Reymann. MATPRO - Version 11. A handbook of material properties for the use in the analysis of Light Water Reactor fuel rod behavior. NUREG/CR-0497 TREE-1280 R3, Idaho National Engineering Lab., Idaho Falls (USA), 1979.

[169] W.C. Oliver and G.M. Pharr. An improved technique for determining hardness and elastic modulus using load and displacement sensing indentation experiments. *J. Mater. Res.*, 7:1564–1583, 1992.

[170] W.C. Oliver and G.M. Pharr. Measurement of hardness and elastic modulus by instrumented indentation: advances in understanding and refinements to methodology. *J. Mater. Res.*, 19:3–20, 2004.

[171] Y.-T. Cheng and C.-M. Cheng. Scaling, dimensional analysis, and indentation measurements. *Mater. Sci. Eng. R*, 44:91–149, 2004.

[172] A.E. Giannakopoulos, P.-L. Larsson, and R. Vestegaard. Analysis of Vickers indentation. *Int. J. Solids Struct.*, 31:2679–2708, 1994.

[173] Z. Li, Y.-T. Cheng, H. T. Yang, and S. Chandrasekar. On two indentation hardness definitions. *Surf. Coat. Tech.*, 154:124 – 130, 2002.

[174] T.R.G. Kutty, A.K. Sengupta, and C. Ganguly. Indentation technique for mechanical property evaluation of ceramic nuclear fuels. In *International Workshop on Indentation Techniques*, Bologna, Italy, 1990. European Appl. Res. Rept. - Nucl. Sci. Technol.

[175] K. Yamada, S. Yamanaka, and M. Katsura. Mechanical properties of $(U, Ce)O_2$. *J. Alloy Compd.*, 273:697–701, 1998.

[176] M.C. Pujol, M. Idiri, L. Havela, S. Heathman, and J. Spino. Bulk and Young's modulus of doped UO_2 by synchrotron diffraction under high pressure and Knoop indentation. *J. Nucl. Mater.*, 324:189–197, 2004.

[177] J. Spino. Determination of the Young's modulus of irradiated fuels by Knoop indentation. Annual Activity Report, European Commission, JRC-ITU, 2005.

[178] H. Stehle, H. Assmann, and F. Wunderlich. Uranium dioxide properties for LWR fuel rods. *Nucl. Eng. Des.*, 33:230–260, 1975.

[179] H. Többe. Der Brennstab-Code IAMBUS. Technischer Bericht 73.65, Interatom, 1973.

[180] J.D. Hales, R. L. Williamson, S.R. Novascone, G. Pastore, B.W. Spencer, D.S. Stafford, K.A. Gamble, D.M. Perez, and W. Liu. BISON Theory Manual - The Equations behind Nuclear Fuel Analysis. INL/EXT-13-29930, Idaho Falls, (USA), 2014.

[181] M. Suzuki, H. Saitou, Y. Udagawa, and F. Nagase. Light Water Reactor Fuel Analysis Code FEMAXI-7. Model and Structure, Copyright © 2013. JAEA-Data/Code 2013 - 005, Reactor Safety Research Unit, Nuclear Safety Research Center, Japan Atomic Energy Agency, 2013.

[182] Fuel Performance Analysis Capability in FALCON. 1002866, EPRI, Palo Alto, CA, 2002.

[183] K.J. Geelhood, W.G. Luscher, P.A. Raynaud, and I.E. Porter. FRAPCON-4.0: A Computer Code for the Calculation of Steady-State, Thermal-Mechanical Behavior of Oxide Fuel Rods for High Burnup. PNNL-19418, Vol.1 Rev.2, Pacific Northwest National Laboratory, Richland, Washington, 2015.

[184] SCDAP/RELAP5-3D©Code development team. SCDAP/RELAP5-3D©CODE MANUAL. MATPRO - A library of material properties for light-water-reactor accident analysis. INEEL/EXT-02-00589, Idaho National Engineering Lab., Idaho Falls (USA), 2003.

[185] J. Spino, H. Santa Cruz, R. Jovani-Abril, R. Birtcher, and C. Ferrero. Bulk-nanocrystalline oxide nuclear fuels - an innovative material option for increasing fission gas retention, plasticity and radiation-tolerance. *J. Nucl. Mater.*, 422:27–44, 2012.

[186] H. Stehle. Performance of oxide nuclear fuel in water-cooled power reactors. *J. Nucl. Mater.*, 153:3–15, 1988.

[187] N. Lozano, L. Desgranges, D. Aymes, and J.C. Niepce. Influence of rounds sub-grains in high burnup UO_2 fuel. In *Technical and economic limits to fuel burnup extension*, IAEA-TECDOC-1299, pages 32–40, San Carlos de Bariloche, Argentina, 1999. IAEA.

[188] L. Holt, A. Schubert, P. Van Uffelen, C.T. Walker, E. Fridman, and T. Sonoda. Sensitivity study on Xe depletion in the high burn-up structure of UO_2. *J. Nucl. Mater.*, 452:166–172, 2014.

[189] G. Khvostov, V. Novikov, A. Medvedev, and S. Bogatyr. Approaches to modeling of high burn-up structure and analysis of its effects on the behaviour of light water reactor fuels in the START-3 fuel performance code. In *International Topical Meeting on LWR fuel performance*, Kyoto, Japan, 2005.

[190] A. Schubert. unpublished work, 2016.

[191] D. Pizzocri, F. Cappia, L. Luzzi, G. Pastore, V.V. Rondinella, and P. Van Uffelen. A semi-empirical model for the formation and the depletion of the high burnup structure in UO_2 fuel. *J. Nucl. Mater.*, 487:23–29, 2017.

[192] J. Arborelius, M. Dahlbäck, L. Hallstadius, P. Jourdain, T. Andersson, R. Lisdat, M. Hahn, and E.H. Toscano. The effect of duplex cladding outer component tin content on corrosion, hydrogen pick-up and hydride distribution at very high burnup. In *Zirconium in the Nuclear Industry: Fourteenth International Symposium*, Stockholm, Sweden, 2004. ASTM.

[193] SAS Institute Inc. *SAS/STAT® 12.1 User's Guide*, chapter 31 - The CLUSTER Procedure, page 1934. Springer Berlin Heidelberg, Cary, NC, USA, 2012.

[194] J. B. Freeman and R. Dale. Assessing bimodality to detect the presence of a dual cognitive process. *Behav. Res. Methods*, 45:83–97, 2013.

[195] R. Pfister, K. A. Schwarz, M. Janczyk, R. Dale, and J. B. Freeman. Good things peak in pairs: a note on the bimodality coefficient. *Front. Psychol.*, 4:700:1–4, 2013.

[196] S. Torquato. Nearest-neighbor statistics for packings of hard spheres and disks. *Phys. Rev. E*, 51:3170–3182, 1995.

[197] T. Tverberg and W. Wiesenack. Fission gas release and temperature data from instrumented high burnup LWR fuel. In *Technical and economic limits to fuel burnup extension*, pages 7–16, San Carlos de Bariloche, Argentina, 1999. IAEA.

[198] D. Baron and L. Hallstadius. Fuel performance of Light Water Reactors (Uranium oxide and MOX). In R.J.M. Konings, editor, *Comprehensive nuclear materials*, volume 2, chapter 19, pages 481–514. 2010.

[199] P. Van Uffelen. *Contribution to modelling of fission gas release in light water reactor Fuel*. PhD thesis, Université de Liège, 2002.

[200] Hj. Matzke. Gas release mechanisms in UO_2 - a critical review. *Radiat. Eff. Defects Solids*, 53:219–242, 1980.

[201] K. Lassmann, A. Schubert, J. van de Laar, and C.W.H.M. Coquerelle. Recent developments of the TRANSURANUS code with emphasis on high burnup phenomena. In *Nuclear fuel behaviour modelling at high burnup and its experimental support*, pages 387–405, Windermere, United Kingdom, 2001. IAEA.

[202] K. Lassmann, A. Schubert, P. Van Uffelen, C. Györi, and J. van de Laar. *TRANSURANUS Handbook, Copyright © 1975-2014*. Institute for Transuranium Elements, Karlsruhe, Germany, 2014.

[203] V.I. Tarasov and M.S. Veshchunov. Models for fuel porosity evolution in UO_2 under various regimes of reactor operation. *Nucl. Eng. Des.*, 272:65–83, 2014.

[204] L.K. Mansur. Void swelling in metals and alloys under irradiation: an assessment of the theory. *Nucl. Technol.*, 40:5–34, 1978.

[205] M.S. Veshchunov and V.I. Tarasov. Modelling of pore coarsening in the high burn-up structure of UO_2 fuel. *J. Nucl. Mater.*, 488:191–195, 2017.

[206] L. Noirot, Ph. Garcia, and C. Struzik. A mechanistic fission gas behaviour model for UO_2 and MOX fuels. In *Fission gas behaviour in light water reactor fuels*, pages 131–149, Cadarache, France, 2000.

[207] L. Noirot. MARGARET: A comprehensive code for the description of fission gas behavior. *Nucl. Eng. Des.*, 241:2099–2118, 2011.

[208] D.R. Olander. *Fundamental aspects of nuclear reactor fuel elements*, chapter 13. Swelling due to fission gases, pages 210–213. Technical Information Center, Office of Public Affairs Energy Research and Development Administration, 1st edition, 1976.

[209] G. Khvostov, K. Mikityuk, and M.A. Zimmermann. A model for fission gas release and gaseous swelling of the uranium dioxide fuel coupled with the FALCON code. *Nucl. Eng. Des.*, 241:2983–3007, 2011.

[210] M. Fanfoni and M. Tomellini. The Johnson-Mehl-Avrami-Kolmogorov model: A brief review. *Il Nuovo Cimento D*, 20:1171–1182, 1998.

[211] J. Noirot, Y. Pontillon, S. Yagnik, and J.A. Turnbull. Post-irradiation examinations and high-temperature tests on undoped large-grain UO_2 discs. *J. Nucl. Mater.*, 462:77 – 84, 2015.

[212] G. Khvostov, A. Medvedev, and S. Bogatyr. The dynamic model of grain boundary processes in high burn-up lwr fuel and its application in analysis by the START-3 code. In *5th international conference on WWER Fuel Performance, Modelling and Experimental Support*, Albena, Bulgaria, 2003.

[213] P. Blair, A. Romano, Ch. Hellwig, and R. Chawla. Calculations on fission gas behaviour in the high burnup structure. *J. Nucl. Mater.*, 350:232–239, 2006.

[214] D.R. Olander and P. Van Uffelen. On the role of grain boundary diffusion in fission gas release. *J. Nucl. Mater.*, 288:137–147, 2001.

[215] P. Blair, G. Khvostov, A. Romano, Ch. Hellwig, and R. Chawla. Interpretation of high-burnup fuel annealing tests. *Nucl. Eng. Technol.*, 45:639–646, 2008.

[216] Hj. Matzke. Atomic transport properties in UO_2 and mixed oxides $(U, Pu)O_2$. *J. Chem. Soc. Farad. Trans.*, 83:1121–1142, 1987.

[217] H. Wallin, L.Å. Nordström, , and Ch. Hellwig. Fission gas model of the fuel code SPHERE-3. In *Fission gas behaviour in light water reactor fuels*, pages 391–407, Cadarache, France, 2000.

[218] M. Lemes, A. Soba, and A. Denis. An empirical formulation to describe the evolution of the high burnup structure. *J. Nucl. Mater.*, 456:174–181, 2015.

[219] A. Soba and A. Denis. DIONISIO 2.0: New version of the code for simulating a whole nuclear fuel rod under extended irradiation. *Nucl. Eng. Des.*, 292:213–221, 2015.

[220] K. Une, M. Hirai, K. Nogita, T. Hosokawa, Y. Suzawa, S. Shimizu, and Y. Etoh. Rim structure formation and high burnup fuel behavior of large-grained UO_2 fuels. *J. Nucl. Mater.*, 278:54–63, 2000.

[221] D. Pizzocri, F. Cappia, V.V. Rondinella, and P. Van Uffelen. Preliminary model for the pore growth in the HBS. Technical Report JRC103064, European Commission, Directorate for Nuclear Safety and Security, JRC-Karlsruhe, 2016.

[222] U. Gösele. Concentration dependence of rate constants for diffusion- or reaction-controlled void-point-defect reactions. *J. Nucl. Mater.*, 78:83–95, 1978.

[223] T. Kogai. Modelling of fission gas release and gaseous swelling of light water reactor fuels. *J. Nucl. Mater.*, 244:131–140, 1997.

[224] M.V. Speight and W. Beere. Vacancy potential and void growth on grain boundaries. *Met. Sci.*, 9:190–191, 1975.

[225] S.K. Tyler and P.J. Goodhew. Direct evidence for the brownian motion of helium bubbles. *J. Nucl. Mater.*, 92:201 – 206, 1980.

[226] D. Preininger and D. Kaletta. The growth of gas-bubbles by coalescence in solids during continuous gas generation. *J. Nucl. Mater.*, 117:239–243, 1983.

[227] A. Baldan. Review progress in ostwald ripening theories and their applications to nickel-base superalloys part i: Ostwald ripening theories. *Jo. Mater. Sci.*, 37:2171–2202, 2002.

[228] R.J. White. The development of grain-face porosity in irradiated oxide fuel. *J. Nucl. Mater.*, 325:61–77, 2004.

[229] J.A. Turnbull. The mobility of intragranular bubbles in uranium dioxide during irradiation. *J. Nucl. Mater.*, 62:325–328, 1976.

[230] I.M. Lifshitz and V.V. Slyozov. The kinetics of precipitation from supersaturated solid solutions. *J. Phys. Chem. Solids*, 19:35–50, 1961.

[231] H. Schroeder and P.F.P. Fichtner. On the coarsening mechanisms of helium bubbles - Ostwald ripening versus migration and coalescence. *J. Nucl. Mater.*, 179:1007–1010, 1991.

[232] P.F.P. Fichtner, H. Schroeder, and H. Trinkaus. A simulation study of Ostwald ripening of gas bubbles in metals accounting for real gas behaviour. *Acta Metall. Mater.*, 39:1845–1852, 1991.

[233] H. Xiao and C. Long. Modeling of Pore Coarsening in the Rim Region of High Burn-up UO_2 Fuel. *Nucle. Eng. Technol*, 48:1002–1008, 2016.

[234] S. Torquato. *Random Heterogeneous Materials: Microstructure and Macroscopic Properties*, chapter 5. Monodisperse spheres, page 128. Springer-Verlag, 2002.

[235] S. Chandrasekhar. Stochastic problems in physics and astronomy. *Rev. Mod. Phys.*, 15:1–89, 1943.

[236] S. Torquato. *Random Heterogeneous Materials: Microstructure and Macroscopic Properties*, chapter 3. Many-particle statistics, pages 59–95. Springer-Verlag, 2002.

[237] `http://imagejdocu.tudor.lu/doku.php?id=macro:radially_averaged_autocorrelation`, 2009.

[238] G. Pastore, L. Luzzi, V. Di Marcello, and P. Van Uffelen. Physics-based modelling of fission gas swelling and release in UO_2 applied to integral fuel rod analysis. *Nucl. Eng. Des.*, 256:75–86, 2013.

[239] S. Torquato. *Random Heterogeneous Materials: Microstructure and Macroscopic Properties*, chapter 10. Some continuum percolation results, pages 234–256. Springer-Verlag, 2002.

[240] S. Brémier and C.T. Walker. Radiation-enhanced diffusion and fission gas release from recrystallised grains in high burn-up UO_2 nuclear fuel. *Radiation Effects and Defects in Solids*, 157:311–322, 2002.

[241] J.A. Turnbull, C.A. Friskney, J.R. Findlay, F.A. Johnson, and A.J. Walter. The diffusion coefficients of gaseous and volatile species during the irradiation of uranium dioxide. *J. Nucl. Mater.*, 107:168–184, 1982.

[242] S.D. Wicksell. The corpuscle problem. a mathematical study of a biometric problem. *Biometrika*, 17:84–99, 1925.

[243] B.W. Silverman. *Density Estimation for Statistics and Data Analysis*, chapter 1. Introduction, pages 1–2. Chapman and Hall, 1st edition, 1986.

[244] B.W. Silverman. *Density Estimation for Statistics and Data Analysis*, chapter 2. Survey of existing methods, pages 13–19. Chapman and Hall, 1st edition, 1986.

[245] B.W. Silverman. *Density Estimation for Statistics and Data Analysis*, chapter 5. Three important methods, pages 100–110. Chapman and Hall, 1st edition, 1986.

[246] R. Cao, A. Cuevas, and W.G. Manteiga. A comparative study of several smoothing methods in density estimation. *Comput. Stat. Data An.*, 17:153–176, 1994.

[247] P. Hall, J.S. Marron, and B.U. Park. Smoothed cross-validation. *Probab. Theory Rel.*, 92(1):1–20, 1992.

[248] WAFO-group. *WAFO - A Matlab Toolbox for Analysis of Random Waves and Loads - A Tutorial*. Math. Stat., Center for Math. Sci., Lund Univ., Lund, Sweden, 2000.

[249] S. Torquato, B. Lu, and J. Rubinstein. Nearest-neighbor distribution functions in many-body systems. *Phys. Rev. A*, 41:2059–2075, 1990.

Acknowledgements

The work in this thesis was financially supported by the European Commission through the Training and Mobility of Researchers program in the 7th Framework Program and Horizon 2020 of the European Commission. I would like to thank the former and present director of the ex Institute for Transuranium Elements (ITU), now part of the Directorate for Nuclear Safety and Security, Prof. Dr. Thomas Fanghänel and Dr. Maria Betti for giving me the possibility to perform this research project in the institute. I would like to acknowledge Prof. Dr. Rafael Macián-Juan for accepting me as Ph.D. candidate at the Technische Universität München and for the warm encouragement while performing these studies. I thank Prof. Dr. Lelio Luzzi for accepting to review this manuscript.
I am thankful to AREVA GmbH for providing some of the commercial samples here used. I also acknowledge the NFIR project and thank its members for the permission to publish the results obtained on the special irradiation discs.

I owe my sincere gratitude to my supervisor at ITU Dr. Vincenzo Rondinella, not only for the scientific advice he provided, but also for guiding me during these years with his catching optimism, for sharing with me his passion about the nuclear fuels and the HBS.

This work would not have been possible without the contribution of many. A big thank you to Gianni, not only for being an amazing colleague, but also a great friend. I will always be grateful for all the times you prepared my samples even if it was not planned and priorities were others. I am indebted to Didier, who with patience taught me how to use the SEM and spent a lot of time with me acquiring the images. I had the support and encouragement of Lorenzo, who introduced me to the image analysis and its “secrets”. Thanks to Gegé, Ramil and Ralf for being always available when I was rushing in wing B and asking for another sample. I acknowledge the alpha-gamma group and the radioprotection officers, for the wonderful technical support they gave me: Klaus, Michael, Waldemar, Markus, Martin, Bjorn, Gerrit, Joseph, Dragan, Tony, Claudia, Matthias and Yvan. Thanks to Laurent and especially to Matthias for advising me with their expertise when I was coming up with crazy ideas about new experiments. Bert and Markus deserve a special mention for their help in the lab during the last sample preparation.

My heartfelt acknowledgements are due to Davide and José for the nice collaborations we set up during this work. Particularly, thank you Davide for making me discover the modeling of fission gas. I will never forget the vibrant discussions in our offices drawing cell models and concentration profiles in the HBS. Your collaboration has been a rich

source of professional development, and your friendship a source of cheerful moments with the others of the Italian group.

It was an honour to collaborate with Dr. Paul Van Uffelen, Dr. Arndt Schubert and Jaques van de Laar, who supported me with the TRANSURANUS calculations and gave precious inputs to this thesis. Special thanks are conveyed to Dr. Thierry Wiss, Dr. Stephane Brémier and Dr. Concetta Fazio for the fruitful scientific advice and for all the time invested in discussing with me the results.
It was a real pleasure to work with Birgit for the Research Fellows Association. I am thankful to Petra, Eirini, Ursula and Anna for the warm support they provided with the ITU procedures.

The years I spent in Karlsruhe offered me the possibility to meet many people with whom I shared unforgettable moments. I would like to thank Sarah for the nice evenings together both in Germany and in Italy. My memories at ITU will be always linked to the Italian groups, to our loud lunches in the Imbiss and messy beach volley matches: thanks to Fidelma, Luca, Valentina, Zap, Sara, Luchino, Daniele, Laura, Lio, Nicolino, Elena, Lorenzo, Madda, Elisa, Manlio, Alberto, Luana and Enrica for sharing with me those happy times. Thanks to Johnny and Frau Wahuuuuu, Sylvain, Emily, Brandon, Frau Martel, Vaclav, Ondrej and Pavel for all the amazing moments we spent together climbing, the beers we *prost* together, the barbeques in the park. Nazdrave b******!
I appreciated to meet many Research Fellows and nice people during these years at ITU: Lars, Oli, Roland, Mohamed, Damien, Dario, Jone, Nadya, Manuel, Ernesto, Toto.

A special thank you goes to Eli, my “socia” in all my adventures here in Karlsruhe. She was there in all the uncountable good moments, and in all the stressful ones too (come on, if I was telling that the Ph.D. was all sunshine and rainbows would you believe me?). I don’t know how many times I dialled that 886, and you were always on the other side to listen to me and to support me. Thank you for all the biking, climbing, running, for the shopping strolls on Saturday afternoon. Thank you for simply being one of my best friends.

Part of my heart will always be in Italy, where I have my old friends and family. Thanks to my big bro Peter, Patata, Silvia, Massi and Lalla who are always there for a spritz together when I cross the Alps. I owe my deepest gratitude to Saretta on whose true, everlasting friendship I can count even if I will be on the other side of the world.

I have no words to thank my family for supporting me through my career choices. Thank you Mum and Grandma for giving me your unconditioned love and being patient when I call you less often than I should. Thank you for making me feel special. I am thankful to my cousin Anna for her friendship and love. From you I learnt never to give up, and to fight for my achievements. Thanks to my Dad for teaching me the power of forgiveness. You taught me that it is never too late to make peace.

The last acknowledgement goes to the most important person, Tsveti. With your bright smile, you taught me to always look at the positive side, you inspired me and made me believe in myself when I thought I could not make it. I shared with you all the little moments in these three years that made this experience unique. I owe you my deepest gratitude for being always next to me, for walking with me along this path till the end. Thank you for making me a happy, strong woman.